ADVANCED MATERIALS
www.advmat.de

# Materials, Actuators, and Sensors for Soft Bioinspired Robots

*Mahdi Ilami, Hosain Bagheri, Reza Ahmed, E. Olga Skowronek, and Hamid Marvi**

**Biological systems can perform complex tasks with high compliance levels. This makes them a great source of inspiration for soft robotics. Indeed, the union of these fields has brought about bioinspired soft robotics, with hundreds of publications on novel research each year. This review aims to survey fundamental advances in bioinspired soft actuators and sensors with a focus on the progress between 2017 and 2020, providing a primer for the materials used in their design.**

## 1. Introduction

Taking inspiration from some of nature's most sophisticated creations has proven to be extremely beneficial toward the advancement of soft robotics. A few examples are soft robots inspired by snakes,[1] worms,[2] inchworms,[3] fish,[4] cephalopods,[5] and jellyfish[6]. The deformability and dexterity of these animals, and other soft-bodied species, embody the goals set for the field of soft robotics.

Motivations toward bioinspired soft robotics are abundant, including wearable and interactive robots for medical and military fields,[7–10] adaptable robots for search and rescue missions over unstructured terrains,[11] and underwater and flying robots for exploration,[12–14] to name a few. While wearable electronics such as those used for monitoring health[15,16] do not require strength to support limb weight, they are obliged to be flexible, such that the users can conduct their regular daily activities while wearing the device. The desire for deformable devices extends to robots interacting with the world around them. The real world can be unpredictable and unstructured. Soft bodies and limbs are more adept than their rigid counterparts at navigating uneven terrains since they can deform and maintain contact with such substrates. This incredible adaptability of soft robots to their environment is often matched by their ability to withstand damage.[17,18] In some cases, soft robots can also heal their bodies, something rigid robots are generally not capable of doing.[19–22]

This review covers recent advancements in the field of bioinspired soft robotics, with a primary focus on the last 4 years (2017–2020). The review serves as a toolbox for an interdisciplinary audience interested in the most recent bioinspired soft robotic technologies. In particular, it highlights and explores the vital components of soft robots, focusing on the enabling mechanisms and their biological inspirations. The first section discusses the materials used to fabricate soft bioinspired robots. Soft bioinspired actuation and sensing are then discussed, exploring their capabilities and implementation by researchers. Existing challenges and future potentials of bioinspired soft robots are addressed in the concluding remarks. This review provides engineers and scientists with the latest technological advancements and information needed for designing and developing the next generation of soft bioinspired robotic systems. The future applications of these robots will be grand and limitless.

## 2. Materials Used for Bioinspired Sensors and Actuators

Classical robotic systems are comprised of rigid bodies, actuators, and sensors. Unfortunately, many of these well-developed actuators and sensors are not transferable to soft bodies. Thus, researchers working in soft robotics need to reinvent actuators and sensors for soft moving bodies. Biological organisms can be an excellent inspiration for designing these soft actuators and sensors, allowing for their integration in both soft and rigid bodies. The design process of soft actuators and sensors have to be initiated with material selection and composition, for they are foundations upon which the actuators and sensors will be built around. Presently, a diversified list of materials has been used in the development of soft robotic systems. This section will cover some of the latest advancements in the last 4 years in the area of material selection and composition for the design and development of soft bioinspired actuators and sensors.

During the past 4 years, researchers have produced soft bioinspired actuators and sensors using biological material such as muscle tissue,[23,24] and plant fibers;[25] carbon-based materials such as graphite and graphene oxide (GO)[26–31] and carbon nanotubes (CN);[32,33] hydrogel materials such as poly(N-isopropylacrylamide) (PNIPAM),[34,35] liquid crystal elastomers (LCE),[36] dielectric elastomers (DE),[37] and ionic polymer-metal composites (IPMC).[38] An overview of these materials (**Figure 1**), along with their underlying mechanisms, are discussed below.

---

M. Ilami, H. Bagheri, R. Ahmed, E. O. Skowronek, Dr. H. Marvi
School for Engineering of Matter
Transport & Energy
Arizona State University
Tempe, AZ 85287, USA
E-mail: hmarvi@asu.edu

The ORCID identification number(s) for the author(s) of this article can be found under https://doi.org/10.1002/adma.202003139.

**DOI: 10.1002/adma.202003139**

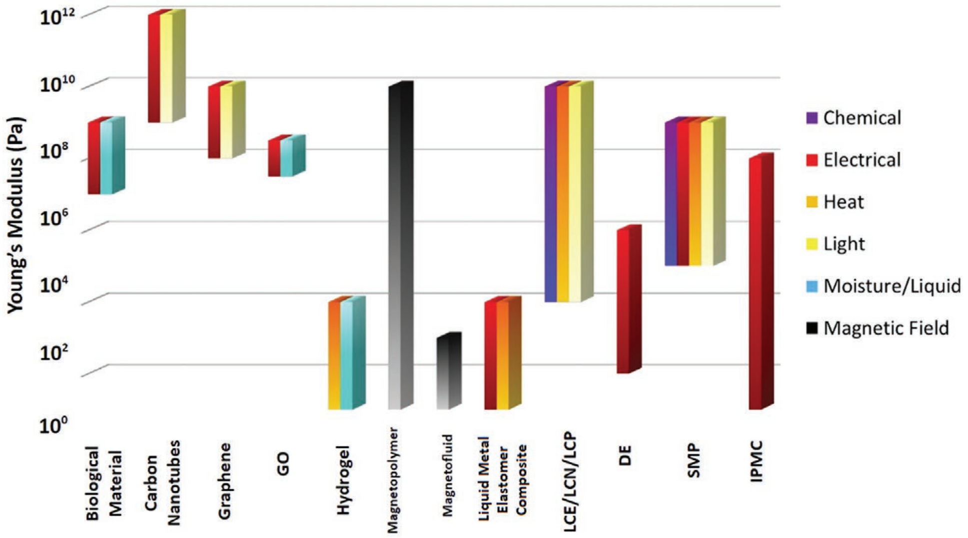

**Figure 1.** Overview of the Young's modulus for bioinspired soft materials is plotted on a log scale, with colored bars denoting the respective stimuli for each. The variation in the Young's modulus for some composite materials is large, due to the wide variety of polymers or elastomers used. Values are approximated. Inspired from refs. [39–45].

### 2.1. Biological Materials

Biology contains materials of every sort: rigid, soft, adhesive, luminescent, brittle, tough, self-healing, and regenerative. With such an abundance of existing solutions, some researchers have sought to directly use these biological materials for robots. In recent research, materials directly grafted from biology to robotics include muscle tissue of Wistar rats grown on substrates,[23,24] silk from spiders[46] and silkworms,[47] plant fibers,[25] DNA,[48] microbial cellulose,[49–51] and layered nanomaterials with marine polysaccharides.[52]

#### *2.1.1. Muscle Cells*

Muscle tissue (**Figure 2**A) exhibits high strain density, a vital metric for efficient actuation. It also self-heals and is electrically activated. Living cells such as cardiac and skeletal muscle cells are among the biological materials directly used in soft robotics. Employing living cells in soft robotic systems has led to the emerging field of miniaturized soft biohybrid robots. Biocompatibility of these small scale robots, along with their unique sensing and actuation capabilities, make them a promising option for healthcare applications such as diagnosing illnesses, drug therapy, and surgery.[53]

In a study, mammalian skeletal muscle was used to actuate a 3D printed hydrogel "biobot." Using electrical stimulation, the biobot achieved a locomotion velocity of over 1.5 body lengths per min.[54] In another study, researchers fabricated photoresponsive bioactuators. When formed into a ring, these tissue actuators generated a contractile force of up to 300 µN per muscle ring.[55] The potential of biological actuators in underwater applications has also been investigated. Researchers introduced a ray fish inspired robot actuated by rat cardiomyocytes. This photoresponsive robot achieved an average speed of around 1.5 mm $s^{-1}$.[56]

It has been shown that muscle tissue can be cultured in wells connecting two joints within an artificial skeletal structure. When grown, the muscle tissue can then be activated by electrical stimulation for effective actuation of the skeletal frame.[23,57] In an attempt to understand if and how biological actuators can be tuned for desired performance, the effects of training protocols on skeletal muscle tissue were studied, and it was found that force outputs can indeed be modulated.[58]

Biohybrid microsystems are capable of both sensing and actuation. They are suitable for untethered applications and can adapt to their environment. On the other hand, the forces generated by muscle cells are limited to several hundred micronewtons and frequencies of up to 5 Hz. Maintenance (temperature of 37°, pH of 7.4, removing byproducts, and resupplying nutrients) is a major disadvantage of using mammalian muscle cells. Moreover, the control of cardiac muscle cells, in particular, is limited due to their self actuating contractions.[59] In addition, if genetically engineered muscle tissues are to be used as actuators for soft robotic systems, then tissue degradation should also be considered one of the limitations.

#### *2.1.2. Plant Fibers*

Plant fibers are known for expanding and contracting due to moisture change, thus achieving actuation. Such materials are responsible for actuating various moving parts found in plants, such as the opening of a pine cone. Actuators using such material properties are termed hygromorph biocomposite (HBC) actuators. HBCs are inexpensive, readily available, and environmentally friendly. The main disadvantage of these fibers for composite reinforcement is their short lifetime due to high water absorption. Moreover, the lack of sufficient knowledge and research on their mechanical behavior hinders high-performance composites.[60–62]

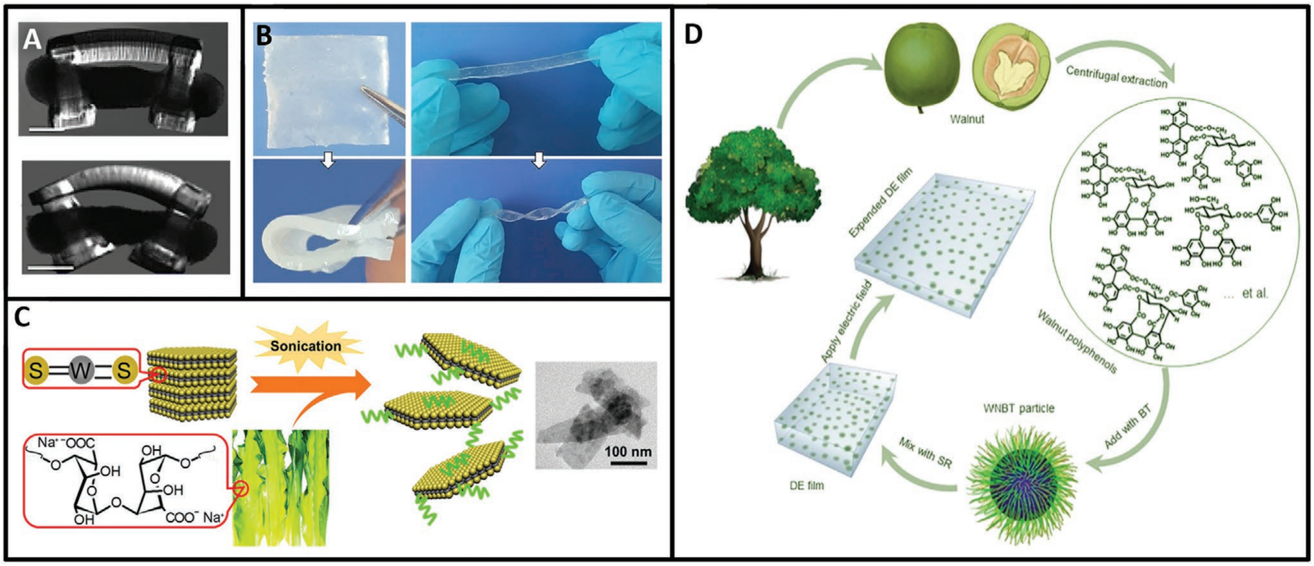

**Figure 2.** Biological materials. A) Muscle tissue composed of differentiated skeletal myofibers in a matrix of natural proteins, grown between two pillars (above: not activated, below: activated). B) Novel shapeable and thermoresponsive composite hydrogel material incorporating polysaccharide guar gum. C) Tungsten dichalcogenides $WS_2$ and marine alginate are coupled to exfoliate the $WS_2$ with a high level of efficiency. D) Toward a dielectric elastomeric material, polyphenolic extract from walnut green husks is used to modify barium titanate particles within a silicon rubber. Rubber treated with the walnut polyphenols exhibits a higher dielectric constant. A) Reproduced with permission.[24] Copyright 2017, Nature Publishing Group. B) Reproduced with permission.[63] Copyright 2020, Elsevier. C) Reproduced with permission.[52] Copyright 2017, Wiley-VCH. D) Reproduced with permission.[64] Copyright 2020, Elsevier.

Recently, the HBC actuation response of flax, jute, kenaf, and coir fiber have been investigated.[25] Jute and flax fibers were concluded as superior for use in HBC actuators. For a moisture change of 50% relative humidity to immersion in water, flax and jute demonstrated 3.3% and 3.6% strain, respectively.[25] Polysaccharides are naturally occurring polymers that have found use in the synthesis of bioinspired robotics materials. Polysaccharides extracted from guar gum have been used to create a thermoresponsive hydrogel by integrating them with FAQRVPP-LDLK12, a self-assembling peptide. The resultant material, shown in Figure 2B, is highly shapeable.[63] In a process described in Figure 2C, polysaccharides from marine alginate have been used to the exfoliation of tungsten dichalcogenides $WS_2$. The exfoliated constituents are photothermally responsive and act as an artificial muscle.[52] Polyphenols, often considered for their dietary and medical applications, are another group of plant-based derivative materials used in soft robots. Polyphenols occurring in green walnut shells have shown to be an effective additive for dielectric elastomeric materials, resulting in a higher dielectric constant as compared to the same material without the added polyphenol (Figure 2D).[64]

### 2.2. Carbon-Based Materials

The term "graphene" refers to a monolayer material of carbon atoms arranged in a hex-shaped lattice resembling a honeycomb. When layers of graphene are stacked, the sheets create graphene paper, a flexible material having Young's modulus ranging from 23 to 42 GPa, and a tensile strength ranging from 15 to 193 MPa, varied by the manufacturing process. Graphene is a result of a series of processes composing of the oxidation of graphite and the exfoliation of GO layers from graphite oxide, followed by the reduction of GO to form graphene.[65,66] The molecular structures of GO and graphene are shown in **Figure 3**A. Graphene exhibits high electrical conductivity, whereas GO is an electrical insulator. The electrical qualities of graphene offer utility for sensing and have been used in bioinspired robotic sensing applications in recent years.[67,68]

Graphite oxide is formed via the oxidation of graphite under strong oxidizing agents in the presence of oxidants. The most common procedures for this oxidation are termed the "Staudenmaier" (utilizing $KClO_3$ (or $NaClO_3$), $HNO_3$, $H_2SO_4$), "Hummers" (utilizing $NaNO_3$, $KMnO_4$, $H_2SO_4$), and "Modified Hummers" (utilizing $NaNO_3$, $KMnO_4$, $H_2SO_4$) processes.[66,69] A quicker, one step method developed by Lee et al. is shown in Figure 3B. In this process, easily soluble graphite is exfoliated by chlorine trifluoride in approximately 5–6 h, as compared with several days in the aforementioned processes.[70] Graphite oxide readily and stably separates into individual GO sheets in water.[65] Oxygen groups attached to the surface of both graphite oxide and GO make these materials hydrophilic. Both tend to expand as water attaches to the hydrophilic groups bonded to the surfaces of individual sheets, pushing them apart. This feature has demonstrated the potential for moisture-responsive artificial muscles used toward bioinspired soft robotics.[26–31]

Graphene, GO, and reduced GO (RGO, highly reduced graphene (HRG)) expand in response to changes in temperature. Thermal expansion of these materials has recently been exploited by many researchers interested in light-activated actuation for artificial muscles.[30,67,71–75] Figure 3C shows a Venus flytrap inspired robot that is photothermally actuated. The

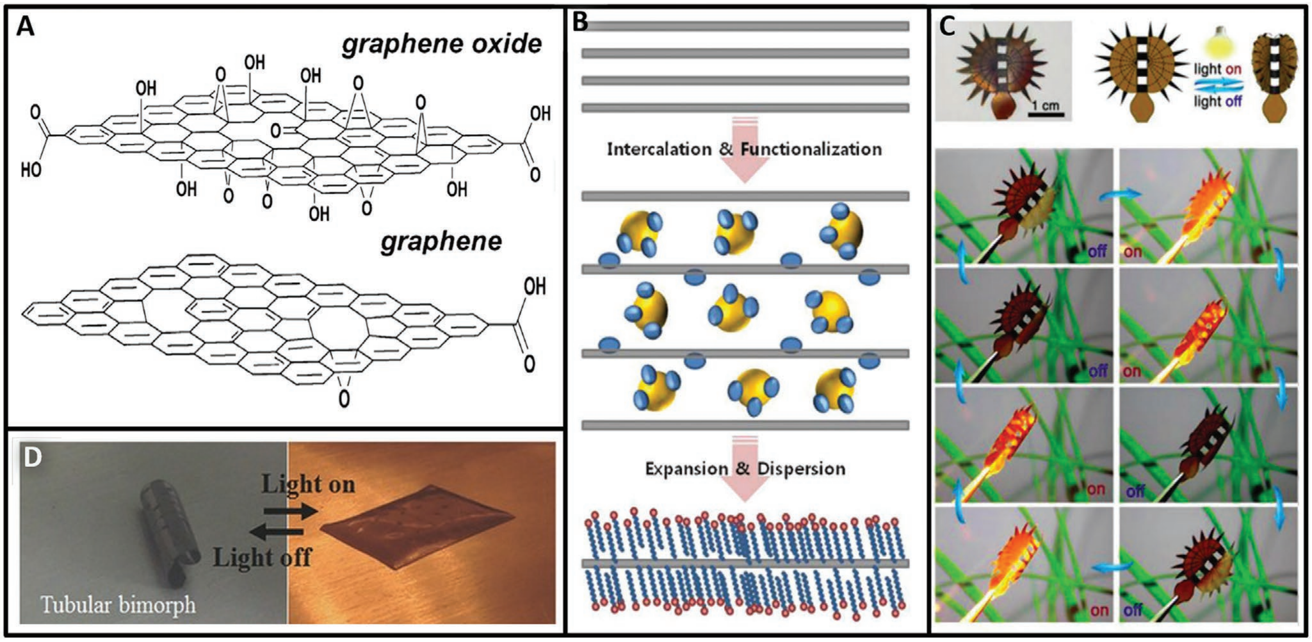

**Figure 3.** Carbon-based materials. A) Molecular diagram of GO (top) and graphene (bottom). B) Diagram of a one-step process used to exfoliate graphene sheets from easily soluble graphite. C) A Venus flytrap inspired photothermal artificial muscle. The muscle is formed from a bilayer structure of poly(methyl methacrylate) and GO compounded with AuNRs. D) Photothermal artificial muscle capable of a deformation angle of around 479° in only 3.6 s. A) Reproduced with permission.[66] Copyright 2010, Wiley-VCH. B) Reproduced with permission.[70] Copyright 2009, Wiley-VCH. C) Reproduced with permission.[76] Copyright 2019, Wiley-VCH. D) Reproduced with permission.[77] Copyright 2015, Wiley-VCH.

mechanism composed of a bilayer structure where two laminated materials have different coefficients of thermal expansion. Though the concept holds for other materials, this iteration uses a bilayer structure of poly(methyl methacrylate) and GO compounded with gold nanorods (AuNRs).[76] Figure 3D further demonstrates this concept, showing the reversible nature of the deformation.[77]

Composite materials formed using RGO have demonstrated high utility toward soft robotics as photothermal materials. Graphene-hydrogel nanocomposite formed by elastin-like polypeptides interfacing with RGO sheets have been demonstrated to act as a photoresponsive composite material.[78] Another graphene-hydrogel composite material is formed by the copolymerization of stearyl acrylate, methacrylic acid, and RGO. Through thermal stimulation (via light) the density is altered, enabling underwater locomotion.[75] In recent years, enhanced strain and moisture-sensitive polymer composite materials have been demonstrated by combining graphene and/or CNT with cellulose nanocrystals or polydimethylsiloxane (PDMS). These composite materials outperform the strain and moisture sensing capabilities of carbon-based materials.[32,33] Carbon-based materials as actuators exhibit high stress and efficiency at low voltage, but low strain outputs. Graphene offers outstanding electrical and thermal conductivity, flexibility, mechanical strength, and high surface area. However, if overheated, individual layers of GO paper may rupture and delaminate as the material thermally expands. This may permanently damage the material's layered structure, causing wrinkling of the layers. Moreover, low actuation strain and short life cycles limit the applications of graphene.[65,79]

### 2.3. Hydrogels

Hydrogels are highly hydrophilic crosslinked polymer networks that are capable of holding large amounts of water. This water-absorbing quality is caused by hydrophilic groups on the polymer chain. The polymer network's crosslinking counters this affinity for water, maintaining the structure and deterring dissolution of the polymer. Interestingly, the polymer used in many synthetic hydrogels is water-soluble when not crosslinked. Hydrogels resemble biological materials in that their composition is mainly water, and in fact, many biological and natural materials are classified as hydrogels. For example, collagen, elastin, fibrin, gelatine, silk fibroin, glycosaminoglycans, alginate, and chitosan are naturally occurring hydrogels based on proteins or polysaccharides.[80] These similarities have caused hydrogels to be sought as a material for simulating or mimicking biological tissue, garnering extensive interest in the arena of soft and bioinspired robotics.[81] Commonly found hydrogels can absorb up to 99 wt% of their dry mass in water, enabling them to exhibit significant swelling and deswelling deformations of more than ten times their original volume. This mechanism can mimic the hydromorphic behavior of plants, and expulsion of the stored moisture can be stimulated with temperature, light, or pH. Although hydrogels require minimal stimuli change to achieve a large volumetric deformation, their applications are limited to aqueous media. In addition, they have a slow response rate, taking several hours for a centimeter scaled piece of hydrogel to deform.[82]

To fabricate hydrogels, a common approach is to apply a thermal stabilization process and subsequent alkaline hydrolysis on a material called polyacrylonitrile (PAN). In 2017, it was demonstrated that by beginning the aforementioned process with a nanofibrous yarn of PAN (produced via an electrospinning process), a similarly microfibrous hydrogel yarn can be formed. This material is uniquely characterized by an aligned polymer network instead of the bulk polymer network other hydrogels exhibit.[83]

Thermoresponsive hydrogels are organized into two groups: positively and negatively thermosensitive hydrogels. Positively thermosensitive hydrogels are characterized by an upper critical solution temperature (UCST) and contract to become effectively hydrophobic as temperature decreases past the UCST. Negatively thermosensitive hydrogels are characterized by a lower critical solution temperature (LCST) and contract as temperature increases past the LCST. Negatively thermosensitive hydrogels are advantageous to medical and implantable purposes because a device or material used for drug delivery can be introduced (at room temperature) to the body and undergo contraction as it warms to body temperature. Among negatively thermosensitive polymers, poly(*N*-isopropylacrylamide) (commonly abbreviated as PNIPAM or PNIPAAM) shown in **Figure 4**A) is of particular interest, despite its fragility. Its structure is well defined, and its tunable LCST is close to human body temperature.[34,35] Figure 4B shows a thermoresponsive hydrogel with a gradient pore structure expanding and contracting in response to changes in temperature.[84]

The usage of hydrogel is highly preferable in applications where biocompatibility is essential. In fact, conductive soft materials are vital for wearable and internal biomedical applications. Figure 4C displays a method of externally attaching a conductive material to a hydrogel substrate via a combination of chemical polymerization and electropolymerization. In this case, conductive poly (3,4-ethylenedioxythiophene) (PEDOT) was attached to the polyurethane hydrogel (PU) substrate. Using this approach, a composite material is made that does not delaminate or detach during moisture activated expansion and drying cycles. As an alternative approach, conductive materials can be impregnated into the internal structure of a soft hydrogel. To form an internally conductive soft hydrogel material, ion-rich hydroxypropyl cellulose (HPC) biopolymer fibers are implanted into a polyvinyl alcohol (PVA) hydrogel (Figure 4D).[85]

### 2.4. Liquid Crystalline Polymers

LCEs are polymer networks that contain components (mesogens) that cause the material to exhibit an intermediate state called the mesophase or the "liquid crystal state." This state is characterized as a middle-ground between solid and liquid

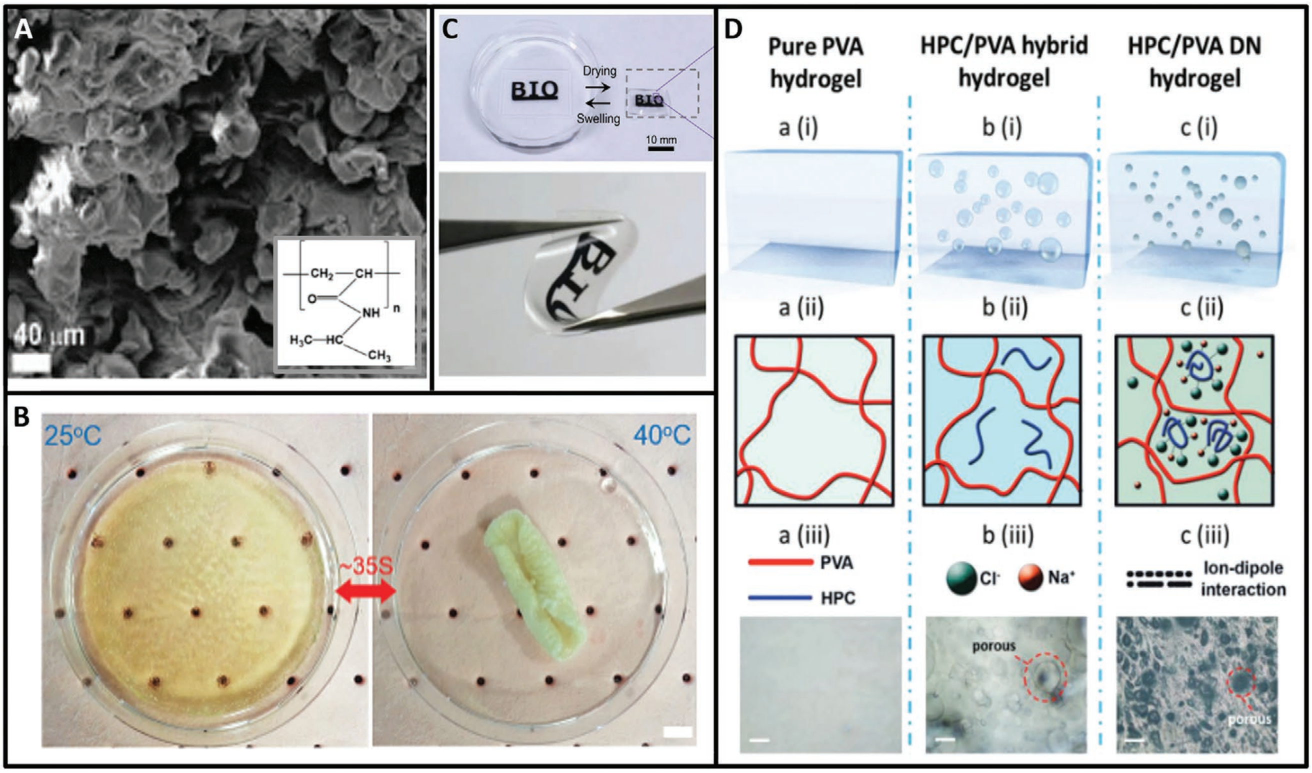

**Figure 4.** Hydrogels. A) Scanning electron microscope (SEM) image of PNIPAM, subpanel showing the molecular structure of the PNIPAM monomer. B) Gradient porous photo/thermal responsive hydrogel, with tunable mechanical properties and reversible temperature based deformation. C) PEDOT and polyurethane/hydrogel hybrid material that exhibits similar conductive qualities when either swollen or dry. The material is soft and flexible, promising for biomedical applications. D) Electrically conductive, soft, and stretchable material formed with PVA hydrogel matrix embedded with ion-rich HPC biopolymer fibers. A) Reproduced with permission.[86] Copyright 2019, MDPI. Subpanel A) Reproduced with permission.[87] Copyright 2020, MDPI AG. B) Reproduced with permission.[84] Copyright 2015, Wiley-VCH. C) Reproduced with permission.[88] Copyright 2014, Wiley-VCH. D) Reproduced with permission.[85] Copyright 2019, Wiley-VCH.

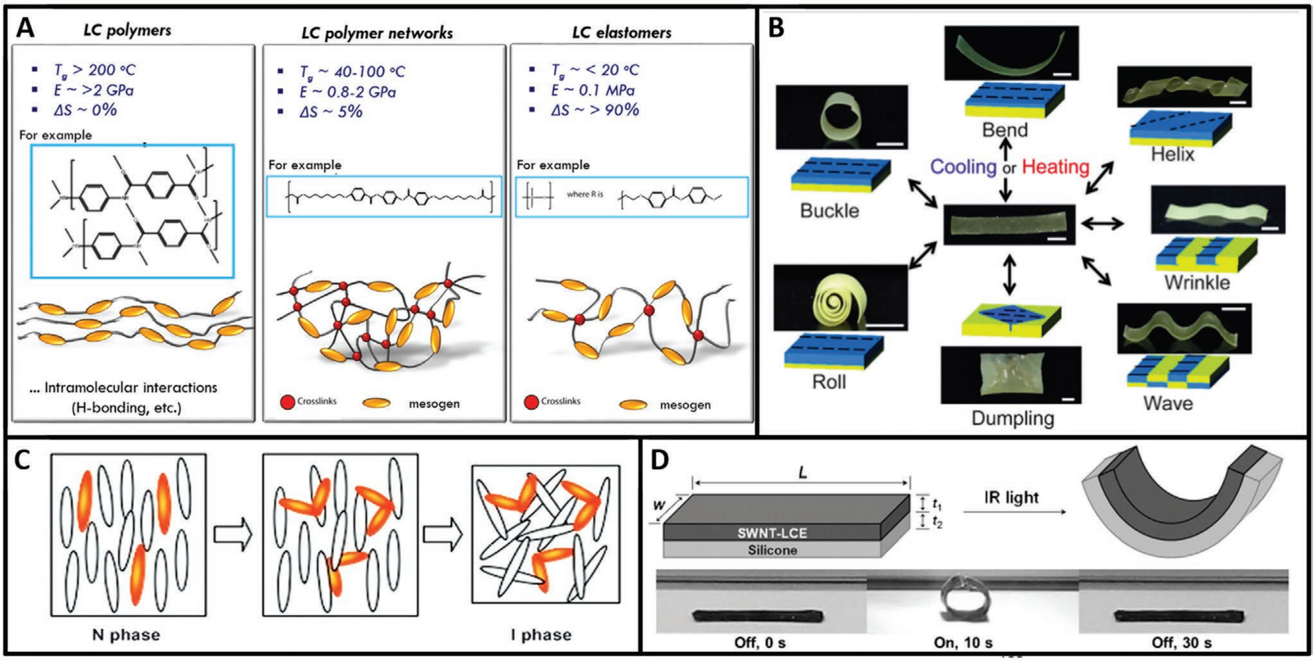

**Figure 5.** LCPs. A) Classification of LCPs. LCPs are linearly structured and stiff polymers that contain mesogens (left); LCNs are nonlinearly structured mesomer containing polymers, highly crosslinked, and softer than LCPs; LCEs are loosely crosslinked and nonlinearly structured mesogen containing polymers. B) Selectively photocrosslinked LCE materials thermally deform in highly customizable ways. The differences in actuating behavior are due to geometric differences in the regions of the material that undergo phase transitions. C) The Nematic and Isotropic phases of liquid crystalline materials. In the nematic phase (N-phase, left), the mesogens tend to become aligned in the direction of the nematic director, similar to a crystalline structure. In the isotropic phase (I-phase, right), the material collapses into a disordered state, similar to a liquid. D) A photoresponsive actuator composed of a bilayer composite of LCE and silicone. A) Reproduced with permission.[89] Copyright 2018, Wiley-VCH. B) Reproduced with permission.[90] Copyright 2017, Wiley-VCH. C) Reproduced with permission.[91] Copyright 2006, Wiley-VCH. D) Reproduced with permission.[94] Copyright 2013, Wiley-VCH.

states, where individual components of a substance can be structured as in a solid (crystalline), but the substance may flow like a liquid. In LCEs, the liquid crystalline state is a result of mesogen inclusions within an elastomer network. Mesogens can join the network as part of the main polymer chain itself, be attached as a side chain, or be combined with another polymer inclusion.[36] Liquid crystal polymers (LCPs) are often characterized by their level of crosslinking. Liquid crystals (LCs) exhibiting linear structures, such as the polymer described in the leftmost column of **Figure 5**A (Kevlar). LCPs can denote a more broad umbrella term used to describe polymer networks containing mesogens. Liquid crystal networks (LCNs) are softer than LCPs and characterized by their high levels of nonlinear crosslinking structure, such as the material shown in the centermost panel of Figure 5A. LCEs, shown in Figure 5A (right), are less crosslinked than LCNs and nonlinear, displaying the "softest" characteristics of the three classifications.[89] Furthermore, during the manufacturing of the material, local photocrosslinking can be performed in application-specific patterns that allow liquid crystalline materials to behave in a highly customizable manner. Figure 5B shows LCEs that have been selectively photocrosslinked in a variety of patterns, achieving a range of geometrically different thermoresponsive deformations.[90]

Illustrated in Figure 5C, LCEs exhibit two distinct states that characterize their utility. One where the mesogens or other LC components exist in the nematic phase (N-phase). Another where they exist in the isotropic phase (I-phase).[91] The LCE material itself may be referred to be in one or the other phase colloquially, when in fact, the terms refer to the state of the mesogen components. In the nematic phase, the LC components tend to align in a particular direction, yet are not subject to any sequential or crystal arrangement. The direction in which the LC units align in the nematic phase is termed the "nematic director." This defines the axis through which the material contracts during the reversible transition from the nematic phase to the isotropic phase. To force the transition from the nematic phase to the isotropic phase, the LCE material's temperature must be increased. In recent research, this temperature increase has been achieved by either exposing the material to nonmesogenic solvents or by applying ultraviolet (UV) radiation to it.[92,93] Figure 5D illustrates a photoresponsive bilayer actuator composed of an LCE laminated onto a layer of silicone.[94]

LCEs are capable of shape-fixing and shape-restoring responses. Moreover, they can be designed to be actuated by a wide range of stimuli. In addition, LCEs can self-organize as a homogeneous material and mechanically transform into different spatial orientations and geometries. However, LCEs require high temperatures (above 100 °C) to actuate. They also suffer from poor mechanical properties and their low blocking stress (below 500 kPa) limits their application.[95,96]

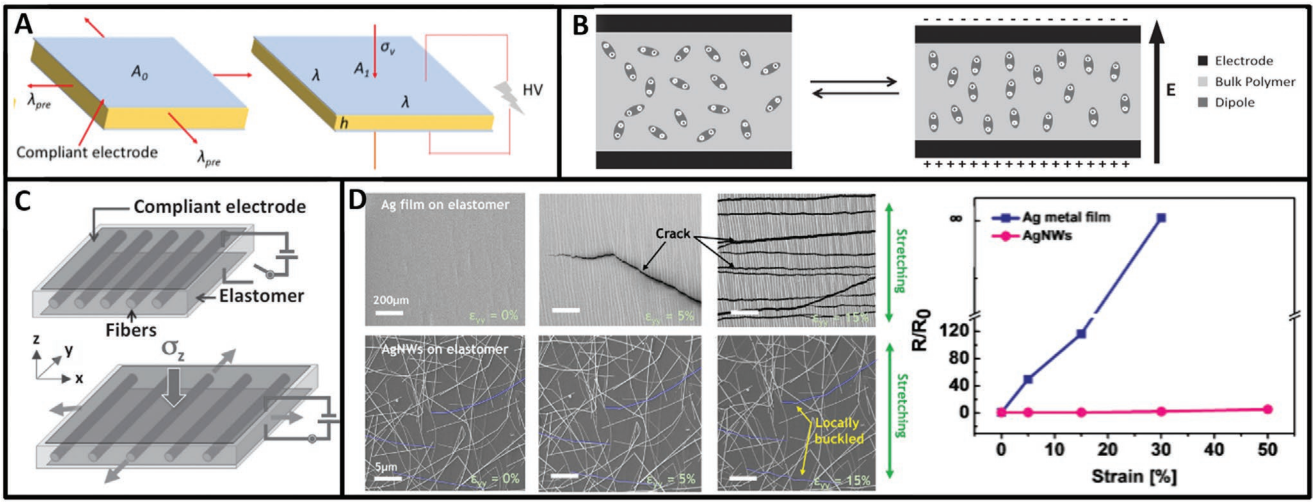

**Figure 6.** DEs. A) Diagram of DE's basic function. As a voltage is applied across the parallel plate capacitor, the capacitor is compressed. This compression causes internal elastomer to become vertically squished, expanding the elastomer horizontally in all directions. B) Randomly distributed dipole groups on the polymer chain within the DE materials become aligned within the electric field, applying stress on the polymer network. The DE compresses, and the material expands outward to compensate. C) Structural fibers can be implanted into a DE to increase its strength or to force the material to deform in a certain direction. D) SEM images of two different varieties of electrodes used in DEs: deposited Ag film (top left) cracks when the DE is activated, due to stretching of the brittle Ag film. Ag nanowires (bottom left) do not rupture but instead are allowed to bend and buckle locally. A comparative plot (right) shows the relationship between planar resistance as a function of DE strain. A) Reproduced with permission.[64] Copyright 2020, Elsevier. B) Reproduced with permission.[97] Copyright 2015, Wiley-VCH. C) Reproduced with permission.[99] Copyright 2014, Wiley-VCH. D) Reproduced with permission.[103] Copyright 2016, Wiley-VCH.

### 2.5. Dielectric Elastomers

DEs are a form of electroactive polymers (EAPs) generating mechanical work upon electrical stimulation. Coulomb force is indeed responsible for DE actuation. In particular, Coulomb forces emerge when an electric field is applied across the plates of a parallel plate capacitor, pulling the plates toward one another. If a compliant yet incompressible dielectric polymer is placed between the two attracting plates, the coulomb forces will deform and expand the polymer outward as it is squeezed between the two plates. This provides a mechanism for actuation, as illustrated in **Figure 6**A.[64] Furthermore, randomly distributed dipole groups on the polymer chain align themselves under the influence of the applied electric field, adding to the mechanism of deformation (Figure 6B).[97] DEs are promising for bioinspired applications due to their ability to reproduce muscle properties such as actuation strain (10–100%) and stress (0.1–8 Mpa). DEs are readily available and have large work and power density. Other advantages of DEs include their self-sensing capacity, operation simplicity, and high energy density. However, DEs require high working voltages compared to low voltage materials such as CNTs and IPMCs.[98] Acrylic elastomers and silicone are the most popular materials used for the elastomeric membrane. Acrylic films need to be prestretched and are sensitive to humidity and temperature change. As a silicone membrane, PDMS shows better functionality in humid environments and over a wider range of temperatures. Another iteration of bioinspired DE materials calls for implanting of fibers within the elastomer. This inclusion adds strength to the material and biases the deflection to be normal to the "grain" direction of the fibers. Such a material is shown in Figure 6C.[99] Carbon-based materials (e.g., carbon powders, carbon greases, and carbon composites) are the typical choices for electrodes, because of their great compliance.[100] Developing nonconventional electrodes for DEs is another active area of research. For instance, Wang et al. used a mixture of poly(3,4-ethylenedioxythiophene): poly(styrenesulfonate) (PEDOT:PSS) and waterborne polyurethane (WPU) as compliant electrodes. Unlike carbon-based electrodes, this material is transparent, enabling the transmittance of the visible light spectrum through the DE.[101]

The electrode material is often not as compliant as the DE. Due to this discrepancy in softness, the electrode material will tend to form microcracks as the DE deforms. These cracks cause a loss of electrical conductivity in the plane of the electrode plate. Figure 6D shows the formations of cracks in deposited Ag as the electrode deforms (top left), and a plot of planar resistance loss as a function of strain (right). As an alternative, Ag nanowires can be used as a more effective electrode, which does not lose significant conductivity caused by deformation (bottom left).[102,103]

### 2.6. Ionic Polymer–Metal Composite

IPMCs are composite materials formed by sandwiching an ion-exchange membrane (IEM) between two chemically coated electrode layers. When current passing across the electrodes and the IEM, the material deforms due to swelling caused by an uneven saturation of electrolyte molecules within the IEM. This phenomenon is detailed in **Figure 7**A. The molecules of the electrolyte, most commonly water, are attracted to the cation

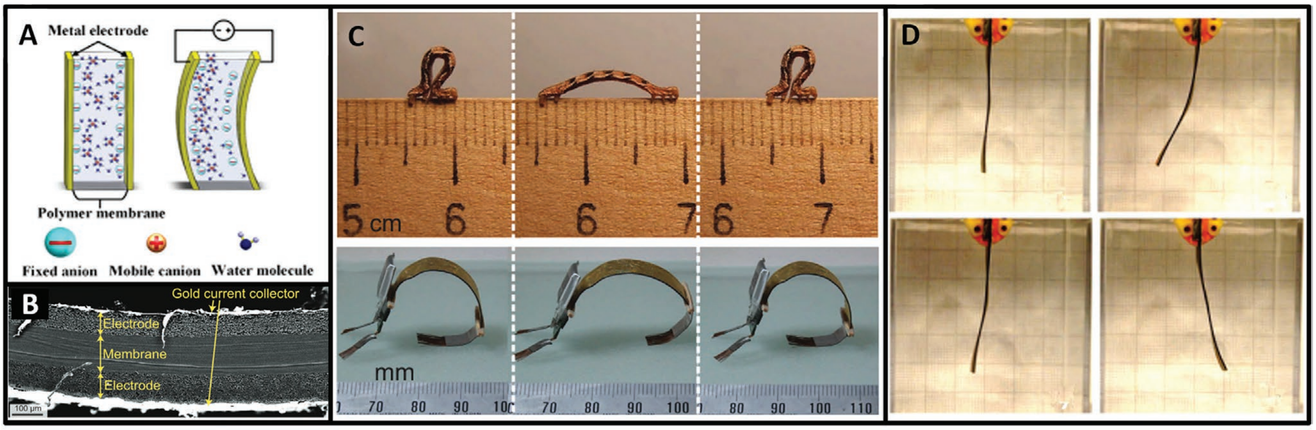

**Figure 7.** IPMCs. A) The actuation mechanism of an IPMC film. Two flexible electrodes sandwich an IEM. A voltage applied through the IEM causes ions to migrate to one side of the membrane. This inhomogeneity causes bending actuation in the film. B) SEM image of an IPMC. The IEM is sandwiched between two electrodes and marked. C) Inchworm inspired crawling IPMC robot. D) Free-hanging IPMC material demonstrating that reverse-direction actuation is possible by reversing the polarity of the applied electric field. A,D) Reproduced with permission.[108] Copyright 2016, Nature Publishing Group. B,C) Reproduced with permission.[113] Copyright 2015, Wiley-VCH.

side of the IPMC, causing hydrophilic expansion of the polymer network near the cathode and shrinkage near the anode. As a result, the material is bent.[38]

The electrodes are most commonly made of platinum due to its resistance to corrosion though alternative materials can be used, such as palladium, gold, silver, carbon, graphite, nickel, lead, copper, and iridium.[104] In Figure 7B, an SEM image of the cross-section of an IPMC utilizing gold plated carbon-based electrodes is shown, where the three layers (two layers of electrodes and one layer of IEM) can be distinctly seen. For the amount of strain that the material generates with its low actuation voltage, IPMC is often used in small-scale soft robots.

IMPCs require low voltages and provide large displacements. They have fast response rates (microseconds to seconds) while showing a long lifetime (in orders of $10^7$ cycles), and are relatively inexpensive ($20 per $\text{cm}^2$). Depending on their IEM, IPMCs cover a wide range of Young's modulus (Figure 1); however, they are generally lightweight and compliant materials (Young's modulus of ≈200 MPa). Despite their advantages, they suffer from limitations such as low output forces, solvent evaporation, instability due to the relaxation of IPMC, and hydration in periodic contact with water.[105–107]

The material in Figure 7B is used to create an inchworm inspired robot shown in Figure 7C. By alternating the polarity of the applied electric field, an IPMC material can be made to sway in opposite directions, as demonstrated in Figure 7D.[108] Recently, it has been shown that IPMCs can be 3D printed to form intricately shaped actuators. Utilizing machine learning techniques, negative effects caused during the manufacturing process can be mitigated, such as inconsistencies and filament grain in the final product.[109]

The IEMs in IMPCs are polymers that are specially designed to allow ions to pass through them. The mechanical strength of an IEM material is determined by its long polymer backbone. Its ion exchange capabilities are determined by its active ionic side chains. Different ionic side chain groups can be attached to the main chain to selectively allow the passage of cations or anions through the membranes.[110] IEM materials used in IPMCs are chosen from a selection of perfluorinated ionomeric polymer membranes that are commercially available, including Nafion, Xion, Flemion, Fumasep, and Aciplex.[104] Furthermore, IPMCs must operate below the electrolysis voltage of the electrolyte to avoid gas formation.[111,112]

## 3. Bioinspired Soft Actuators

Actuators are one of the main components of robotic systems and thus, have received extensive attention from researchers aiming to enhance their efficiency[114,115] and dexterity.[116–118] Recently, researchers have focused their attention on nature-inspired designs[119–121] as well as on the implementation of soft materials.[122–124]

Plentiful examples of biosystems undergoing transformation in response to external stimuli can be found in nature, such as pine cones,[125] plant tendrils,[126] and wheat awn,[127] to name a few. The wide range of stimulation responses and diverse functionality have made biological actuation systems an appealing source of inspiration for the development of artificial actuators.[128] In addition, the desire for actuators to attain their full potential has engaged significant research effort toward the design and development of soft actuators.[39,129] Successful studies on actuation mechanisms,[39] material selection,[130] and creative design implementations[131] affirm the potential of this field. Acknowledging the interests in soft bioinspired actuators, a survey of recent studies on soft actuators and their bioinspired applications is presented, categorized according to their mechanism of actuation. Regarding the numerous smart materials introduced to soft bioinspired technologies,[132–135] a wide range of stimuli-responsive actuators have been reported.[136,137] The stimuli presented here are water, pH, thermal, light, magnetic, electric, and the combination of those mentioned. A schematic of these stimuli is presented in **Figure 8**. In addition,

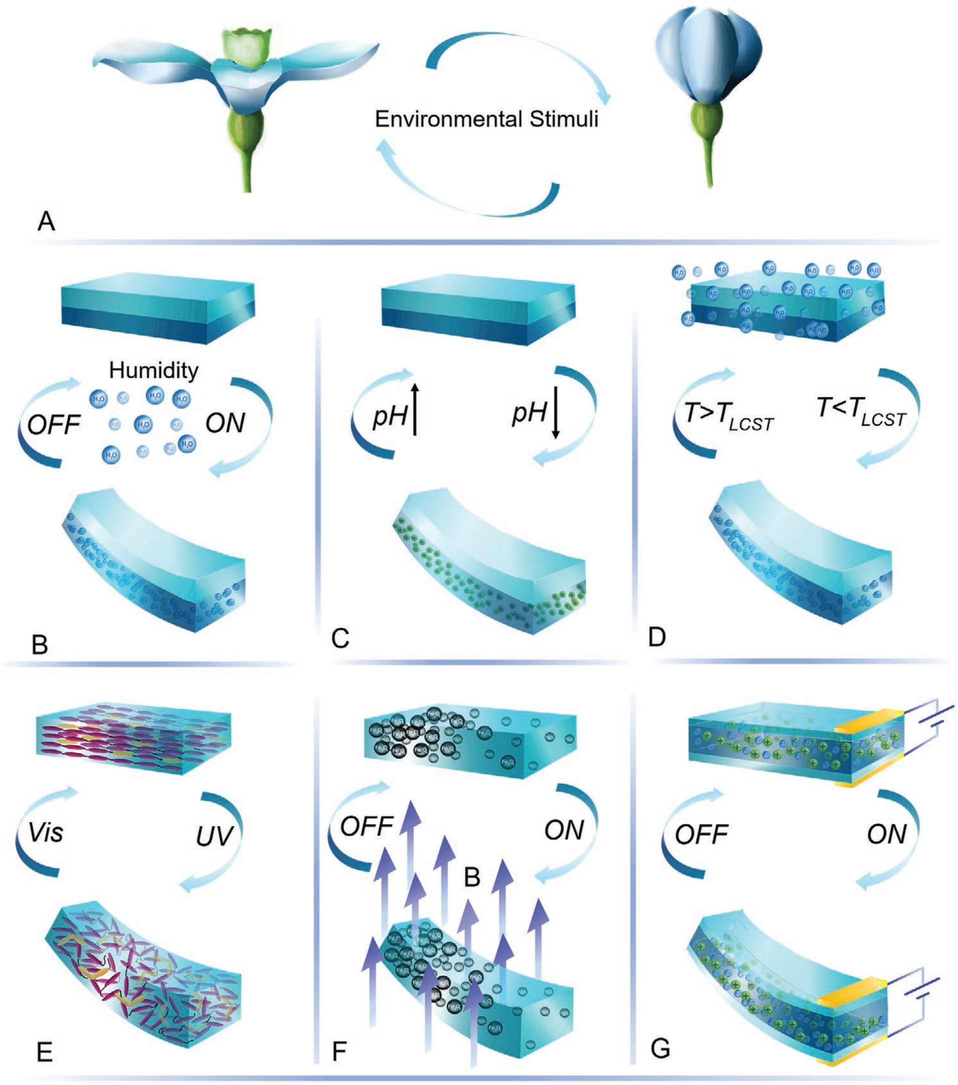

**Figure 8.** Bioinspired soft actuators made of soft smart materials. A representative response mechanism to different stimuli is shown; however, the mechanisms are not limited to these. A) Schematic of a bioinspired soft flower with petals being potentially actuated using the mechanisms demonstrated in (B–G) panels. B) water-responsive actuator. Illustration of bilayer structure composed of a water-responsive layer such as hydrogel along with an inactive layer. C) pH-responsive actuator. Illustration of bilayer actuation based on polybases swelling/deswelling in response to changes in pH in their environment. D) Thermoresponsive actuator. An example of employing thermoresponsive hydrogels in a bilayer structure to develop a bioinspired soft actuator. E) Photoresponsive actuator. Illustration of using light-responsive switches in LCE to enable photoresponsiveness. F) Magnetic responsive actuator. Using a nonuniform distribution of magnetic responsive particles in a polymeric matrix. G) Electrical responsive actuator. Particularly, the deformation of an IPMC in response to the applied electric field is illustrated.

the mechanisms, applications, performance, and sources of inspiration for these bioinspired actuators are summarized in **Table 1**.

### 3.1. Water-Responsive Actuators

Water stimulus can be in the form of liquid (moisture) or vapor (humidity). Moisture gradients and humidity changes are widespread phenomena in nature. Various types of plants such as *Mimosa pudica* and pine cones respond to water stimuli.[125] These plants, also known as hygromorphs,[138] owe their water-responsive and shape-changing properties to their bilayer structure. Each layer responds differently to water stimulus, resulting in an anisotropic deformation in the bilayer structure.[139] This mechanism has inspired scientists to develop actuators that respond to such stimuli.[140]

#### 3.1.1. Anisotropic Interplanar Expansion

Among the different materials investigated for the fabrication of moisture responsive actuators, GO has become very popular. The oxygen-containing functional groups in GO accumulate water molecules and enhance water adsorption properties.[141] Throughout the adsorption process, GO experiences changes

**Table 1.** Summary of bioinspired soft actuators and applications, their source of inspiration, and technical information.

| Stimulus | Mechanism | Bioinspiration | Deformation | Applications | Response rate | Performance | Reference |
|---|---|---|---|---|---|---|---|
| Water | Expansion of GO layer in GO/RGO bilayers | Cilia of respiratory | Bending | Controlled object transport | (12 mm × 1 mm × 11.5 µm) 25° → 100° in 7 s and recovery in 5 s | The average bending and straightening forces of ≈0.63 mN and ≈0.35 mN, respectively | [30] |
| | | Tendril climber plant | Twisting | Biosensors | 0° → 160° with 30° s$^{-1}$ | (4.5 mg, 12 mm thick) able to lift 35.5 mg to a height of 0.8 cm in 8 s with a work output of 0.64 J kg$^{-1}$ and a power density of 0.08 W kg$^{-1}$ | [26] |
| | | Nacre | | Wound dressings | | | |
| | | Water lilies | | Energy-harvesting devices | | | |
| | | Pitcher plant | | Humidity responsive motors | (Bilayer with the thickness of 18.3 µm) Curvature of –0.047 cm$^{-1}$ → 0.175 cm$^{-1}$ in 55 s and recovery in 45 s | NA | [28] |
| | | Wheat awns | | Artificial articular cartilages | | | (Figure 9A–C) |
| | | Pine cones | | Robots of different forms: flower, claw, crawler, tendril, butterfly | (1.5 mm × 15 mm) 0 cm$^{-1}$ → 1.48 cm$^{-1}$ in 10 s | NA | [31] |
| | | Seed dispersal | | Motions of different forms: flip, flap, fold, bloom | 0 → 145° in 1.2 s and recovery in 1.6 s | NA | [146] |
| | | *Bacillus* spores | | | (2 cm × 2 cm × 60 µm) frequency f ≈ 34 min$^{-1}$, A motor with a speed of 2.5 cm s$^{-1}$ | (1.4 cm × 0.5 cm × 0.037 mm and weight of 4.8 mg) lift objects 50 times heavier to the height of 1.2 cm in 16 s with a work output of 6.17 J kg$^{-1}$ and a power density of 0.39 W kg$^{-1}$; transport cargos 10 times heavier | [29] |
| | | | | | (3.5 cm × 1.0 cm × 10 µm) 0° → 180° in 1 s | (3.5 cm × 1.0 cm × 10 µm) contractile stress up to 42.3 MPa | [145] |
| Water | Swelling and deswelling of polymer-based bilayers | Plant tendrils | Bending | Smart switch | (5 mm × 10 mm) 0° → 140° → 0° in 5 s | (10 mg film) Lifting a 0.29 g weight up to 6 mm in 3 s, 2.4 g up to 2 mm, work performance 47 µJ | [150] |
| | | Plant fibers | Twisting | Transporter | Curvature 0 cm$^{-1}$ → 4 cm$^{-1}$ → 0 cm$^{-1}$ in 1 min | Gripper lifting 30 times its own weight | [153] |
| | | Lotus leaf | S-shape | Generator | One full cycle of locomotion in 5 min | (25 mg film) Lifting objects 380 times heavier, transport cargo 10 times heavier (lifting 9.5 g load to a height of 2 mm within 3 s, the work output 7.6 J kg$^{-1}$, power density 2.5 W kg$^{-1}$) | [159] |
| | | Pinecone | Ω-shape | Gripper | Locomotion speed of 6 mm s$^{-1}$ | Robot carry a load 50 times its weight | [152] |
| | | Awns of wild wheat | Helical-shape | Continuous locomotion | 0° → 180° → 0° in less than 1 s | NA | [50] |
| | | Erodium | | Blooming flower | | | (Figure 9D,E) |
| | | Chrysina genus of beetles | | | (2 cm × 2 mm × 80 µm) uniform circle in 200 s | (2.5 cm × 1.0 cm × 60.0 µm, 28.9 mg) lifting 130.5 mg to a height of 3.0 cm, the work output for lifting the object is 39.2 µJ | [157] |
| | | *Mimosa pudica* | | | (Thickness of 8 µm), curvature 0 cm$^{-1}$ → ≈0.8 cm$^{-1}$ in 150 s | NA | [142] |

**Table 1.** Continued.

| Stimulus | Mechanism | Bioinspiration | Deformation | Applications | Response rate | Performance | Reference |
|---|---|---|---|---|---|---|---|
| | | Dionaea muscipula | | | | | |
| | | Venus flytrap | | | | | |
| | | *Selaginella lepidophylla* | | | | | |
| Water | Yarn-shape | Pine cones | Torsional deformation | Automatic ventilation | Delivering a 52% stroke during 12 min at an isobaric load of 2.3 MPa and recovering in 3 min | Gravimetric work capacity 2.17 kJ $kg^{-1}$, volumetric work capacity 1.8 MJ $m^{-3}$, lifting 12 g mass (12000 times heavier than the actuator weight) | [147] |
| | | Seed dispersal | | Hydro-generator | Rotational speed of 1125 rpm | Work capacity of 73 J $kg^{-1}$ and volumetric energy density of 172 kJ $m^{-3}$ | [148] |
| | | *Bacillus* spores | | Smart textiles | Rotational speed of 13000 rpm | Output rotational kinetic energy of $1.48 \times 10^4$ W $kg^{-1}$, Lifting weight 3000 times heavier than its own weight | [149] |
| | | Silkworm silk | | Smart rainy curtain | | | |
| | | Pinecones | | Breathable fabric | | | |
| | | Mimosa | | Smart crane | | | |
| pH | Ionization of functional groups | Pine cones | Bending | Grippers | Curvature ≈1.4 $cm^{-1}$ → $1.2^{-1}$ in 160 s and recovery in 320 s | NA | [172] |
| | | Wheat awns | Rings | Smart encapsulators | (micropost: diameter = 1.5 µm, height = 10 µm, square array with pitch = 8 µm) Actuation in fractions of second | NA | [160] (Figure 10A) |
| | | Orchid tree seedpods | Tubules | Lenses | | | |
| | | Cilia in human respiratory tract | Flower-, helix-, bamboo-and wave-like shapes | Actuating surfaces, Microfluidics | | | |
| | | Echinoderms | S-shape | Propulsion, Cargo transport | (1.5 mm thickness) Radius of curvature 2.2 cm → 1 cm in 250 min | NA | [161] (Figure 10B) |
| | | | Ω-shape | Engineer living cell-based microactuators | | | |
| | | | | Controlled/triggered molecule delivery | | | |
| | | | | Circuit switch | Curvature 0.05 $mm^{-1}$ → 0.25 $mm^{-1}$ in 40 s and recovery in 35 s | NA | [169] |
| Light | Photochemical | Gecko toe hairs | Twisting | Photocontrollable micro-structured transport device | Controllable adhesion force between 0.73 ± 0.23 mN and 0.27 ± 0.03 mN | NA | [190] |
| | | Plant tendril | Winding | Rapid release | NA | Provided work = 3.04 J $mol^{-1}$ of azobenzene and a power of 9 nW | [191] |
| | | Chiral seedpod | Helical-shape | Underwater locomotion modes, such as crawling, walking, jumping, and swimming, | Width 770 mm, length 1.2 cm), and the total operation process takes about 40 s | NA | [185] (Figure 12A) |
| | | Sea slug and snail | Bending | | | | |

**Table 1.** Continued.

| Stimulus | Mechanism | Bioinspiration | Deformation | Applications | Response rate | Performance | Reference |
|---|---|---|---|---|---|---|---|
| | | | | | (16 mm × 3 mm × 0.1 mm) vertical swimming with an almost constant velocity of 4.9 mm s$^{-1}$ during the stroke period | NA | [187]<br>(Figure 12C) |
| Light | Photothermal | Worm locomotion | Bending | Multimodal locomotion | Crawling speed of 0.7 mm s$^{-1}$ | NA | [195] |
| | | Caterpillar locomotion | Stretching | Crawl on ground | NA | (Circular shaped structure with diameter of 28 mm) 12 mm deflection corresponding to curvature of 0.33 cm$^{-1}$ under the illumination intensity of 106 mW cm$^{-2}$ in 3 s | [186] |
| | | Fruit fly larva jumping | | Squeeze through small channels | | | (Figure 12D) |
| | | Inchworm | | Jump over barriers | (1.2 cm × 0.5 cm × 10 µm) bent to 90° in 2 s and recover in 5 s | The walking process: bend to its maximum in 2.4 s, stretch 3.8 s. Walking distance 4 mm | [74] |
| | | Human finger | | Infrared and sunlight-driven curtain | Recovering ≈74–84% in 10 s | 75° under exposure of NIR laser with 5.7 W cm$^{-2}$ power density | [78] |
| | | | | Infrared actuated self-folding box | locomotion speed of ≈2.4 µm s$^{-1}$ | (0.3 g robot) Carrying a 15 g weight on a flat surface, 3.8 g weight on an uphill. | [193] |
| | | | | Worm-like locomotion | bending at a speed of 17° s$^{-1}$ | step length of 1/10 of body length (0.6 mm) | [194] |
| | | | | Finger-like flexing | | | |
| Heat | Change in hydrophobicity | *Urechis unicinctus* | Bending | Gripper | Bending 0° → 360° in 49 s | Lifting a 5.67 g cargo to a height of 3.35 cm | [180] |
| | | Venus flytrap | Sectional shrinking | Flower | Snap-thourgh actuation in less than 0.5 s (The whole operation takes few min) | NA | [181] |
| | | Water self-circulation of mimosa leaves | Bowl-shape | Instability triggering for applications such as: drug delivery, microfluidic control system, and soft biomimetic robotics | (40 mm × 10 mm × 2 mm) Curvature 0 mm$^{-1}$ → 1.2 mm$^{-1}$ in 5 min | NA | [35]<br>(Figure 11E,F) |
| | | | | | Gripper from open to close: in water within 3 min, recovery in 20 min, in oil within 2 min, recovery in 20 min, and in air within 2 min, recovery in 20 min | Lift and carry a cargo of 1 g | [183] |
| Heat | Phase change | Inchworm | Bending | Hook-shape actuator | ≈55% strain in 30 min for a uniaxial LCE | Lifting 10 times heavier than its own weight | [178] |
| | | Caterpillar | S-shape | Crawling | (28.6 mm × 7.7 mm × 0.5 mm, 0.29 g) crawling speed of 1.91 mm min$^{-1}$ | NA | [282] |
| | | Gecko toe hairs | Elongation | Gripper | | | |
| | | Mimosa | Spiral spring | Shape-changing with finger-touch | (1.3 mm × 2 mm × 0.188 mm) Cantilever deformation, 1.8 mm $^{-1}$ | Maximum work density of 8.4 kJ m$^{-3}$ | [173]<br>(Figure 11A) |
| | | Water lily | Spiral ribbon | Flowering process on the palm | | | |

**Table 1.** Continued.

| Stimulus | Mechanism | Bioinspiration | Deformation | Applications | Response rate | Performance | Reference |
|---|---|---|---|---|---|---|---|
| | | Octopus | Curling | Flowering with breath-blowing | Mimosa inspired leaves open to close in 12 s and<br>Lift 10 times heavier than its own weight | NA | [306] |
| | | | Pin-shape | Opening/closing with/without light | | | |
| | | | | Caterpillar locomotion | | | |
| Magnetic | Magnetic force/torque | Cilia | Bending | Wireless power for electronics | Triggering actuation takes 1.32 s, the snap-through takes 0.2 s | Required triggering force 41.46 N | [226] |
| | | Amoeba | Tilting | Programmable microswitches | From flat to concave in 0.112 s | Required triggering force 0.0636 N | [225] |
| | | Bacteria | Elongation | Switching surface wettability | Average water transportation speed of 46 ± 9 and 32 ± 6 mm $s^{-1}$, with and without methylene blue dye, respectively | NA | [223] |
| | | Lotus leaf | Contraction | Gripper | | | |
| | | Indian cress leaf | Combination of the above | Autonomous, intelligent microrobotics | | | |
| | | lady's mantle leaf | | Pump free microfluidic device | | | |
| | | Venus flytrap | | Portable platform for lab-on-a-chip | 3 µL droplet transportation for 1.8 mm in 237 ms | Tilting angle from 0° to 60° with the increase of intensity of magnetic field from 0 to 1 Tesla. | [214] |
| | | Nepenthes peristome | | Ferrofluid-based molding | | | (Figure 13A) |
| | | Octopus | | Multiflagellated nanoswimmers | The speed of the specimens is calculated to be in the range of 0.15–0.37 mm $s^{-1}$ | Body length per cycle: inchworm 0.025, turtle 0.087, quadruped 0.012, millipede 0.011 | [228] |
| | | Chameleons | | Long-range liquid transport | | | |
| | | Gecko toe hairs | | Self-cleaning and water repellency | For experimental case, both of the legs had a stride speed of 1.67 mm $s^{-1}$ and moved 5 mm after one crawling cycle. | | [215] |
| | | Inchworm | | Swimming robot | Each crawling cycle was about 3 s long. | The maximum load carrying capacity on a smooth surface is 5.95 g, which is about 30 times its own mass. It is also able to carry a load 1.5 times its body weight while stably climbing on a 45° inclined surface | (Figure 13C) |
| | | Caterpillar | | Locomotion | | | |
| | | Butterfly | | Medical robot | | | |
| | | Serrated microstructure of mantises' forelegs, | | Linear locomotion and crawling | NA | Angle of 80° under 35 mT | [230] |
| | | | | Pick-and-place and cargo-release tasks | NA | Average speed of 0.3 µm $s^{-1}$ for helical and curly swimmers @ 3 Hz. average speed of 1 µm $s^{-1}$ for coiled swimmers @ 8 Hz. | [216] |

**Table 1.** Continued.

| Stimulus | Mechanism | Bioinspiration | Deformation | Applications | Response rate | Performance | Reference |
|---|---|---|---|---|---|---|---|
| | | | | | | | (Figure 13D) |
| | | | | | NA | Maximum work 1913 μNm | [203] |
| | | | | Pick-and-place and cargo-release tasks | NA | Average speed of 0.3 μm s$^{-1}$ for helical and curly swimmers @ 3 Hz. average speed of 1 μm s$^{-1}$ for coiled swimmers @ 8 Hz. | [216]<br>(Figure 13D) |
| | | | | | NA | Maximum work 1913 μNm | [203] |
| Electric field | Electrostatic forces | Annelid | Bending | Locomotion | (120 mm × 170 mm, 10 g) a 3-segment robot can reach an average speed of 5.3 mm s$^{-1}$ (1.871 body lengths/min) | Actuation frequency of 0.5 Hz: 4.12% Body length/cycle and speed-mass ratio 20.39 mm min$^{-1}$ g$^{-1}$ | [307] |
| | | Venus flytrap | Twisting | Swimming | From 32 degrees to fully close in 0.25 s | Expansion of 32° @ 5 kV input voltage | [258] |
| | | Insects | | Gripper | Average speed of 5.2 cm s$^{-1}$ @ 7 Hz actuation frequency | Inchworm locomotion 0.25 BL/s @ 10 Hz actuation, 4-legged locomotion 0.115 BL/s @ 1.5 Hz actuation | [262] |
| | | Inchworm | | Low power, Silent operation- in underwater environments | Average swimming speed 19 mm s$^{-1}$ @ 0.25 Hz with 5 kV input voltage | Actuator able to increase the projected area by 66% → improve peak thrust by 34.5% | [264] |
| | | Frog | | | Average speed of 3.2 mm s$^{-1}$ | NA | [268] |
| | | Jellyfish | | | Maximum speed of 1.8 (tethered) and 3.2 mm$^{-1}$ (untethered) | Maximum deflection of 10 mm, Force of 6.1 mN, and Work output of 16 μJ | [240]<br>(Figure 14B) |
| Electric field | Joule heating | Elephant trunk | Multidirectional bending | Multifunctional soft gripper | Bending 0 → 85° in 30 s, recovery in 270 s @3.0 V | Capable of lifting 50 g object | [283] |
| | | Octopus arm | Contraction | Untethered soft robot | 25% contraction in 120 s | Maximum work density of 9.2 J kg$^{-1}$ | [287] |
| | | Starfish feet | | | Crawling locomotion: stride cycle takes 60 s, Average speed: 1.91 mm min$^{-1}$ | NA | [241]<br>(Figure 14C) |
| Electric field | Motion of ions | Gecko | Bending | Switchable adhesion | Flapping cycle of 2 s (upstroke and down stroke) | Create 2.4 grams of force @ 4 V DC. | |
| | | Beetle | | Wall climbing | | Displacement under 4.5 V and different frequencies: 6.5 mm @ 0.5 Hz, 4.1 mm @ 1 Hz, and 3.1 mm @ 1.5 Hz | [308] |
| | | Fish | | Flapping air vehicle | NA | For different voltage inputs (1, 1.5, and 2 V), the normal adsorption forces are 5.52-, 14.2- and 23.13-fold bigger than the desorption forces. | [309] |
| | | Butterfly | | Swimming | Swimming speed up to 0.45 BL/s | Small turning radius: less than half a body length | [290] |
| | | Anomalocaris | | | Turning left and right up to 40° s$^{-1}$ | | |
| | | Dragonfly | | | Anomalocaris swimmer: Average swimming speed 2.3 mm s$^{-1}$ @ 2 Hz and 3.7 V, | Butterfly robot: Right wing flapping @ 5.8 Hz, 3 V; Left wing flapping @ 7.9 Hz, 3 V | [310] |
| | | | | | Bending speed of 224.2 mm s$^{-1}$, >10 Hz response rate under AC voltage | Tip displacement 35.3 mm, lift objects 20 times heavier | [242]<br>(Figure 14D) |

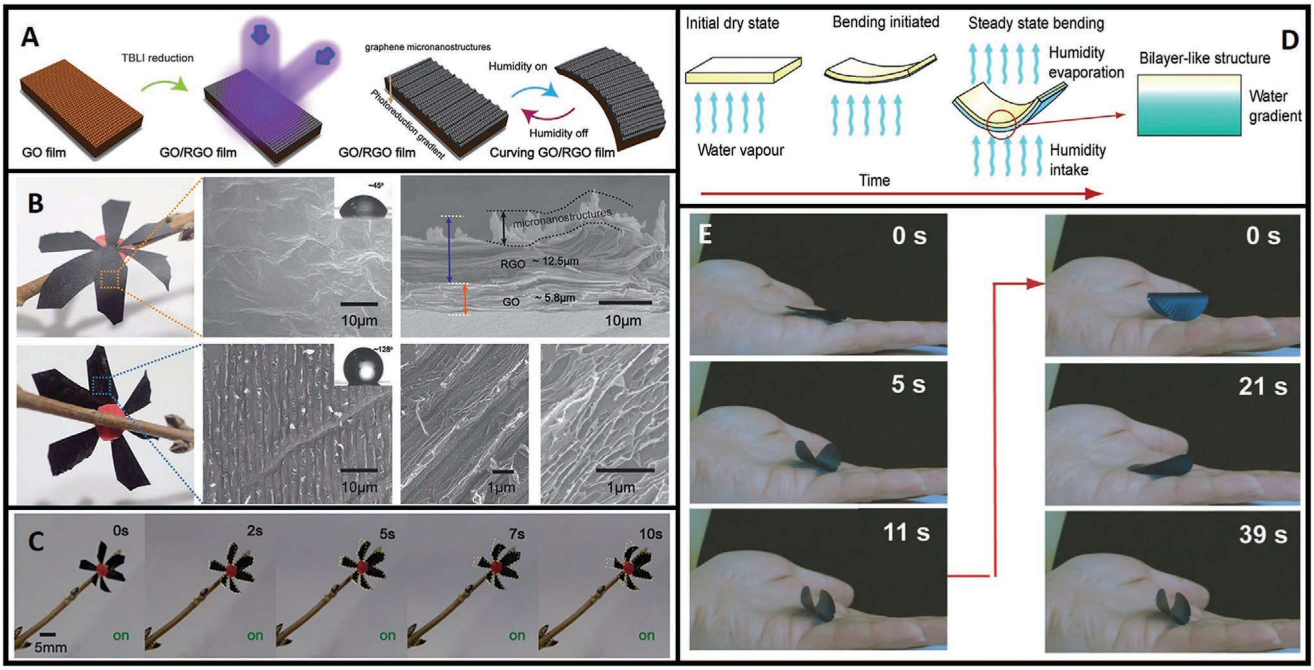

**Figure 9.** Water-responsive actuators. A) Fabrication of a GO/RGO bilayer film using the TBLI method and demonstration of its reversible actuation. B) SEM images of the front and back of the GO/RGO bilayer structure. C) Snapshots of a GO/RGO flower robot. D) Illustration of actuation of a film with cellulose nanofibers. E) Experimental demonstration of reversible actuation. A–C) Reproduced with permission.[28] Copyright 2019, Frontiers. D,E) Reproduced with permission.[142] Copyright 2015, Wiley-VCH.

in interlayer spacing when exposed to water either as vapor or liquid. Researchers have taken various approaches to employ this property in soft actuation. One of which is the development of an anisotropic structure through oxygen reduction of the GO layers, nonuniformly throughout its thickness (**Figure 9**B). Removing the oxygen content reduces its ability to adsorb water. When the GO/RGO actuator is exposed to moisture or humidity, the GO layer adsorbs water and expands, causing the structure to curve. There are processes using chemical, thermal, and other methods to reduce the oxygen content of a GO layer. One such method that enables nonuniform reduction uses UV irradiation on thick GO layers. This method relies on the fact that the oxygen content of a thick GO layer cannot be fully reduced, due to the limited light transmittance. With controlled irradiation, different actuation modes can be achieved with patterned GO/RGO structures. Han et al. demonstrated that the actuators fabricated using this method can perfectly mimic the behavior of respiratory tract cilia and tendril climber plants.[30] Another method used to produce the anisotropic GO/RGO structures is unilateral two-beam laser interference (TBLI). This technique can reduce the oxygen content of the GO layers and cut them into grating-like periodic RGO microstructures (Figure 9A).[28] Anisotropic actuation of homogeneous GO layers can be achieved by using nonuniform water stimuli, such as humidity gradients.[26] While this simplifies the fabrication process (i.e., avoidance of multilayer structures), the actuator functionality is limited to an optimal surface thickness and temperature.

While the utilization of GO for moisture responsive actuators has attracted much attention, these actuators lack mechanical strength. To solve this issue, researchers took inspiration from nacre-like structures, considering their extraordinary mechanical properties.[143,144] These studies have led to the development of many actuators with nacre-like structures.[29,31,145] Besides improving mechanical properties, the idea of developing composite GO actuators has led to additional functionalities. Inspired by water lilies, Xiang et al. developed a 3D structure made of GO layers, poly(vinyl alcohol-*co*-ethylene) (PVA-*co*-PE) nanofibers (NFs), and silver nanowires (AgNWs). This structure offers an enhanced moisture exchange rate, larger deformations under stimulation, and improved conductivity.[146]

In addition, researchers have introduced yarn-shaped structures as an alternative design for these actuators.[147,148] Kim et al. fabricated yarn-shaped synthetic muscles using hybrid CNT, inspired by *Bacillus* spores. These structures are made of twisted CNT sheets and hydrophilic poly(diallyl dimethylammonium chloride) (PDDA). This actuator demonstrates up to 78% tensile stroke, 2.17 kJ kg$^{-1}$ gravimetric work, and 1.8 MJ m$^{-3}$ volumetric work capacity in response to water absorption or change of ambient relative humidity. [147]

### 3.1.2. Anisotropic Swelling

As an alternative to using GO for moisture responsive actuators, polymer-based actuators have also been investigated. It has been shown that different modes of motion can be achieved using these actuators, such as twisting,[149,150] bending,[151,152] and s-shaped and spiral motions.[153] Water-responsive polymers have achieved anisotropic deformation by using foreign molecules and/or multilayer structures consisting of an active polymer and a hygroscopically inactive layer. The active polymer layer expands and shrinks during the absorption and desorption of water, respectively, while the inactive layer remains unchanged. Hydrogel, a superabsorbent polymer, is a good choice of active material for actuation purposes. Hydrogels can absorb large amounts of water and expand quickly; however, they show poor flexibility, slow recovery, and low stress generation. Moreover, their applications are limited to aqueous environments.[154,155]

Using alternative polymers and designs, flexible, fast, and efficient polymer-based actuators have been developed. Polyimide (PI), poly(ethylene glycol), and PVA are among the most popular materials used to enhance the flexibility of bilayer structures. Inspired by *Mimosa pudica* and pine cone, Zhu et al. fabricated actuators using poly(vinyl alcohol-*co*-ethylene) (EVOH) nanofibers and cellulose nanocrystals (CNC). Their actuator maintained its efficiency, even after 100 cycles.[156] Inspired by the *Selaginella lepidophylla*'s stem structure, Tan et al. fabricated soft actuators composed of sodium alginate (SA) and PVA. Using this actuator, they achieved an energy conversion efficiency of 81.2% at 25 °C.[157] Besides the bilayer structures, the aligned microstructures of the plants have a significant role in their actuation and response time. Cellulose materials (cellulose nanofibers, cellulose nanocrystals, bacterial cellulose) are super hydrophilic nanostructures that can enhance response time (Figure 9D,E).[142,156,158] The curvature and the response time of the actuators can be controlled by tuning the thickness and the amount of CNC. Moreover, the chosen alignment of CNCs enables different actuation modes such as bending and twisting.[156] In addition to the improved response time, the research on composite actuators has led to additional properties and functionalities. Ma et al. developed a fast reversible actuator inspired by the network structure of the animal dermis. The resultant polymer composite actuator offers significant mechanical deformations, large forces, and high work density, making it a suitable choice for a wide range of applications, such as switches and piezoelectric power generators.[159]

Although there have been many studies on developing water-responsive actuators, there are challenges in implementing them for robotic applications. These challenges include: 1) Developing actuators with quick responses and agile behavior, while still providing desired power; 2) Producing actuation without artificial modifications to environmental humidity, which is preferable for autonomous purposes; 3) Generating directed motion for robotic applications; 4) Establishing mathematical models to study the actuators' behavior, which is essential for control purposes and design optimization. Researchers have been working to improve these shortcomings and prepare water-responsive actuators for robotic applications One such study uses a bilayer structure soft robot inspired by motile plants. It is made of hygroscopically responsive film and hygroscopic poly(ethylene oxide) (PEO) nanofibers. Capable of creeping, crawling, and slithering motions, it reflects movements found in worms, snails, and snakes.[152]

### 3.2. pH-Responsive Actuators

Despite their benefits, humidity and moisture gradient responsive actuators are not practical in fluidic environments such as "lab-on-a-chip" and microfluidic applications. In contrast, pH-responsive actuators are suitable for applications in such environments. These actuators employ materials that deform (e.g., swell and deswell) in response to the changes in pH. This deformation commonly results from pH dependant ionization of the material's functional groups and the electrostatic repulsion between similar charges. Researchers found this self-response property suitable for developing bioinspired soft actuators.[162] Advances in synthetic polymers with different architectures and chemical structures have enabled researchers to fabricate pH-responsive actuators for a wide variety of applications. These active polymers fall into two categories: polymers with basic and acidic groups.[163]

#### 3.2.1. Ionization of Acidic Groups

Carboxylic groups such as poly(acrylic acid) (PAAc) and poly(methacrylic acid) (PMAAc),[164] sulfonic acid such as poly(2-acrylamido-2-methylpropane sulfonic acid) (PAMPS) and poly(4-styrenesulfonic acid) (PSSA),[165] phosphonic acid,[166] and boronic acid[167] are the most frequently used acidic groups to develop pH-responsive acidic polymers. Inspired by microorganisms that use flagella for propulsion, researchers fabricated a polymer network using acrylic acid (AAc) as the pH-responsive element along with an acrylamide (AAm)-based hydrogel. The resultant hydrogel swells at pH > 4.25 as it undergoes water infiltration when experiencing an increased osmotic pressure due to AAc ionization. At pH < 4.25 the acrylate protonates and the hydrogel contracts (**Figure 10**A).[160]

#### 3.2.2. Ionization of Basic Groups

Various active groups have been used to develop basic polymers, including tertiary amine such as poly(*N*-(dimethylamino) (PDMA),[168] morpholino such as poly[(2-*N*-morpholino)ethyl methacrylate] (PMEMA), and pyridine groups such as poly(4-vinylpyridine) (P4VP), to name a few. PDMA is a tertiary amine methacrylate-based polymer which has received great attention because of its thermoresponsive and pH-responsive behavior. Using a layer of PNIPAM as a temperature-sensitive material along with a pH-responsive layer of poly(2-(dimethylamino) ethyl methacrylate) (PDMAEMA), reversible and repeatable response is achieved with the change in solution temperature and pH.[169] Using PNIPAM to develop a temperature and pH-responsive actuator, Li et al. showed that the actuation performance can be tuned by controlling the composition of the hydrogel.[170]

#### 3.2.3. Ionization of Natural Acidic and Basic Polymers

A recent trend in developing pH-responsive polymers is using biodegradable and biocompatible natural polymers such as dextran, hyaluronic acid (HA), alginic acid, chitosan, and gelatine for biomedical purposes.[171] Inspired by the bilayer structure of plants, Duan et al. fabricated a biohydrogel actuator for biomedical applications. The actuator's structure consists of polymers with acidic and basic groups, granting functionality

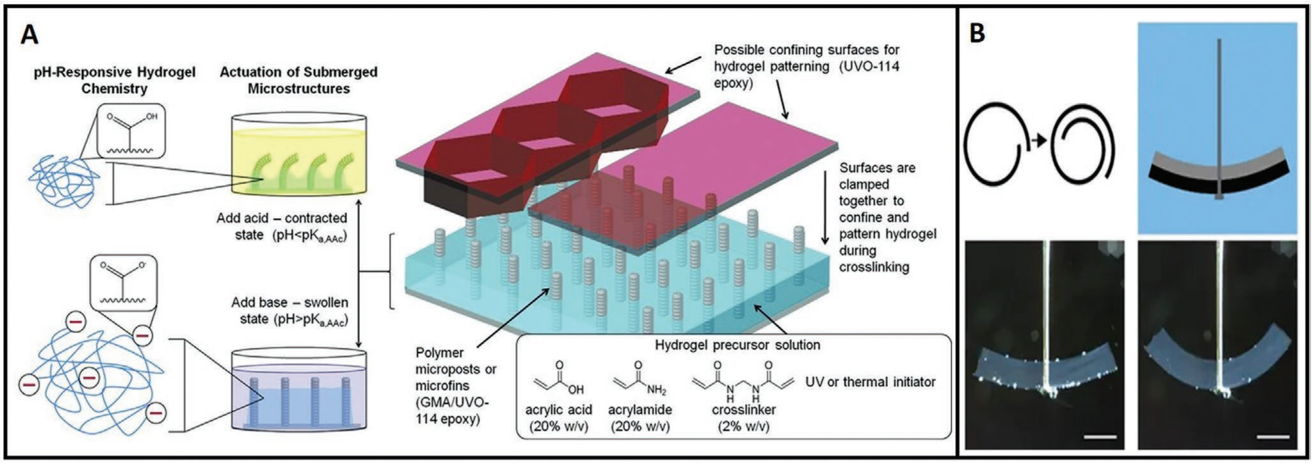

**Figure 10.** pH-responsive actuators. A) Left to right: Chemistry of a hydrogel actuator; actuation of microstructures; and fabrication process of pH-responsive microstructures. B) Schematic illustration of a stent (top-left) and the gelatine bilayer actuator (top-right). Snapshots of the bilayer actuator before (bottom-left) and after actuation (bottom-right); The scale bar is 5 mm. A) Reproduced with permission.[160] Copyright 2011, Wiley-VCH. B) Reproduced with permission.[161] Copyright 2017, Nature Publishing Group.

in high and low pH. By using a cellulose/carboxymethylcellulose layer (swelling in basic pH) and chitosan layer (swelling in acidic pH), they demonstrated bidirectional actuation.[172] Using gelatine layers irradiated with electron beams, Riedel et al. fabricated a bilayer pH-responsive actuator. They showed that the irradiation modifies the swelling properties of gelatine, which produces anisotropic deformation when used in a bilayer configuration (Figure 10B).[161]

The structural design of pH-responsive actuators goes beyond layered structures. For example, researchers sought to emulate the mechanical properties and flexibility of yarn. Wu et al. introduced nanofibers to PAN-based hydrogel yarn to enhance the response of hydrogel actuators. Their hydrogel yarn exhibits a fast response to pH stimuli with a maximum change of 100% in length and 900% in diameter.[83]

### 3.3. Thermoresponsive Actuators

Although numerous water and pH driven actuators with outstanding functionalities have been developed, they are not practical for a range of applications in dry or water-sensitive environments. This has urged researchers to invest in developing dry actuators. Among these dry actuators, thermoresponsive actuators have the advantage of enabling various actuation mechanisms as they respond to a wide range of heat generation methods such as exothermic reactions, photothermal heating, Joule heating, and magnetocaloric effects. Furthermore, these actuators are known for their capability of presenting large volume and shape changes. While they are suitable for dry environments, numerous thermoresponsive actuators have also been designed to function in wet environments.

#### *3.3.1. Material Phase Change*

Liquid crystals (LC) are a popular material choice for thermoresponsive bioinspired soft actuators as they show large and reversible deformations when crosslinked to form LCEs or LCNs. Crosslinked liquid crystals allow for the control of macroscopic shape-changing via molecular reorientation of liquid crystal molecules called mesogens. Temperature change is one method to induce this molecular reorientation. LCs experience a reversible phase transition when their temperature goes above the isotropic phase transition temperature. In this case, the mesogens get randomly aligned, leading to a random coil conformation in the polymer chains.[36,112,175,176] Utilizing a LCN-based thermoresponsive soft actuator, Shahsavan et al. were able to mimic self-peeling of gecko toes (**Figure 11**A).[173]

Considering the potential of LC-based thermal actuators, researchers are attempting to enhance their programmability and functionality. In one of these studies, researchers introduced a method for fabricating LCE robots solely by integrating multiple LCE actuators. These seamless 3D LCE structures increase the dexterity and multifunctionality of the robot. Their technique consists of welding and aligning LCE materials with different chemical compositions and physical properties.[177] The new generation of thermoresponsive actuators require stable reprogramming abilities. To achieve this goal, researchers have introduced switchable reprogrammability for LCE-based thermoresponsive actuators. In addition, by creatively designing the structural architecture of reprogrammable actuators they can be used for different modes of actuation.[178]

#### *3.3.2. Material Solubility Change*

As previously mentioned, thermoresponsive actuators are not limited to dry environments. There have been many studies on wet environments, particularly using hydrogel-based thermal actuators. Thermoresponsive polymers are a class of smart polymers that exhibit reversible deformation in response to changes in temperature. Negatively thermoresistive polymers characterized by LCST experience a rapid and reversible solubility change in an aqueous solution, which leads to complete

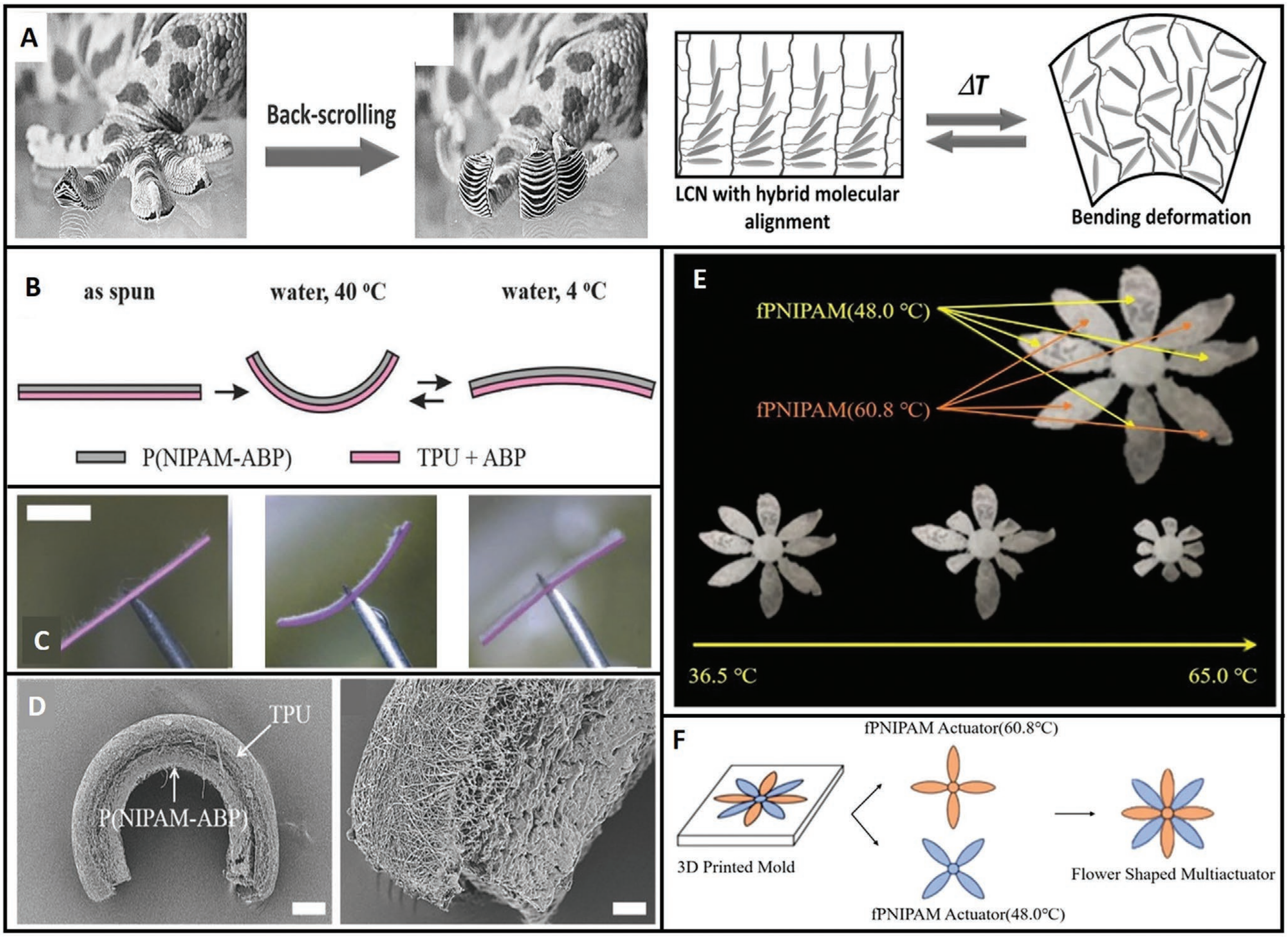

**Figure 11.** Thermoresponsive actuators. A) Images of gecko toes in gripping and releasing modes. Shape-changing mechanism of an LCE-based actuator in response to a thermal stimulus. B) Schematic representation of thermal actuation using a bilayer structure. C) Experimental demonstration on a TPU40-NIPAM15 sample. D) Microstructure of the bilayer after actuation. E) Flower blossom-shaped sequential actuation and F) schematic illustration of its fabrication process. A) Reproduced with permission.[173] Copyright 2017, Wiley-VCH. B–D) Reproduced with permission.[174] Copyright 2015, Wiley-VCH. E,F) Reproduced with permission.[35] Copyright 2019, Nature Publishing Group.

hydration at temperatures below LCST. PNIPAM and its derivatives are the LCST-type polymers that have extensively been used to develop the thermoresponsive actuators.[179] The crosslinked PNIPAM swells and deswells in the water below and above LCST, respectively. The response time of these actuators varies from seconds for very thin actuators to minutes for centimeter thick actuators (Figure 11B–D).[174] Inspired by the fluid-induced actuation behavior of *Urechis unicinctus*, Lin et al. developed a thermoresponsive hydrogel tube. This tube is composed of thermoresponsive PNIPAAm$_x$-PAA$_y$ and nonresponsive PAM$_x$-PAA$_y$. By controlling the design of the responsive and nonresponsive geometries, different actuation modes were achieved.[180] Although PNIPAM hydrogels are fragile, there have been many studies to improve their mechanical properties for actuation purposes.[34] Preparation methods such as double-network (DN) and ionic-covalent entanglement (ICE) have been successfully used to fabricate strong hydrogels.[181,182] Using UCST- and LCST-type polymers together, researchers have developed hydrogel-based actuators performing in dry environments. Zheng et al. introduced a water self-circulation mechanism inspired by *Mimosa* leaves. Employing this mechanism, they developed a hydrogel-based reverse thermal responsive actuator made up of a bilayer structure.[183]

PNIPAM based actuators are limited to two modes of actuation: above and below their LCST. To circumvent this limitation, researchers developed multiresponsive actuators by employing these PNIPAM based actuators along with different responsive actuators. While the PNIPAM based actuators suffer from two modes of actuation, copolymerization with functional monomers has been used to change the LCST to a desired temperature. By tuning the LCST, Kim et al. introduced a thermoresponsive actuator which can be implemented beyond a binary on/off actuator. Hydrophobic monomers shift the LCST to a lower temperature, while hydrophilic monomers shift the LCST to higher temperatures. Using this technique, they fabricated a bioinspired artificial flower with two distinct LCSTs (48° and 60.8°) (Figure 11E,F).[35]

### 3.4. Photoresponsive Actuators

Light is considered one of the most promising stimuli for bioinspired soft actuators, for they enable 1) noncontact actuation, 2) selective and precise actuation through wavelength and intensity control, and 3) high-resolution temporal and spatial control.[184] Various materials and techniques have resulted in photoresponsive actuators responding to different wavelengths from UV to near-infrared (NIR), triggered directly (photochemical) or indirectly (photothermal).

#### *3.4.1. Photoisomerization of Azobenzene Units*

Light illumination can directly affect polymers with photoresponsive functional groups (photochromic groups) at the molecular level in a way that leads to macroscopic deformation.[188,189] One of the methods for producing photochemical actuators is to introduce photoresponsive switches to a polymer network. Azobenzene units are one of these switches that respond to UV light by undergoing photoisomerization, which is widely used in bioinspired soft actuation. The molecular dimension of azobenzene units changes under 320–380 nm UV light irradiation, which is reversible by the illumination of 420–480 nm light.[190] Inspired by the plant tendrils, Iamsaard et al. fabricated spring-like photoresponsive actuators by introducing azobenzene units into an LC polymer. The actuation mechanism relies on the azobenzene's geometrical isomerization as energy converters were integrated into the polymer network. The molecular orientation of the LC gradually shifts to 90° from the bottom surface to the top surface. After fabricating a film of polymer, different actuation modes as illustrated in **Figure 12**A, were achieved by cutting ribbons of the film in different angles with respect to the orientation of molecules in the mid-plane.[191] With a similar technique, the opening of a seedpod was mimicked using two paired polymers stripped with opposite twisting directions. The stress between these two strips makes them fall apart during the actuation.[185]

Researchers found it favorable to incorporate these actuators along with other mechanisms to create versatile actuators. One

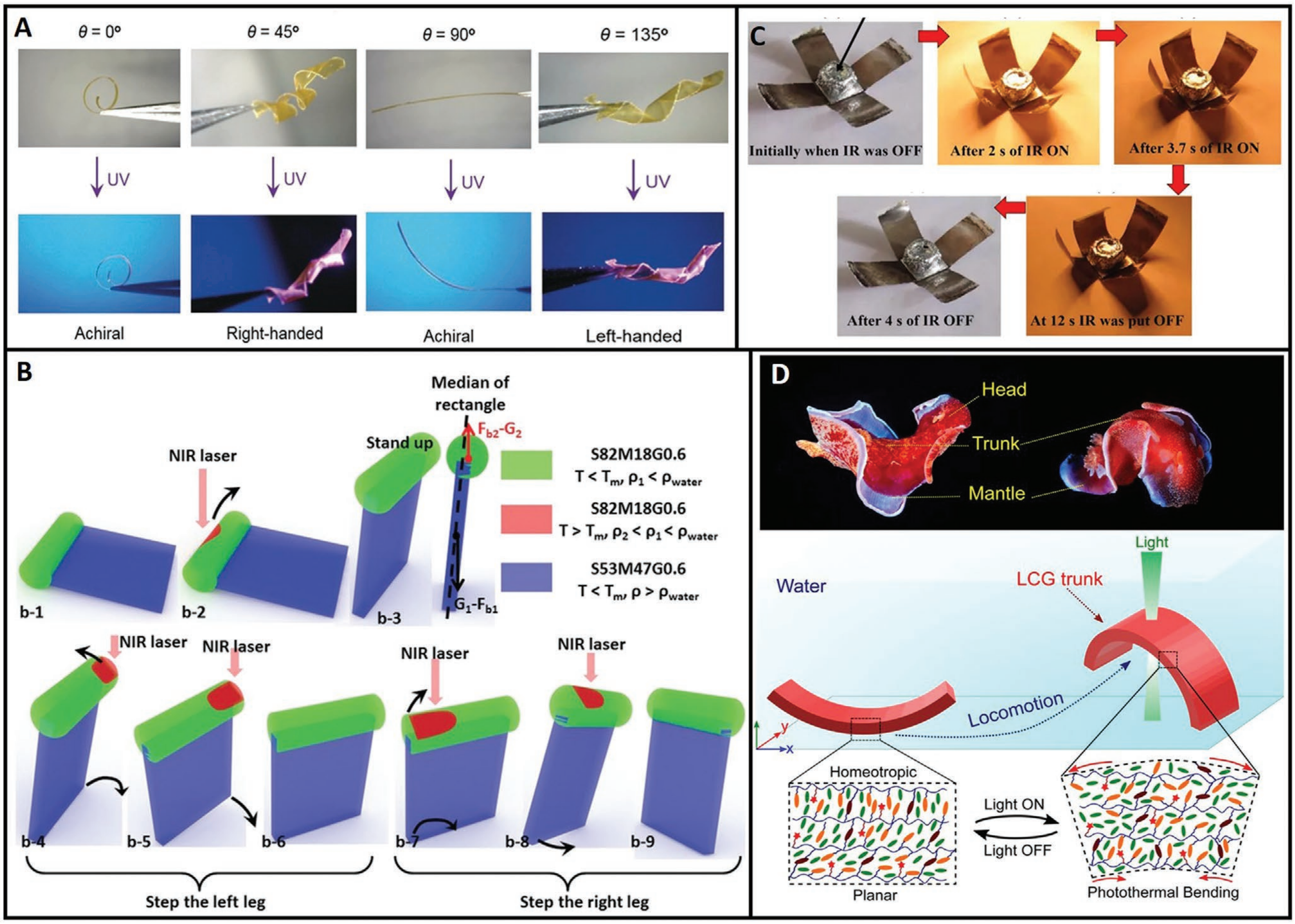

**Figure 12.** Photoresponsive actuators. A) LCP network with azobenzene units. Different actuation modes of ribbons with different cutting angles with respect to the molecules' orientation in the mid-plane. B) Schematic illustration of a hydrogel-based robot locomotion. C) Reversible actuation of a GO/polycarbonate bilayer structure. D) Swimming locomotion of a Spanish dancer (sea slug). Schematic illustration of the LCG actuator mimicking Spanish dancer locomotion. A) Reproduced with permission.[185] Copyright 2017, Wiley-VCH. B) Reproduced under the terms of the Creative Commons CC-BY license.[75] Copyright 2015, Wiley-VCH. C) Reproduced with permission.[186] Copyright 2018, Nature Publishing Group. D) Reproduced with permission.[187] Copyright 2020, National Academy of Sciences.

example is a gecko-inspired microstructured device that uses azobenzene and LCEs. The hierarchical structures found under gecko toes grant them the dry adhesion and thus, the ability to walk on various textured and sloped surfaces. A recent study developed a controlled adhesive mechanism composed of a PDMS mushroom-shaped microstructure with a photoresponsive LCE unit. Utilizing azobenzene switches enables UV light stimulation by disrupting the LC mesogen alignment through photoisomerization of azobenzene. These microstructures minimize their contact area under UV light illumination, which disables adhesion.[190]

### *3.4.2. Photothermal Effect*

The other method used for activating photoresponsive materials is through heat generation caused by light illumination. Photothermal actuators are typically made by introducing a photothermal heater into thermoresponsive polymer matrices. Carbon materials such as CNT, GO, and RGO are the popular photothermal heaters used in the development of recent bioinspired soft actuators. These materials can be used in hydrogels, LCEs and LCNs, and LCPs.[71,73,74,192]

RGO sheets absorb NIR and generate heat, making them a promising option (alongside thermoresponsive materials) to develop light-driven actuators. Wang et al. fabricated a hydrogel actuator by combining RGO sheets as a heat generator element and elastin-like polypeptides (ELPs) as a thermoresponsive element. They demonstrated local, finger-like flexing in the hydrogel at the location of NIR laser spot.[78] With a similar mechanism, Wang et al. made a light-driven swimming and walking actuator. These actuators are made by the copolymerization of stearyl acrylate (SA), methacrylic acid (MA), and RGO as NIR absorbent. By changing the temperature of the gel at the laser spot, the density of gel changes with respect to water. This results in different motions such as fish-inspired swimming and bipedal walking according to the geometry of the actuator (Figure 12B).[75] Thermal properties of graphene were used to mimic a caterpillar's locomotion. The robot is composed of a series of PDMS cuboids with every other cuboid containing graphene, enabling photoresponsive actuation. This robot responds to a range of wavelengths from UV to infrared.[193]

Bilayer structures have extensively been used in fabricating reversible photoresponsive actuators. Bilayer photothermal soft actuators employ layers with different thermal expansion coefficients causing thermal stresses at the interface. An inchworm-inspired soft robot composed of an RGO and GO-polydopamine bilayer soft film structure was actuated by a periodic NIR pulsed laser.[194] Figure 12C shows a GO/polycarbonate bilayer structure used as an actuator with fast and selective responses, low-cost fabrication, and large deformations.[186]

Recently, researchers have been investigating ways to increase the dexterity of photoresponsive actuators and multimodal locomotion robots. One group has successfully developed an LCE and CNT composed photoresponsive inchworm-inspired robot capable of crawling, jumping, and squeezing through channels.[195] Implementing GO for photo actuation has gone beyond single stimulus, as researchers have used them along with other active materials to develop multiresponsive actuators.[72,73,192] LCEs can be made photoresponsive through radiative heating via light exposure. A photothermal caterpillar robot was made by periodically applying light to a strip of LCE. A crawling motion was generated through activation and deactivation of the elastomer.[196,197] A gastropod-inspired robot was designed to locomote upon synthetic mucus by using a modulated laser beam to actuate a photoactive polymer in an undulating fashion. This snail-like robot can also locomote vertically while adhered to a wall, horizontally while adhered to a ceiling, and over obstacles.[198]

One of the benefits of using light as a stimulus is that noncontact actuation expands the applicability of designed methods to environments other than air. Inspired by benthic invertebrates, particularly members of the phylum Mollusca (e.g., sea slugs and snails), Shahsavan et al. showed that photoresponsive liquid crystal gels (LCGs) can also be utilized for underwater actuation. The actuation mechanism of these actuators is based on photothermal responses of the fabricated LC to the illumination of a 532 nm laser beam with different input powers (Figure 12D).[187]

Similar to the other bioinspired soft actuators, recently, researchers have been investing in new fabrication processes of photoresponsive actuators such as 3D printing. Yang et al. used shape memory polymers and carbon black to 3D print photoresponsive memory devices. Studying the effect of material thickness and light density, they showed that this fabrication method provides opportunities in bioinspired soft robotics.[199] A new concept in fabricating bioinspired soft actuators is 4D printing. This method is a combination of printing a 3D geometry with dynamic modulation. Nishiguchi et al. used this technique to print nanocomposite soft actuators composed of thermoresponsive PNIPAM and AuNRs, showing the viability of 4D printing for adaptive bioinspired actuators.[200]

Despite the benefits of photoresponsive bioinspired actuators, there is room for improvement in their efficiency and resolution. The number of factors contributing to the efficiency of these actuators has made it difficult to characterize it and requires further studies. The practical resolution in photothermal actuators is less than that of the stimuli. As the generated heat affects the neighboring molecules, the achievable actuation resolution is limited. This suggests the need for designing new photoactive materials to achieve better efficiency, wavelength selectivity, and higher resolution.[201]

### 3.5. Magnetic Responsive Actuators

Magnetic stimulation has unique advantages over other stimuli used for bioinspired soft actuation. These advantages include: 1) noncontact, remote control which can penetrate through a wide range of materials, 2) precise manipulation through controlling the direction and strength of the magnetic field, 3) enhanced controllability enabled by independently changing the magnetic field and gradients, 4) the capability of generating high-frequency AC fields for applications such as magnetic hyperthermia, 5) scalability and controllability of actuators across length-scales from nanoscale to macroscale. Their drawback is that they require a complicated and bulky external apparatus to control the magnetic field and its gradients precisely. Another shortcoming is that as the distance from the source increases, the magnetic field strength drops significantly.

Nanocomposites are widely used to develop soft actuators since they can combine the properties of fillers and matrices to achieve desired functionalities. One of the mechanisms adopted for the actuation of soft materials is to introduce magnetic responsive materials as fillers in a soft polymeric matrix.[202–205] The resulting materials are a class of shape morphing materials used in soft bioinspired actuators.[206] The actuation mechanism for these materials can either be directly through the applied forces and torques on the filler or through indirect actuation of a thermoresponsive matrix (e.g., using heat generation with high-frequency AC magnetic fields).[204] The fillers can be either small-scale particles made to form continuous responsive areas or magnetized bodies to create discrete active domains.

Strategies for achieving desired functionalities go beyond the material selection of fillers and matrix. Researchers are actively working on various designs to gain new functionalities. For example, different filler distributions can be used, such as a uniform distribution in the bulk of the matrix[207–209] or a concentrated distribution in a specific area.[210] Moreover, new functionalities can be achieved by innovative design, such as using magnetically active and inactive sections of the actuator,[211] nonuniform magnetization profiles,[212] or their combination (**Figure 13**B).[213]

### 3.5.1. Nonmagnetized Bodies

Magnetic responsive soft actuators exhibit great potential over a nano- to macroscale range. Successful examples of these actuators at the microscale are demonstrated in magnetic micropillars and microrods, inspired by cilia and gecko toe hairs. These actuators exhibit potential in applications such as locomotion, propulsion, and controlled surface wettability and adhesion.[217] Researchers use the distribution of particles as a tool to manipulate the functionality of microrods for desired applications. Different particle distributions have been studied, including linearly aligned along the rods, concentrated at the tip of the rods, and random distributions. It was shown that the aligned distribution dramatically enhances responses to applied magnetic fields.[208] Jiang et al. demonstrate a device inspired by cilia, including a magnetic responsive array of soft microrods. These arrays were fabricated by mixing magnetic cobalt (Co) nanoparticles with a PDMS matrix. By changing the external magnetic field, they were able to tune the posture of microrods.[210]

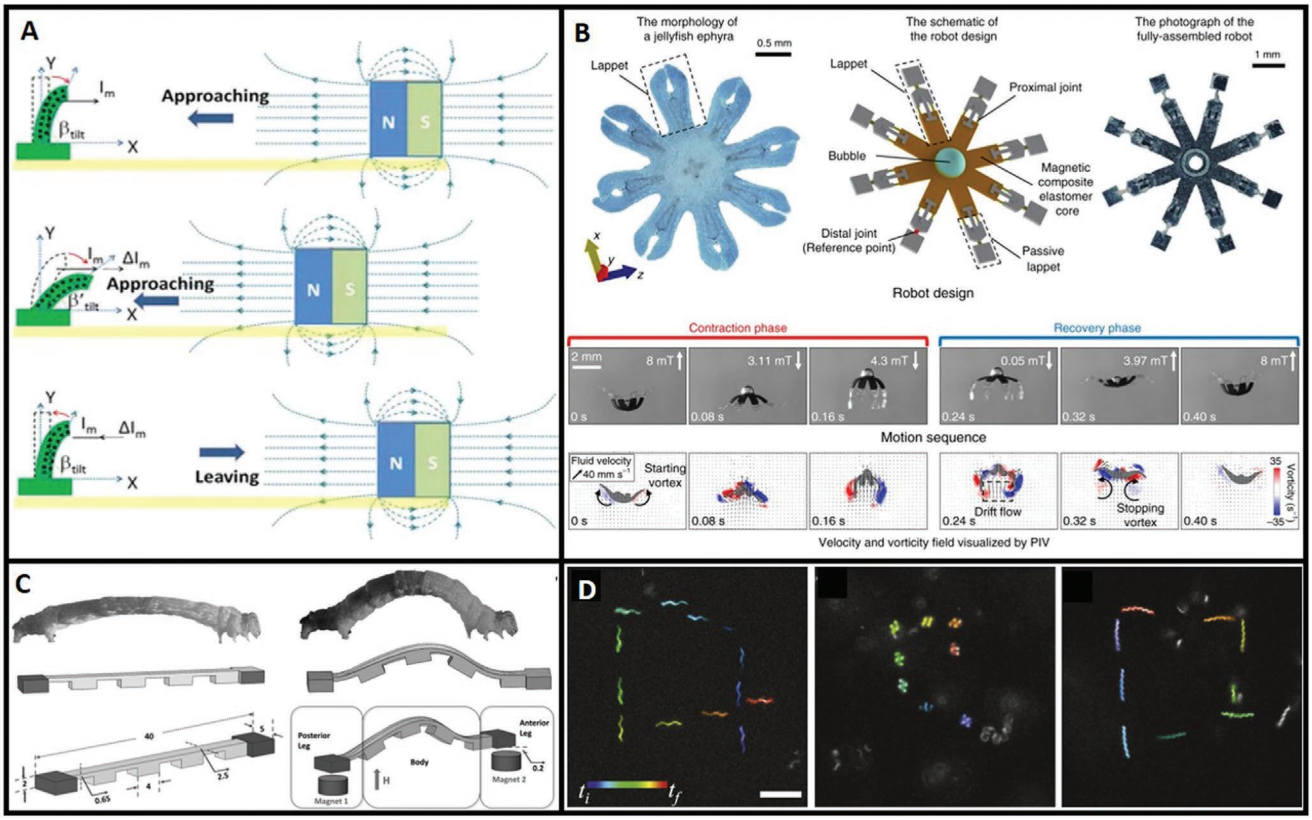

**Figure 13.** Magnetic responsive actuators. A) Actuation of microrods using an external magnetic field. The microrods' tilt angles ($\beta_{\text{tilt}}$) are affected by both the magnetic field intensity ($I_m$) and changes in the intensity ($\Delta I_m$). B) The design of a jellyfish-inspired soft robot, its swimming motion sequence, and the velocity and vorticity fields visualization. C) An inchworm-inspired soft robot. D) Flagellar nanorobots. Left to right: helical, coiled, and curly swimmers (Scale bar indicates 5µm). A) Reproduced with permission.[214] Copyright 2015, Nature Publishing Group. B) Reproduced with permission.[213] Copyright 2019, Nature Publishing Group. C) Reproduced with permission.[215] Copyright 2019, Mary Ann Liebert. D) Reproduced with permission.[216] Copyright 2017, Nature Publishing Group.

Besides the microrods, distributed magnetic nanoparticles can be used in other microstructures such as microplates. Inspired by chameleons, Jiang et al. demonstrated that microplate actuators can be used for color conversion. Moreover, they employed microplates to switch between a hydrophilic and hydrophobic surface.[218] Inspired by controlled surface wettability found in nature (e.g., lotus leaf, Indian cress leaf, lady's mantle leaf, gecko feet, and butterfly wing), Wang et al. used magnetically responsive microplates for liquid transport, self-cleaning, and water-repelling (Figure 13A).[214]

Besides employing these microstructures for developing functional surfaces, they can also be used for untethered locomotion. A millipede-inspired soft robot equipped with micro-tapered magnetic legs was developed for drug delivery. The magnetic legs were composed of PDMS, hexane, and magnetic particles. The legs enabled the robot to function on different terrains in both dry and wet environments and even in unstructured terrain such as a model stomach.[219]

Actuation of magnetic particles is not limited to solid materials, as Leon-Rodriguez et al. showed that magnetic responsive liquids can mimic the locomotion of the unicellular organism, Amoeba.[220] This magnetic responsive liquid, known as ferrofluid, is made of ferromagnetic particles with diameters between 5 and 20 nm suspended in carrier liquids.[221] The high flexibility of these actuators in response to magnetic fields has brought about interesting bioinspired applications. For example, they have been used in molding processes to replicate remarkable structures found in nature. Using ferrofluid based molding, researchers were able to produce a clamping microneedle array inspired by the serrated acicular structure of the forelegs of mantises.[222] In addition, using this process, surfaces with anisotropic wettability are developed, inspired by natural *Nepenthes* peristome.[223]

#### *3.5.2. Magnetized Bodies*

One of the advantages of magnetic actuators is their scalability. Many of the macroscale magnetic responsive actuators employ discrete magnetized bodies or nonuniform magnetization profiles along the body. By embedding discrete magnetized bodies in soft mediums, it is possible to create actuators with active and passive domains. Joyee et al. developed an inchworm-inspired robot using magnetic responsive material in the posterior and anterior segments of a flexible polymeric body (Figure 13C).[215] Using the same configuration but with different magnetization directions, Pham et al. developed a soft medical robot to generate undulatory locomotion inside the lumens of the body. This robot uses two permanent magnets embedded at both ends of a silicon rubber elongated body and is actuated by a rotating nonuniform magnetic field.[224] Other soft robots, like those inspired by Venus flytrap, take advantage of magnetically active and inactive segments to enable a snap-through functionality.[225,226]

In a more comprehensive design, the direction of magnetization follows a profile along the actuator's body. Through the design of the profile, researchers can program different functionalities that can be selectively activated by controlling the magnetic field. Using this method, Hu et al. developed a millimeter-scale soft robot inspired by beetle larva and inchworm. By controlling the magnetic field, this robot can switch between different locomotion modes such as rolling, walking, jumping, and swimming.[227] In another study, researchers fabricated robots that mimic different modes of terrestrial motion inspired by inchworms, millipedes, turtles, and other quadrupeds. These robots usually use magnetic responsive limbs attached to a magnetically inert soft body.[228] Expanding this technique to 3D magnetization profiles over different geometries of soft actuators can enable multiaxis bends, sharp bends, and combinations of torsion and bending, mimicking complex modes of bioinspired locomotion.[229] For instance, using directionally magnetized actuators, Dai et al. fabricated a cephalopod-inspired robot out of neodymium magnet (NdFeB) powder mixed with Ecoflex 00-10. They used a triangular wave gradient magnetic field for higher stability and controllability.[230] Researchers are also investigating different printing methods to facilitate the fabrication of soft bodies with different magnetized domains and complex heterogeneous structures.[231,232]

The actuation of magnetized bodies is not limited to macroscale. There are examples of premagnetized nano- and microscale actuators used for locomotion purposes, such as magnetic microswimmers. They have been inspired by bacteria,[233] sperm cells,[234] and other unicellular eukaryotes[235] (Figure 13D). The capability of remote propulsion and guidance using magnetic fields offers great benefits toward in vivo biomedical applications such as drug delivery, biopsy, and microsurgery.[216,236–238]

### 3.6. Electrically Responsive Actuators

Electrically driven actuators have the advantages of operational simplicity and exceptional controllability. This class of soft actuators can either directly convert electrical energy to mechanical energy or actuate thermoresponsive materials through Joule heating. Electric motors have been used exhaustively in conventional robots, offering precise control, robustness, and excellent repeatability.[243–245] Such motors are composed of rigid parts and thus are not used in bioinspired soft robots, yet electrically powered components are highly standardized and preferred. Therefore, researchers have introduced a new generation of electrically responsive actuators that are suitable for use in soft robotics: artificial muscles (**Figure 14**A).[239] Among these artificial muscles, EAPs best mimic biological muscles as they exhibit changes in shape or size through ion-infusion and electric field actuation.[246] In particular, DEs, LCs, and IMPCs are widely used in bioinspired soft robots.

#### *3.6.1. Coulombic Attraction of Electrodes*

Among EAPs, DEs have received more attention due to their unique properties such as large strains, high energy densities, rapid response rates, light weights, and low costs.[247] A dielectric actuator (DEA) is composed of a soft elastomer membrane sandwiched between two compliant electrodes. By applying a voltage to the electrodes, the DEAs experience Coulomb forces, an attractive force that deforms the elastomer membrane. The conventional method of fabricating DEA is to stack multiple

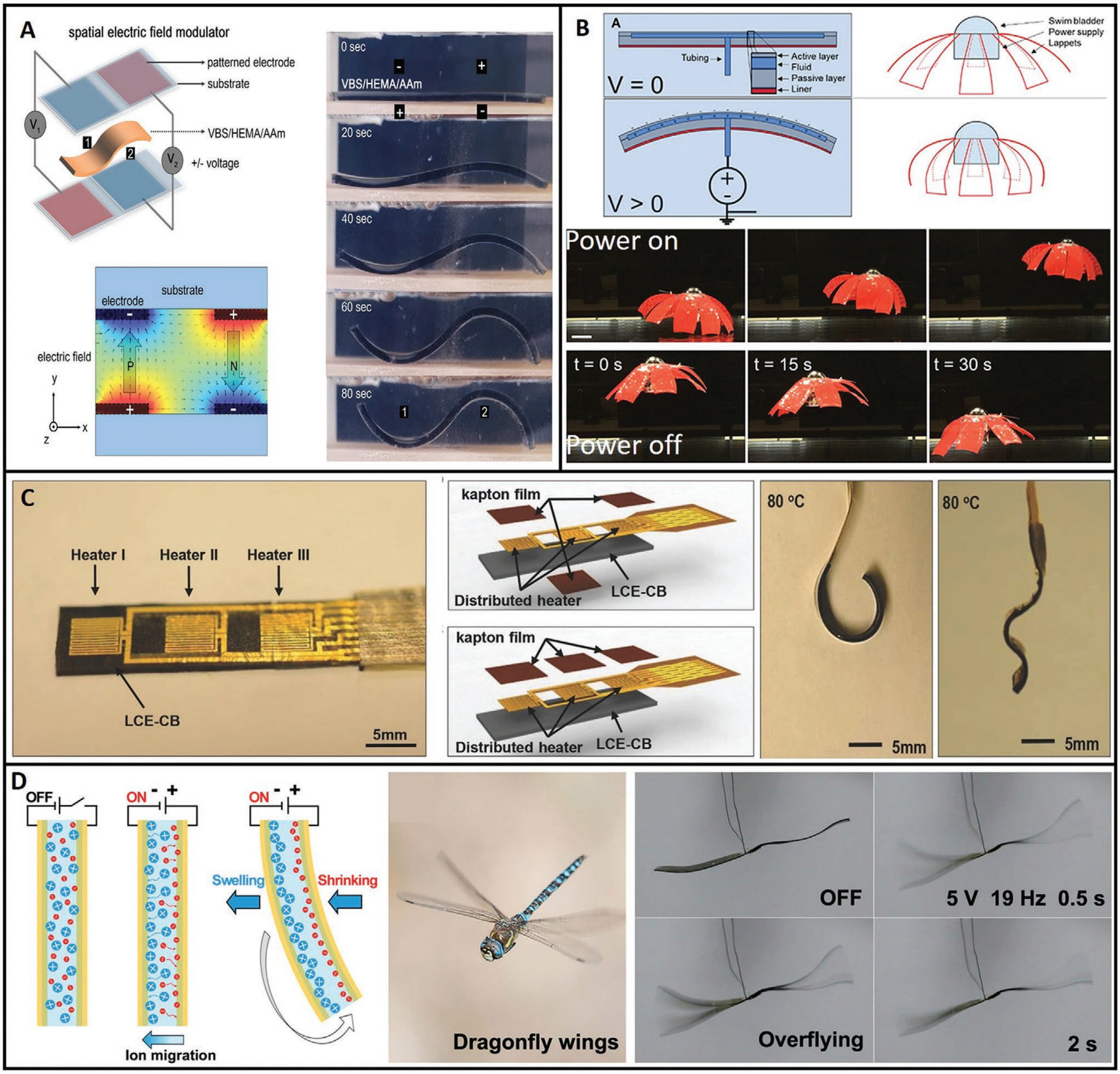

**Figure 14.** Electrically responsive actuators. A) Schematics of an electroactive hydrogel actuator bending in response to the applied electric field and an image sequence of the actuated hydrogel. The actuator reaches its final shape in 80 s. B) Working principle and swimming image sequence of a Jellyfish-inspired robot made of dielectric elastomer actuators. C) LCE-CB actuator with three heaters (left). The impact of Kapton film on the deformation of the actuator (center and right). D) Schematic of an IPMC actuator. High-frequency wing-flapping inspired by the dragonfly. A) Reproduced with permission.[239] Copyright 2020, Nature Publishing Group. B) Reproduced with permission.[240] Copyright 2019, Frontiers. C) Reproduced with permission.[241] Copyright 2018, Wiley-VCH. D) Reproduced with permission.[242] Copyright 2020, Wiley-VCH.

layers of DEs in a single actuator.[248] More recently, different fabrication methods have been introduced to the field. Haghiashtiani et al. employed a direct ink writing (DIW) technique for printing DEAs.[249] Cobaci et al. made use of advances in microfabrication techniques to develop an actuator made of microscale DEA units to resemble myofibrils in biological muscles.[250] The single body DEA (SDEA) has also been introduced to remove the necessity of an external frame, which leads to lighter and more flexible DEAs for artificial muscle applications.[251]

Moreover, better modeling and control of DEAs are also actively pursued as the nonlinear behavior of DEAs creates challenges in precise control. For instance, researchers developed a physics-based nonlinear model and used it to design control strategies for a two degree of freedom DEA.[252] In another study, Gu et al. proposed a model for the viscoelastic electromechanical behavior of DEAs using dissipative nonequilibrium mechanisms. They demonstrated the effectiveness of their model using both experiments and simulations.[253] Furthermore, optimization of DEAs and improvements of their efficiency have also been explored recently.[254,255]

DEAs have been used as artificial muscles in numerous bioinspired soft robots.[256] Li et al. used these actuators to generate eyeball motions in humanoid robots. These actuators provided low noise and natural appearance. Inspired by the extraocular muscles in the human eye, they used three linear DEAs to achieve human eye like motion.[257] There are also examples of utilizing DEAs in plant-inspired soft robots. For instance, Xu et al. developed a gripper inspired by a Venus flytrap with an actuation time of 0.25 s.[258] Furthermore, DEAs have helped researchers mimic insect locomotion.[259,260] A bioinspired hexapod robot has used an alternating tripod gate to walk over flat surfaces. A 7 Hz actuation frequency leads to a speed of 52 mm $s^{-1}$ (approximately 0.35 body lengths per s).[261,262] In another study inspired by insect's resonant actuation, an optimization analysis took place on a double cone-shaped DEA (DCDEA) structure. This study resulted in a peak flapping stroke of 31° at its resonance of 30 Hz.[254] Crawling is another type of locomotion that DEAs have been able to achieve.[263–266] A bioinspired annelid robot was developed with several DEAs, forming a multisegment structure. Deformation of the DEAs makes it possible to mimic axial elongation of annelid body segments.[258]

There have also been bioinspired swimming robots that use DEAs.[193,267] The swimming of aquatic creatures is a great source of inspiration to replace noisy and power-consuming propellers and thrusters. A frog-inspired swimming robot was designed with limbs composed of two segments, mimicking a frog's leg and foot. Each segment is actuated independently using a DEA.[268] Inspired by leptocephalus, Christianson et al. investigated the possibility of using surrounding environmental fluid as an electrode to actuate a DEA. This resulted in a frameless and submersible DEA.[269] Jellyfishes (Figure 14B),[240,270] manta rays,[271], fish fins[272], and other aquatic animals[273,274] have been sources of inspiration for developing untethered swimming robots using DEAs. Inspiration from aquatic animals is not limited to modes of locomotion, as Sholl et al. developed a soft end-effector inspired by cephalopod suckers.[275]

The applications of DEAs in bioinspired soft robotics are not limited to aforementioned examples, as there are many bioinspired grippers, insect-inspired robots, and other soft robotic systems that have been introduced to the field.[276–278]

### 3.6.2. Joule Heating

LC-based bioinspired soft actuators are popular, for they can be actuated with many different stimuli. Researchers control these actuators either directly or indirectly. Although their main mechanism of actuation is by direct heating, researchers have found it favorable to use other stimuli such as indirect heat generation. Among these different indirect methods, electrical stimuli that enables Joule heating are more convenient and provide better control, when compared to other actuation modes.[279] Wang et al. developed a LCE-based electrically responsive actuator to mimic the behavior of soft animals such as the inchworm. They achieved faster response times by doping carbon black (CB) nanoparticles into the elastomer, increasing its thermal conductivity. (Figure 14C).[241] Furthermore, this mechanism has been used to create gecko-inspired temperature-switchable adhesion,[280] and to actuate an artificial iris inspired by that of the human eye.[281]

Deriving inspiration from elephant trunks, octopus arms, and starfish feet, researchers have developed soft manipulators with high dexterity using LCE-based actuators.[282] He et al. fabricated a multimode tubular actuator that works based on Joule heating of LCEs. By embedding heating wires in different sections of the LCE tube, bending and contractions were achieved.[283] Although these actuators offer high dexterity and large deformations, the coupling of heating elements and soft bodies makes their dynamic modeling difficult.[284]

Inspired by the architecture of natural soft tissue, researchers fabricated soft actuators composed of LCE and liquid metal (LCE-LM). LM microparticles embedded in the LC matrix provide thermal and electrical conductivity and enable self-healing.[285] Ford et al. studied the effect of LM particles on the actuator's properties. They showed by changing the size of LM droplets, they can tune properties such as achievable output force and stroke length.[286] Kent et al. used LM in a fluidic channel to fabricate LCE-LM soft actuators. They showed that alongside their actuation capabilities, these channels could also be used as sensors enabling closed-loop control.[287]

### 3.6.3. Redistribution of Ions

Another class of EAPs are IPMC actuators that undergo deformation in response to an external electrical stimulus.[288] In recent years, IPMCs have been utilized to emulate the muscles of an elephant trunk.[289] Additionally, researchers found IPMCs to be useful for underwater applications and have used them successfully as a tail actuator for steering a robotic fish.[290,291] Fast response rates of IPMCs make them a suitable choice for high-frequency applications. Using this property, Ma et al. fabricated a high-frequency wing-flapping robot inspired by dragonflies. They were able to achieve a frequency of over 10 Hz using their IPMC actuators (Figure 14D).[242]

Despite the benefits of IPMC actuators such as being lightweight, flexible, and capable of exhibiting large bending with low voltage inputs, their applications are restricted due to several limitations. One of the limitations is the instability due to the relaxation effect in IPMCs in which, after actuation, the IPMC undergoes an undesired reversed deformation toward its initial state. Generating low output forces is another drawback.[292] Furthermore, solvent evaporation and lack of an optimized and standardized fabrication method are among other notable limitations.[106,107]

## 3.7. Multistimuli Responsive Actuators

While the efforts and achievements with individual stimuli are thriving, researchers have also tried to integrate the advantages of different actuators into one as a means of achieving multifunctionality and versatility. These approaches have received extensive efforts to develop multiresponsive bioinspired soft actuators. One approach is to use a single multiresponsive layer of material, the other to fabricate a composite structure composed of layers of single-stimuli materials.

### *3.7.1. Multilayer Structures*

One approach of fabricating multiresponsive actuators is to use multilayered structures composed of single-stimuli layers. Considering the vast use of polymers in single stimulation actuators, polymers are commonly chosen as the active layers. Furthermore, in situations where the active layer is too soft to generate a practical actuation response, adding an inactive, stiff layer such as PDMS can solve the problem. Using PDMS as the stiff layer, Li et al. reported a temperature and pH-responsive hydrogel-based bilayer actuator. They achieved bending actuation in a PNIPAM-based semi-interpenetrating network (semi-IPN) bilayer structure in response to the variation in the environment's temperature. They also investigated the effect of copolymerizing AAc into hydrogel layer to make it pH-responsive.[170] Another example of using PDMS for the passive layer in conjunction with polymers for the multiresponsive layer has been introduced by Toccola et al. They used PEDOT:PSS as an active layer to develop an electric- and humidity-driven actuator (**Figure 15**C).[294] The layer used for additional stiffness is not necessarily inactive. Cunha et al. showed that adding magnetic carbonyl iron powder to the PDMS provides functionality in response to magnetic stimulus. The second layer of this actuator was inspired by the chameleon's feet and is made of LCN containing photochromic azobenzene dyes, which are triggered by light stimulation (Figure 15A,B).[293]

Paper can also act as either a passive or active layer while providing additional stiffness. It is also low-cost, lightweight, flexible, and biodegradable. Inspired by the ciliary muscle of the human eye, a paper-based multiresponse bilayer actuator is reported by Hu et al., which achieved various deformations such as bending, elongation, and folding. In addition, it had reversible color-changing properties with voltage, temperature, and light stimuli. They used paper with an anisotropic cellulose microfibrils structure, polymer, and silver nanoparticles as geometry constraints, deformation active layer, and energy conversion element, respectively. In addition to deformation, the color-changing function is studied

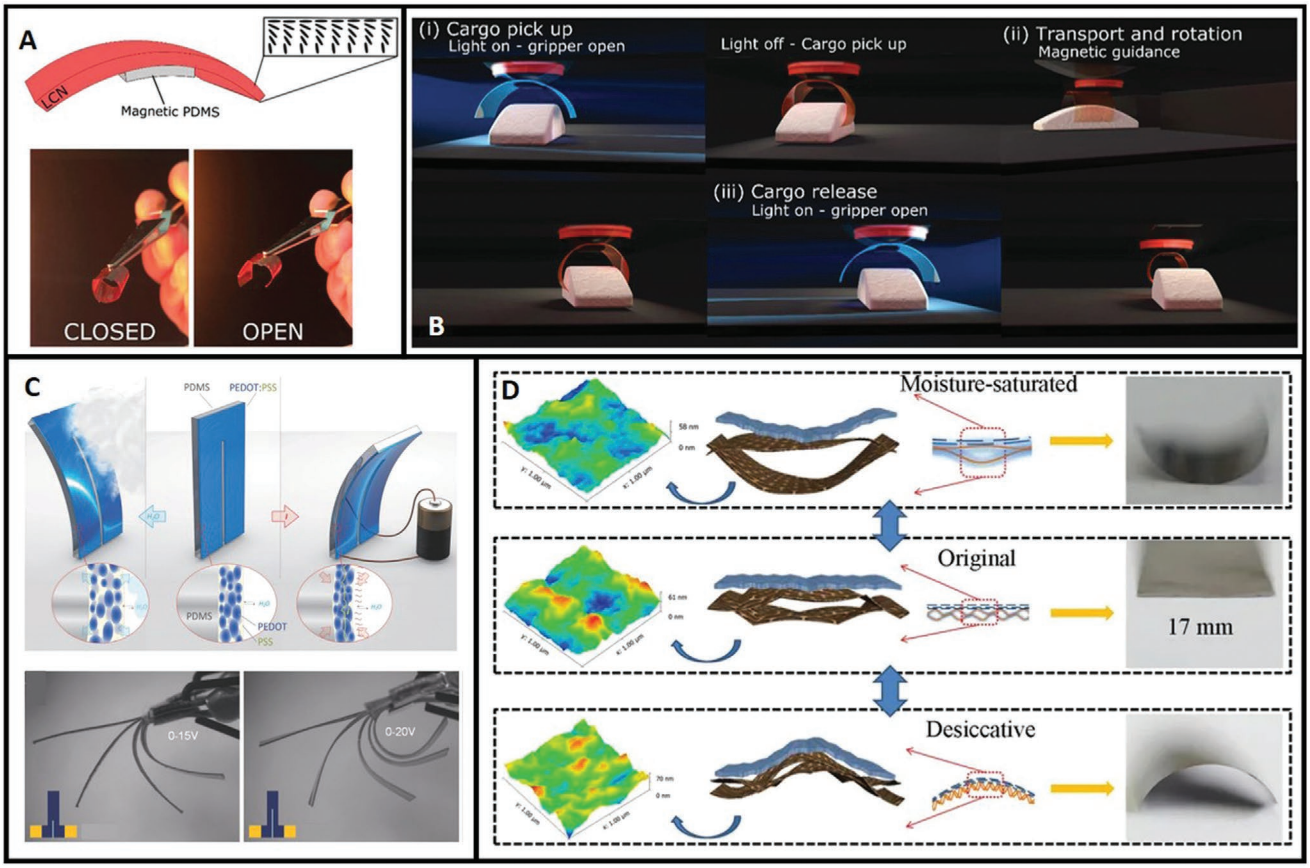

**Figure 15.** Multistimuli responsive actuators. A) A magneto and photoresponsive actuator. B) Illustration of using the actuator in (A) for a pick and place task. C) A moisture and electrically responsive actuator and an image sequence of its actuation. D) A moisture, heat, and photoresponsive actuator. The actuation of a GO(brown)/RGO(blue) structure due to water absorption and desorption is illustrated schematically. A,B) Reproduced with permission.[293] Copyright 2019, Wiley-VCH. C) Reproduced with permission.[294] Copyright 2015, Wiley-VCH. D) Reproduced with permission.[295] Copyright 2015, Nature Publishing Group.

by utilizing the thermochromic pigments in the polymer layer.[296]

The other popular layer used in the multilayer structures is allotropes of carbon (Figure 15D). An example of such actuators is reported by Hu et al., inspired by human finger flick behavior and blooming flowers' response to electrical stimulation and sunlight. This bilayer actuator is composed of rolled CNT and polymer. The actuation mechanism relies on electrothermal and photothermal properties of CNT, along with the thermal expansion between the two layers.[297] The electroheating property of carbon allotropes has promoted their use with different polymers. Duigou et al. used polyamide (PA6) and continuous carbon fibers (cCF) during a 4D printing process to build a bilayer actuator. Polyamide is a well-known moisture responsive polymer. The secondary actuation mechanism was electroheating to change the moisture content of the wet sample.[298] Yang et al. utilized PI adhesive tape and spongy graphene to develop a bilayer actuator with dual-stimuli responses. This functionality is due to the electrothermal and photothermal properties of graphene, deformation of graphene micro-gasbags, and thermal expansion of PI. This actuator can generate large bending curvatures and forces under electrical and light stimulation. The actuator can lift more than 20 times its weight, only limited by the thickness of the material, and was successfully used in a gripper, a robotic hand with independent finger actuation, and a crawling robot.[299]

Another property of graphene is its sensitivity to the change in humidity. Mimicking hawk claw and tendril climber plants, Dong et al. developed a multiresponsive bilayer actuator. This programmable GO/polypyrrole (PPy) bilayer actuator was fabricated using a hydrogel microstamping technique as a means of patterning on a GO film. A humidity responsive actuator was accomplished by coupling a PPy layer (acting as the passive hydrophobic material) with a GO layer (acting as a humidity sensitive material). Moreover, temperature and infrared light can also affect the water absorption of the GO layer.[300]

Multilayered multistimuli actuators are not limited to two layers. Deng et al. fabricated an actuator made from three layers consisting of poly(vinylidene fluoride) (PVDF), PI polymers, and laser-induced graphene (LIG) structures. This actuator inspired by plants and cellulose fibrils, can achieve programmable shape morphing. LIG structures act as the geometrical constraints in the polymer, which dictate the shape morphing actuator's behavior. Moreover, LIG converts photo and electrical energy into thermal energy. PVDF, the active layer of this actuator, enables photothermal, electrothermal, vapor, and moisture stimulation. The material is constrained to bend along the graphene alignment, which can be tailored to accommodate desired complex shapes. This actuator is used for crawling and gripping, where the gripper is able to hold more than 20 times its weight.[301]

#### *3.7.2. Single Layer Structures*

Layered structures have their downside as they may suffer from delamination, which decreases their lifetime. Therefore, some researchers prefer to directly engineer a single layer to achieve desired functionalities.[302] Inspired by the phototropic growth of a seedling and the humidity-responsive blooming of morning glory flowers, Liu et al. introduced a humidity and UV photoresponsive actuator. Using azobenzene switches, this polymer film responds to UV light irradiation while the hydration of C=O and C−O−C groups in the LCs causes bending in the presence of a humidity gradient.[303] Wang et al. introduced an actuator with self-healing capabilities that is responsive to light and magnetic stimuli. Ferric oxide nanoparticles ($Fe_3O_4$ NPs) were used for their magnetic and photothermal properties. Moreover, $Fe_3O_4$@CNC enables response to NIR light and magnetic field.[304,305]

## 4. Bioinspired Sensors

Actuation without sensing is deficient, and in fact, there is no feedback control without sensing. Due to the high deformation of soft structures, preexisting sensors used on rigid bodies are not readily transferable to soft bodies. Either the sensor would limit the structure's deformation or the structure's deformation would compromise or damage the sensor. Solutions to such problems can be sought by reflecting upon the mechanisms found in nature. Plants, insects, animals, and humans are comprised of numerous types of receptors, which can inspire the design and development of sensors for soft robotic systems. The sections below cover several biological receptors (i.e., photoreceptors, chemoreceptors, and mechanoreceptors), and recent achievements made by scientists toward the development of bioinspired soft sensors (**Figure 16**).

### 4.1. Photoreceptors

Photoreceptors have been inspired by everything from the human eye to the arthropod compound eye. The arthropod compound eye is composed of hundreds to thousands of closely packed optical units called ommatidium, forming hemispherical facets. Over the years, many have taken inspiration from their architectural construct and have developed artificial compound eye structures.[317–319] The compound eye has the advantage of having a low aberration, due to the small aperture diameter and focal length of each ommatidium. This fixed focal length, however, can be disadvantageous for applications that desire depth discrimination. To obtain a continuously tunable focal length, some have taken inspiration from the contraction of the human crystalline eye lens and integrated it in their artificial compound eye design.[320] Ma et al. used the femtosecond laser wet etching (FLWE) technique to fabricate a microlens array structure based on bovine serum album (BSA) protein and placed it upon a SU-8 optical lens. The BSA protein microlens swells and condenses upon the increase and decrease of the pH value, respectively. The swelling causes the focal length to change, thus varying the field of view from 30° to 80°.[320]

The human crystalline lens is composed of transparent collagen and fibers, forming a closed elastic structure. The crystalline lens is connected by zonular fibers to the ciliary body. Ciliary muscles, in their relaxed state, cause tension of zonular

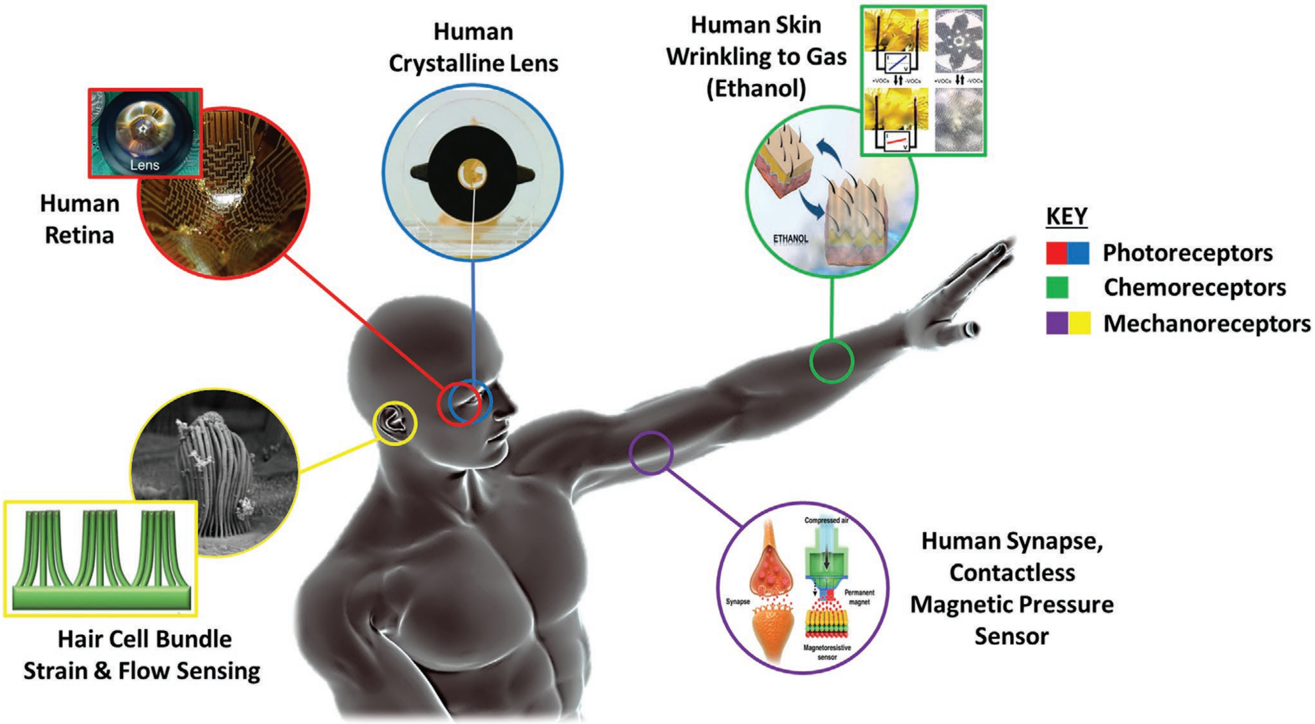

**Figure 16.** Bioinspired soft sensors. Representatives of some of the main bioinspired photoreceptors (i.e., human crystalline lens and retina), chemoreceptors (i.e., human skin wrinkling in the presence of ethanol vapor), and mechanoreceptors (i.e., magnetic pressure sensor inspired by human synapse system and strain and flow sensors inspired by the inner hair cell bundles). Human retina: Reproduced with permission.[311] Copyright 2017, Nature Publishing Group. Human crystalline lens: Reproduced with permission.[312] Copyright 2015, Wiley-VCH. Human skin wrinkling: Reproduced with permission.[313] Copyright 2019, Wiley-VCH. Human Synapse: Reproduced with permission.[314] Copyright 2017, Nature Publishing Group. Hair cell bundle, strain: Reproduced with permission.[315] Copyright 2019, Nature Publishing Group. Hair cell bundle, flow: Reproduced with permission.[316] Copyright 2012, Wiley-VCH. 3D male based image is designed by Kjpargeter/Freepik.

fibers. Tensed zonular fibers pull the crystalline lens into an oblate spheroid, allowing for distant vision. For near vision, ciliary muscles contract, allowing the zonular fibers to relax and the crystalline lens to retain a more spherical shape. The preceding is referred to as an unaccommodated lens (relaxed state), while the latter is referred to as an accommodated lens. Through accommodating the lens, the eye can focus on objects at different distances.[321,322]

The human eye's focusing mechanism and optical structure has motivated the design and development of various artificial tunable (liquid encapsulated) lenses.[318,323] Liquid is encapsulated by a polymer membrane to form a deformable oblate, spherical, or hemispherical lens. Liquid mediums provide a lighter alternative with higher optical transmittance than the conventional optical glass lens. Liquid selection is contingent upon its optical and mechanical properties, such that it has a high refraction index, low scattering, good material durability and thermal stability. This includes liquids such as water,[324] silicone oil,[325] glycerol,[326] polymethyl methacrylate (PMMA),[327] and PDMS prepolymer.[312] The polymer membrane's elasticity and transparency is also of great importance, thus capsule material has been made of poly(ethylene terephthalate) (PET),[325] PDMS,[324,327] and other silicone rubbers.[312,326,327] The polymer membrane is actuated by tension/compression mechanisms through the usage of a micrometer linear stage,[327] electromagnetic[324] (**Figure 17**A), DEA[312,326] (Figure 17B), and even electrowetting on dielectric (EWOD).[325] Through polymer membrane actuation, the liquid lens is deformed, altering its focal length.

The change in the focal point is usually captured by an image sensor, such as a complementary metal-oxide semiconductor (CMOS) or charge-coupled device (CCD), which converts the captured light into electrical signals. In the human eye, the light collected through the lens is converted into action potentials (i.e., electrochemical signals) by the retina.[322] Due to technological and fabrication limitations, previous retina image sensors were thick with large cross-sectional areas, inflexible, and bioincompatible. Furthermore, their implantation would cause retina and optic nerve damage.[318,323] Recent designs are semiconductor nanomembrane-based, which are soft, flexible, ultra-thin, and biocompatible. Initially, they are fabricated on a planar surface with intricate geometrical designs that avoid overlap when deformed into a hemispherical shape. These curved image sensors (CurvIS) have shown to have low aberrations and a wide field of view (Figure 17C,D).[311,328] Choi et al. have performed in vivo animal experiments by implanting their CurvIS upon the retina of rats, where optic nerves were observed to respond to the exposure of white light-emitting diode (LED).[328] This provides hope for patients who have lost their vision due to retinal degeneration. A summary of the above-mentioned designs, along with additional metrics, can be found in **Table 2**.

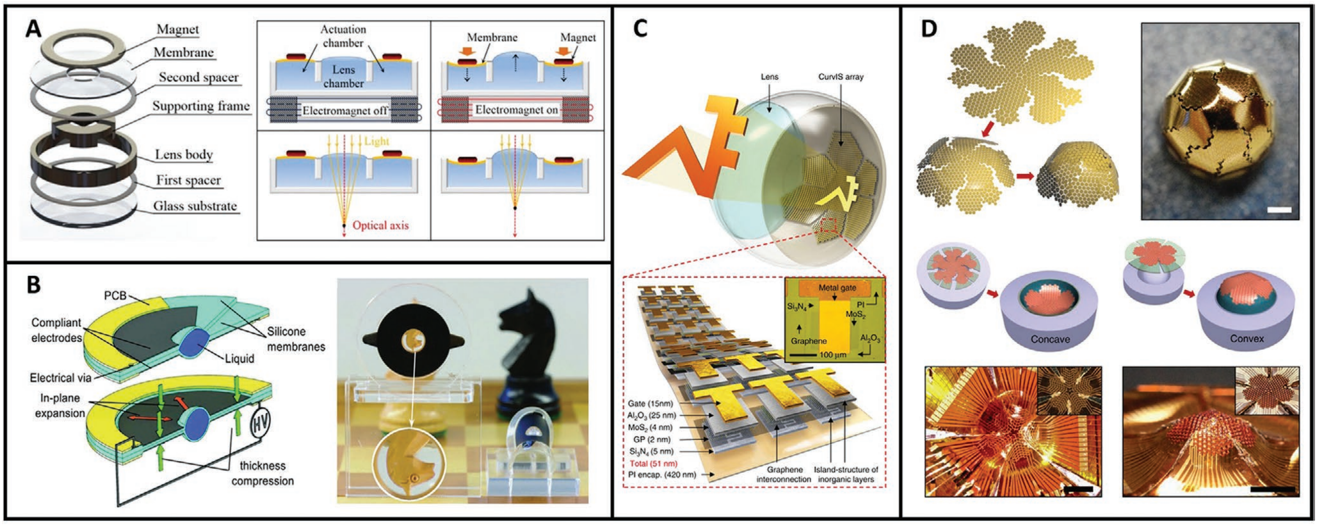

**Figure 17.** Photoreceptors inspired by the human eye. A) Tuning of liquid crystalline lens through the actuation of the electromagnetic field, causing the permanent magnet to descend, compressing PDMS encapsulating water membrane. With volume conserved, the membrane's center deforms convexly, changing the focal point. This mechanism has an actuation and relaxation time of 900 ms. B) PDMS encapsulating silicone prepolymer spherical liquid lens is actuated through DEA. 20% change in focal length change is achieved within 175µs. No degradation observed after 400 × $10^3$ cycles. C,D) Soft and biocompatible semiconductor nanomembrane photoreceptors. Fabricated in 2D with intricate geometrical designs and deformed concave to replace degraded retina. D) The photoreceptor has the ability to be deformed convexly to be used as a compound eye. A) Reproduced with permission.[324] Copyright 2016, Elsevier. B) Reproduced with permission.[312] Copyright 2015, Wiley-VCH. C) Reproduced with permission.[328] Copyright 2017, Nature Publishing Group. D) Reproduced with permission.[311] Copyright 2017, Nature Publishing Group.

### 4.2. Chemoreceptors

#### 4.2.1. Gas

Monitoring gas and vapor is of great importance for the well-being of humans and life on the planet. For example, humans' water metabolism can be captured through breathing and used as a means of measuring vital physiological conditions.[329–332] In addition, hazards and death caused by gas leaks (lacking odor, taste, or color) can be prevented,[333,334] and carbon dioxide emission could be supervised in hopes of decreasing its effects on climate change.[335] With the advancements of technology, developed sensors can accurately and selectively quantify humidity,[336–339] volatile organic compounds (i.e., ethanol, acetone, methanol, formaldehyde),[313,336,338] and noncondensable gases (i.e., hydrogen, carbon monoxide, carbon dioxide).[340]

Humidity sensors have been inspired by weak molecular interactions and bonds[336,337] to the photonic structures of beetle wing-cases.[338,339] Weak noncovalent interactions between proteins and molecules lead to supramolecular assemblies and disassemblies, which can be detected at a cellular level.[341,342] With the presence of water molecules and weak noncovalent interactions, hydrogen bonds rapidly form and break (at room temperature) due to their intermediate intramolecular force.[343,344] By taking advantage of this interaction, humidity can be measured through the collection of water molecules at low and high relative humidity. He et al. used an alternating graphene polymer composite (i.e., graphene nanochannels confined polydopamine) as the sensing material,[336] while Wang et al. used a composite consisting of graphene, carbon nanotubes, and cellulose nanocrystals.[337] These sensors measure water metabolism of humans[336] (**Figure 18**A) and environmental conditions[337] with high sensitivity for low to high relative humidity. With a constant voltage, the sensor circuit measures the change in resistance of the swelling film medium through the presence of water molecules.

The swelling of beetle photonic structures in the presence of moisture has also been an inspiration for humidity sensors. The wing-case of beetles, like that of *Tmesisternus isabellae*, and *Hoplia coerulea*, are composed of an alternating photonic layered structure with air cavities. In the presence of humidity, these cavities fill with traces of water molecules, causing the structure to swell and, in turn, alter the refractive index of the wing-case. The wing-case of *Tmesisternus isabellae* changes from green to red,[345,346] whereas it turns from a blue-violet to green for *Hoplia coerulea*.[347,348] Inspired by the beetle's multilayer photonic structure, Colusso et al. developed an alternating composite structure of silk fibroin and titanate nanosheets, which have a low and high refraction index, respectively. The refractive index increases as the relative humidity increases, caused by the increase of hydrogen bonds and thus the swelling of the medium.[339] The visual color cues help quantify the degree of relative humidity in the environment. Qin et al. implemented a simpler design by covalently bonding a silicon wafer to a thin layer of transparent hydrogel. The hydrogel layer thickens with the presence of humidity, changing the refraction index. The group further implements an alternative hydrogel composition (i.e., poly(2-hydroxyethyl methacrylate-*co*-acrylic acid)) with three dissimilar thickness layers (positioned in parallel) for selectively detecting different volatile organic compounds (VOC). It is valuable to note that the response and recovery times for these sensors are 140 ms and 210 ms, respectively, with the spectrum of achievable colors spanning from violet to yellow-green.[338]

**Table 2.** Summary of bioinspired soft photoreceptors.

| Mechanism | Bioinspiration | Materials | Effective focal length (EFL) [mm] | Back focal length (BFL) [mm] | Refraction index | Other metrics | References |
|---|---|---|---|---|---|---|---|
| pH swelling/ shrinking → tuning FOV, focal length | Human crystalline lens, Arthropods compound eye | BSA membrane, SU-8 lens | 0.246–0.362 | NA | NA | Repeatable Tuning (100 cycles, pH 4–10) | [320] |
| DE actuation | Human crystalline lens | Silicone membrane, Sylgard 184 silicone-prepolymer (liquid lens), carbon grease | ≥ 80 | 17–129.4 | 1.41 | 20% focal length change in 175 µs, no degradation after 400× $10^3$ cycles | [312] (Figure 17B) |
| | | Silicone, carbon grease, glycerol (liquid lens) | mm lens: 3–5.4, smm lens: $391 \times 10^3$–$642 \times 10^3$ | NA | NA | mm lens: ≈0.54 s actuation and ≈0.24 s relaxation.<br>mm lens: 128 Ip mm$^{-1}$, smm lens: 90 Ip mm$^{-1}$.<br>smm lens functions horizontally and vertically | [326] |
| DE actuation, Electrowetting (EW) | Human crystalline lens | SU-8, PET, silicone oil (liquid lens), glass substrate | NA | 10.1–5.8 | 1.49 (silicone oil), 1.35 (water-based conductive liquid) | Resolution: 25.61 Ip mm$^{-1}$, small aperture size | [325] (Figure 17A) |
| Electromagnetic actuation | Human crystalline lens | Acrylic, PDMS, polyimide silicone, neodymium magnet, glass substrate | 10–79 | NA | NA | 900 ms actuation and relaxation time | [324] |
| Manual stage compression | Human crystalline lens | PDMS, PP, PMMA (liquid lens), barium flint (BaF8) lens, K9 (optical borosilicate crown crystal) | 18.1–285.3 | 129.4–17.0 | 1.63 (BaF8), 1.52 (K9), 1.52 (Optical Liq), 1.49 (PMMA) | Resolution 35–57 Ip mm$^{-1}$ (with different radius). | [327] |
| | | | | | | | 7.6× variation of back focal length |
| Semiconductor nanomembrane | Human retina | $MoS_2$, graphene, PI | NA | NA | NA | Photoabsorption coefficient: $>5 \times 10^7$ m$^{-1}$, photoresponsivity: 2200 A W$^{-1}$, small optical aberration, lower induced strain, minimal tissue damages and immune responses | [328] (Figure 17C) |
| | Human retina, Arthropods compound eye | PSi, NSi, polyimide, SU-8 | NA | 7.0–8.5 | NA | wide field of view, low aberration, high-spatial resolution | [311] (Figure 17D) |

Qu et al. measured VOC by implementing a design inspired by the human skin's wrinkling in the presence of ethanol vapor. Through the presence of VOC vapors, the fabricated multilayered film (Ag nanowire/silicon dioxide/polydimethylsiloxane) wrinkles due to the swelling of the medium, caused by microstructural instabilities (Figure 18B).[313] While most of the mentioned gas sensors are quantified through visual observations (i.e., wrinkling, swelling, and color alteration), there are still those whose molecular interactions are measured through circuit resistance.[336,337,340] It was observed that the sensor sensitivity increased through the application of a negative voltage gate, enhancing the interaction of noncondensable gas (i.e., carbon monoxide) with the fabricated sensor containing iron porphyrin and functionalized single-walled carbon nanotubes.[340]

#### 4.2.2. Liquid

Chemosensors for detecting liquids have been developed for vast applications: from quantifying rain drops[349] to culturing and mobilizing bacteria.[350] Taking inspiration from human skin, which can sense the slightest environmental change, a mineral hydrogel-based captive sensor was used to measure water droplets' mass and angle. This mineral hydrogel is neither excessively elastic (i.e., PAA) or viscous (i.e., ACC/PAA),

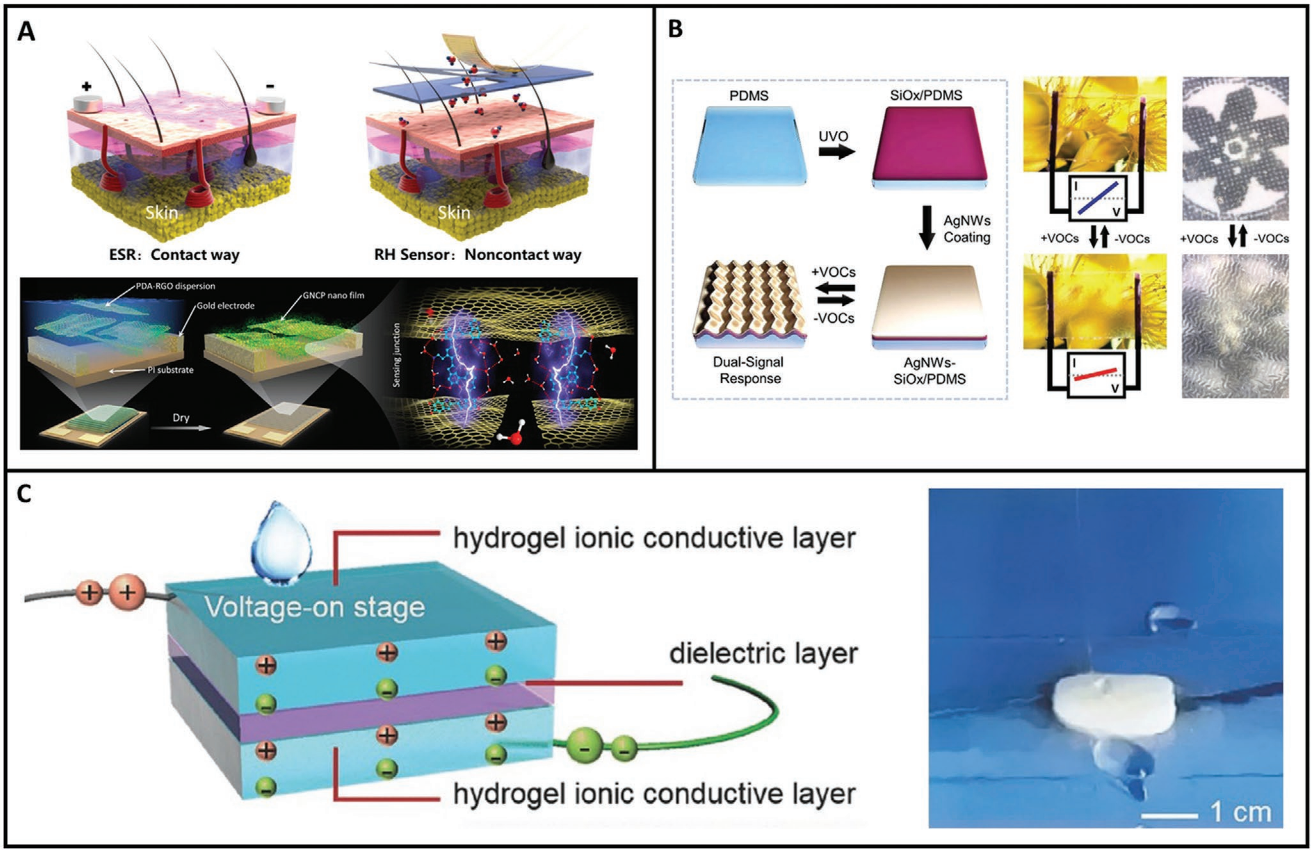

**Figure 18.** Bioinspired chemoreceptors. A) A humidity sensor inspired by weak molecular interactions and bonds. Hydrogen's intermediate intramolecular force results in the rapid binding and breakage of hydrogen bonds. This contactless humidity sensor uses an alternating graphene polymer composite to measure the collection of water molecules at a low and high relative humidity (i.e., 0–97%). It can measure human water metabolism by direct contact with the skin. B) Inspired by the human skin, this sensor wrinkles in the presence of VOCs, such as ethanol. It can also detect and quantify VOCs by measuring the resistance as the membrane is influenced by molecular interactions. This sensor is composed of iron porphyrin and functionalized single-walled carbon nanotubes. C) This hydrogel composite (ACC/PAA/alginate chains) sensor can detect water droplets as small as 20 mg, dropped from a height of 20 cm. A) Reproduced with permission.[336] Copyright 2017, American Chemical Society. B) Reproduced with permission.[313] Copyright 2017, Wiley-VCH. C) Reproduced with permission.[349] Copyright 2017, Wiley-VCH.

yet something in between, with self-healing ability and high sensitivity. The mechanism consists of a polyethylene (dielectric) film layered between two hydrogel films. The applied pressure creates an imbalance of capacitance between the dielectric film and the two hydrogel films. The capacitance is detected by a bridge circuit and converted to an output current. The change in capacitance increases with each water droplet (Figure 18C).[349] While the sensor is about three times more sensitive (i.e., 0.17 $\text{kPa}^{-1}$) than other crosslinked hydrogels, it is not as sensitive as sensors with microstructures.[350] A summary of the above-mentioned designs, along with additional metrics, can be found in **Table 3**.

### 4.3. Mechanoreceptors

Soft strain and pressure sensors hold particular importance since they can be used to monitor humans' physiological conditions. The majority of the below-mentioned studies have adhered their strain and/or pressure sensors to different locations of the human body to take measurements of vital metrics such as pulse, breathing, talking, chewing, and swallowing, in addition to the body, limb, and joint motions. This section will also explore flow sensors, specifically those found in fish and amphibians. They have been implemented in detecting subtle vibrations and flow fields.

#### *4.3.1. Strain Sensors*

Recently developed strain sensors have enhanced their performance and capability by taking inspiration from nature. Such advancements include a wide strain range, high sensitivity, stretchability, and quick response and recovery time. One area of bioinspiration comes from the microcracks and voids found in nature—from micro slits found upon spiders' legs and scorpions to the gaps found between hair cells and bundles. Arachnids (i.e., spiders and scorpions) have mechanoreceptors on their legs known as slit sensillum, which consists of distributed parallel microchannels upon their exoskeleton near their joints. The movement of their joints and environmental vibration, deform and squeeze (i.e., decrease in channel width)

**Table 3.** Summary of bioinspired soft chemoreceptors.

| Mechanism | Bioinspiration | Materials | Limit of detection (LOD) | Response time [s] | Recovery time [s] | Other metrics | References |
|---|---|---|---|---|---|---|---|
| Humidity, VOC: Hydrogen bond | Moisture sensing systems (human skin), biomolecular interaction (noncovalent intermolecular weak interactions, proteins and molecules) | Graphene nanochannels-confined poly(dopamine) (GNCP) | Relative humidity: 0–97% | 0.02 | 0.017 | Holds functionality while bent | [336] (Figure 18A) |
| VOC: Hydrogel swelling interferometer, colorimetric humidity | Cell or protein soft layer of color-changing animals (e.g., cephalopods, squid, beetle) | Hydrogel, Si wafer, poly(HEMA-*co*-AAc) | 1.74 µg $\mathrm{mL^{-1}}$ (ethanol vapor), 0.09–1.38% error | 0.14 | 0.21 | NA | [338] |
| Gas, VOC: Chemical molecule-trigger, instability of multilayer swelling, transparency | Human skin wrinkle long-exposure to ethanol vapor | AgNW, SiO, PDMS | VOCs: 18–47 $\mathrm{J^{1/2}\,cm^{-3/2}}$ (ethanol: 26.0 $\mathrm{J^{1/2}\,cm^{-3/2}}$, ethanol vapor: 0.2%) | 240–840 | NA | High selectivity to ethanol vapor, and not to toluene | [313] (Figure 18B) |
| Humidity: Volume change through water absorption/desorption, Bragg reflector with humidity responsive optical properties | Beetle (*Hoplia coerulea*) cuticle, color change in presence of moisture, both spider silk and silkworm silk show cycling contraction induced by humidity | Silk fibroin, titanite nanosheets (TNSs), $\mathrm{SiO_2}$ | 0.54nm, Relative humidity: 10–80% | 50 | ≈500 | Linearity at 360m with 0.28 sensitivity. | |
| | | | | | | 1–2% hysteresis for wavelength position, bandwidth, and transmittance. | [339] |
| | | | | | | High refractive index silk (HRIsilk): 1.80, Regenerated silk fibroin (Rsilk): 1.56. | |
| Humidity, water droplet (i.e., angle and mass): Electromechanical, micro/nano cracks, swelling effect enlarged the gaps among conductive nanofillers | Hydrogen bonding and noncovalent interactions | Hybridized nano carbons of graphene, CNTs, CNCs | NA | ≈25–100 | NA | Micro/nano cracks enhanced sensitivity by 65× | [337] |
| Water droplet: Capacitance pressure | Human Skin, sensing water droplets | Amorphous calcium carbonate (ACC) nanoparticles, PAA, alginate chains | NA | ≈0.1-0.9 | NA | Detect water droplet of 20 mg dropped from 20 cm height | [349] (Figure 18C) |

these arrayed channels, exciting the receptors and signaling the insect of potential predators.[351–353] Han et al. took inspiration from the forest scorpion's *Heterometrus petersii* radial slit sensillum arrays to design a flexible strain sensor. Through solvent induction (i.e., ethanol swelling and evaporation), radial channels were created on a polystyrene (PS) surface. The PS crack design was transferred to a PDMS medium through epoxy mold fabrication, which was then sputter-coated with gold nanoparticles. Copper paste and wires were placed at the ends of the sensor to measure the change in resistance when bending the sensor. Upon compression, the channel width decreased, while upon tension, the channel width increased. When compared to the base design without channel arrays, the implemented bioinspired microchannel arrays increased the gauge factor by ≈sevenfold.[354]

Others have taken advantage of micro- and nanocracks in their design, but on a more dynamic level. One design used CNCs in its composite mixture to regulate and distribute the nanocarbon of graphene with CNTs through noncovalent interactions and hydrogen bonds. Cured into polyurethane (PU) elastomer, micro- and nanocracks can dynamically propagate and recover when the elastomer is stretched and relaxed, respectively. The sensor's deformation has shown enhanced sensitivity (i.e., gauge factor) by 182 times, which has been achieved through CNCs' ability to rearrange fragmented nanocarbon structures.[337] Miao et al. developed a more controlled crack propagation by taking structural inspiration from the micro- and nanovoids in human inner ear hair cells and bundles, respectively. These hair cells, also known as stereocilia, are responsible for sensing sound vibration and transforming them into neural impulses sent to the brain.[355,356] Through a soft lithography and molding process, PDMS nanopillars were fabricated and then immersed into ethanol. With the evaporation of ethanol, lateral capillary forces induced the formation

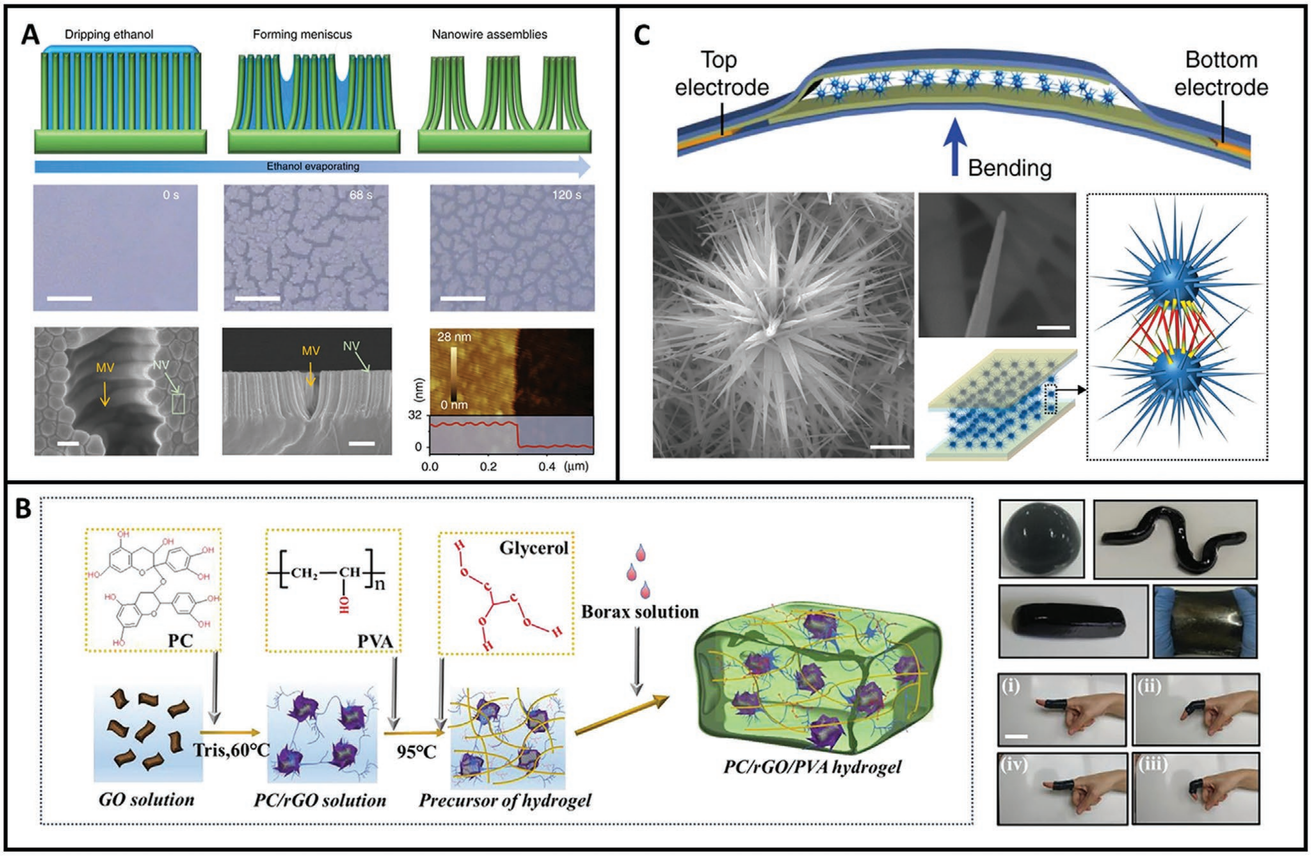

**Figure 19.** Bioinspired strain mechanoreceptors. A) These PDMS nanopillars get their structural inspiration from stereocilia bundles of a cochlea. Through the process of ethanol saturation and evaporation, pillars are bundled up with macrovoids between bundles and nanovoids within each bundle. The hierarchical structures allow for a two-step cracking process, increasing the strain sensitivity (gauge factor: 107.45%). B) The given human skin inspired hydrogel can easily conform and sense subtle changes. Its mussel inspired self-healing (95.73%, 3 s) and adhering ability, make it a perfect medium for ECG and EMG recording. C) This dual strain–pressure sensor has been inspired by the interlocking of biological bristles and cilia. These ZnO spiky microparticles, sandwiched between a PDMS membrane, deform and interlock with one another upon membrane deformation. A) Reproduced with permission.[315] Copyright 2019, Nature Publishing Group. B) Reproduced with permission.[362] Copyright 2020, Elsevier. C) Reproduced with permission.[367] Copyright 2018, Nature Publishing Group.

of pillar bundles. The pillar bundle assembly was coated with a platinum film, such that the electrical resistance could be measured upon structure deformation. The design allowed for strain to be measured at low and high ranges, through microvoids among pillar bundles and nanovoids between discrete pillars. This mechanism allows for the gradual formation of cracks and voids, thus increasing the durability and sensitivity range of the sensor (**Figure 19**A).[315]

Much of the existing strain sensors have been inspired by the human skin's tactile ability, with diversified designs and composition. Through the use of iron(II,III) oxide nanoparticles in a carbon fiber aerogel (CFA) and silicone resin composite, a group was able to design a dual contact/contactless strain sensor. The carbon fibers provide the conductive medium of the sensor, whereupon their displacement with strain increases the electrical resistance. Iron(II,III) oxide nanoparticles allow for contactless spatial sensing with the presence of a magnetic field, which displaces the carbon fibers and thus the change in electrical resistance.[357] Yang et al. fabricated a woven grid graphene structure upon a copper mesh through chemical vapor deposition. The graphene woven fabric (GWF) was displaced onto a PDMS film through the transfer process, and silver conductive paste was applied to adhere electrical leads. The design improved the biaxial strain and stress, while still preserving sensor sensitivity.[358] A more simplified fabrication process was used to develop a graphene-based sensor, where a strip of paper was repeatedly immersed into an aqueous GO solution and was allowed to dry upon a glass surface. This process was repeated 20 times, after which the GO coated paper was immersed into a hydroiodic (HI) acid solution and surface baked until the HI evaporated. The surface baking caused an asymmetry between the bottom and top side of the GO coated paper, where the bottom side (directly in contact with the heated surface) obtained a smoother surface than the top side. Copper foils were adhered to the ends of the top surface using silver conductive paste, allowing for electrical resistance to be measured when the GO coated paper is bent. Contactless bending can be accomplished through the exposure of a light source since graphene is a photothermal material. This is an adverse effect of the phenomenon referred to as goosebumps, which the authors take inspiration from.[359] Goosebumps occur upon exposure to cooler environments, where hair follicles are contracted through inner skin muscles (i.e., Arrector pili muscles) tensing, causing hairs to become erected.[360]

In conjunction with graphene (Gr), some have implemented greater mechanical stiffness in their strain sensors. This was accomplished by augmenting their composite with polyacrylic acid (PAA) and ACC and utilizing the process of biomineralization. This process of biomineralization is formulated through crosslinkers between the graphene nanosheets and calcium ions, and the hydrogen bonds between the graphene nanosheet with PAA and itself. As a result, the composite's mechanical properties were strengthened. The Gr-PAA-ACC composite was placed between the double-sided tape with copper leads at each end for testing purposes; however, it can function as a standalone as well.[361] Different hydrogel composites have shown promising capabilities for developing strain sensors inspired by human skin. Pan et al. designed an electronic skin composed of proanthocyanins (PC), RGO, and polyvinyl alcohol borax (PVA-borax) hydrogel. The PC/RGO/PVA hydrogel film (with metal leads) could easily conform to establish close skin contact and measure patient electrocardiography (ECG), and electromyography (EMG) signals with low signal to noise ratios and smooth output signals (Figure 19B).[362]

Some strain sensors have been designed with self-healing abilities, allowing them to be reused at full capacity (i.e., 98–99% recovery) after seconds of healing.[363,364] Inspiration has also been obtained from mussels, which are capable of self-healing and self-adhesion by using levodopa protein to form strong hydrogen bonds.[365] To implement self-adhesive capability in hydrogel composites, Gao et al. added catechol groups (i.e., poly(acrylamide-*co*-dopamine)) to their lithium chloride and gelatine composite. Gelatine further increases the crosslinking network structure, thus enhancing the mechanical properties of the composite sensor.[366] In an earlier design, the group used poly(acrylamide-*co*-dopamine) with functionalized single-wall carbon nanotubes (FSWCNT)[363] for their hydrogel compound. FSWCNT/hydrogel has shown to provide a stable structure with a greater gauge factor and percent resistance change compared to composites consisting of graphene/hydrogel and silver nanowire/hydrogel.[364] **Table 4** summarizes the above mentioned designs along with additional metrics.

#### *4.3.2. Dual Strain and Pressure Sensors*

Some hydrogel composite sensors can sense both strain and pressure. Lei et al. developed a hydrogel composite consisting of ACC nanoparticles crosslinked with PAA and alginate chains (ACC/PAA/alginate), introducing a structural balance between elasticity and viscosity. Two ACC/PAA/alginate hydrogel films were developed and layered with a polyethylene (dielectric) film in between, and a metal wire was placed on each hydrogel film. The capacitance of the sandwiched structure (hydrogel and dielectric films) changes through the application of pressure and/or strain. The sensor is about three times more sensitive (i.e., 0.17 $kPa^{-1}$) than other crosslinked hydrogels when tested under a pressure range between 0 to 1 kPa, and it has reversibility for a strain range between 0% and 100%.[349] Moreover, an ionic conductive hydrogel strain/pressure sensor was created through the addition of lithium chloride (LiCl) to the other components, which included sodium dodecyl sulfate (SDS), lauryl methacrylate (LMA), and hybrid latex particles (HLPs). Through micellar copolymerization, the mentioned composite was formulated, producing crosslinked network structures. This resulted in a wide strain sensing range (i.e., 0.25–2000%) and pressure sensitivity (gauge sensor) of 5.44%.[368]

Some pressure/strain sensors have taken inspiration from the insect bristles and hair, which cover the insect's entire exoskeleton, allowing them to sense environmental vibrations. Specifically, the tapered structure of bristles and hair-to-hair interlocking/detangling have been points of inspiration.[369–371] Through the mixture of sodium hydroxide and zinc acetate dihydrate in deionized water, zinc oxide (ZnO) microparticles were formulated as the solution was heated at 40° in an autoclave. The formed microparticles exhibit a series of densely spiked spherical particles. These particles were transferred between two layers of PET films coated with indium-tin oxide (ITO). The entire double-layer film was then encapsulated within a PDMS membrane. The copper foils connected to the upper and lower ITO/PET layers record resistance as the spiky microparticles interlock and deform under applied pressure and/or strain. This unique, yet simple design can detect pressure as low as 0.015 Pa (with a high of 200 Pa) and has a strain gauge factor of $>10^4$ (Figure 19B).[367] Another group capitalized on the interlocking and cracking of hierarchical microstructures by designing their sensor through the process of in situ GO reduction upon a 3D PU structure. They then coated the structure with conductive polyaniline nanohair (PANIH). This sponge-like structure introduced structural microcracks under minimal deformation and interlocking of nanohairs under greater deformation. Under 0–10% strain range, deformation-induced microcracks increased structural voids and, in turn, decreased the conductive path. As the electrical resistance increases, the output current decreases. Under 10–20% strain range, the conductive path increases through the interlocking of nanohairs, causing the output current to increase gradually. With strain ranges greater than 20%, the output current increases faster, caused by the increase of interlocking and contact area between nanohairs. The design provides a wide pressure sensing range of 27 Pa to 25 kPa.[372] To create similar hierarchical structures, Dong et al. made use of actual sea sponge *Phylum Porifera* as the base of their sensor design. Through a dipping and drying process, the sponge was coated with polydomine reduced graphene oxides (pDA-RGO) and conductive AgNWs. Using conductive silver paste, copper wires adhered to the augmented sponge structure to measure its resistance upon deformation. Under structural deformation, the conductive contact area increases, thus decreasing the sensor resistance. In the absence of microcracks, a linear relationship between pressure and strain was attained for 0–40% kPa pressure range, with a gauge factor of 1.5 at 60% strain (**Figure 20**A).[373]

Taking inspiration from human skin, some have designed triboelectric smart skins. The design developed by Bu et al. has dual pressure and strain sensing capability. The fabrication process initiates with pouring a silicone rubber mixture consisting of aggregation-induced emission (AIE) powder on AgNW solution. Upon curing, the copper tape was adhered to the top before pouring the second layer of the silicone mixture. When the second layer was cured, the surface was coated

**Table 4.** Summary of bioinspired soft mechanoreceptors – strain sensors.

| Mechanism | Bioinspiration | Materials | Gauge factor (%) | Min strain [%] | Max strain [%] | Response time [s] | Recovery time [s] | Other metrics | References |
|---|---|---|---|---|---|---|---|---|---|
| Piezoresistive, micro/nano cracks propagation | Forest scorpion (*Heterometrus petersii*) leg slit sensillum | PS, PDMS, Cu, Au | Tension: 5888.8, compression: 33.92 | –1.2 | 2 | 0.297 | NA | Microcrack arrays enhanced performance | [354] |
| | Weak hydrogen bonding and noncovalent interactions | Graphene, CNTs, CNCs | 1129 | 5 | 20 | ≈0.5–10 | NA | CNCs enhanced sensitivity by 182× | [337] |
| | Stereocilia bundles of a cochlea (hair cells) | PDMS, PEIE | 107.45 | 0.005 | 130 | NA | NA | Hierarchical structure allows for two-step cracking | [315] (Figure 19A) |
| Piezoresistive, magnetic | Human skin (i.e., sensitive to touch and temperature) | $Fe_3O_4$ nanoparticles, silicone, CFA | NA | 20 | 60 | 0.033 | NA | Dual strain/magnetic sensor, eco-friendly | [357] |
| Piezoresistive, graphene-based | Human skin (i.e., sensitive to touch and temperature) | GWFs, PDMS | 500 ($\varepsilon$: 0–2%), $10^3$ ($\varepsilon$: 2–6%), 106 ($\varepsilon > 8\%$) | 2 | 8 | NA | NA | | [358] |
| | | Graphene oxide, paper | tension: 4.27, compression: 7.84 | NA | NA | 0.079 | NA | | [359] |
| Piezoresistive, hydrogel-based | Human skin (i.e., sensitive to touch and temperature) | LiCl, SDS, LMA, shell HLPs | 1.466 ($\varepsilon$: 0–80%), 5.44 ($\varepsilon > 80\%$) | 0.25 | 2,000 | 0.151 | 73 | | [368] |
| Piezoresistive, hydrogel-based | Human skin (i.e., sensitive to touch and temperature) | Conductive hydrogel, PC/RGO, PVA-borax | 4.29 ($0\% < \varepsilon < 60\%$), 5.26 ($60\% < \varepsilon < 260\%$), 14.14 ($260\% < \varepsilon < 550\%$) | 0.1 | 5,000 | ≈0.1–0.6 | ≈0.2–1.1 | Self-healing: 95.73%, 3 s, compliance: 1 mm | [362] (Figure 19B) |
| | Mussel's adhesion and self-healing | FSWCNT, PVA, PDA | NA | NA | NA | ≈1–3 | ≈1–3 | Self-healing: 99%, 2 s.<br>Adhesion strength: 5.2–9.2 kPa | [363] |
| | | Single wall carbon nanotube (SWCNT), graphene, silver nanowire | SWCNT/hydrogel: 0.24 ($\varepsilon$: 100%), 1.51 ($\varepsilon$: 1000%), graphene/hydrogel: 0.92, Silver nanowire/hydrogel: 2.25 ($\varepsilon$: 1000%) | 2 | 1,000 | ≈0.2–1.8s | ≈0.6–3.5 | Self-healing: 98%, 3.2 s | [364] |
| | | Gelatin, PDA-*co*-PPA, LiCl | 2.566 ($\varepsilon$: 20–61%), 2.814 ($\varepsilon$: 61–100%) | 1 | 1,150 | ≈4s–34 | ≈4–39 | Maximum adhesive strength: 23 N $m^{-1}$, Self-healable, puncture resistance | [366] |
| | Biomineralization process | graphene, PAA, ACC | NA | 1 | 200 | ≈15–22 | ≈15–22 | Works in air and water | [361] |
| Piezoresistive | Sea sponge structure | Sea sponge (Phylum Porifera), pDA-RGO, AgNWs | 1.5 | 0 | 60 | 0.054 | 0.147 | | [373] (Figure 20A) |
| Triboelectric photonic, photocurrent | Sea sponge structure | AgNW, silicone rubber | NA | 0 | 160 | 0.09 | 60 | | [374] |

with copper, whereupon parallel lateral microcracks were created through axial tension. Under tensile load, the AIE powder (within the silicone rubber) illuminates green in the presence of UV light source, with the illumination intensity increasing as strain increases. The sensor was placed on a robot hand to show the degree of joint bending through illumination intensity. The sensor has a pressure sensitivity ranging from <0.17 to >1.7 kPa and strain range from 0% to 160%. The sensor's self-powering abilities hold a great advantage. Triboelectric effect based sensors begin operation with equal distribution of positive and negative charges within the fabricated sensor and the external medium it will soon contact. As the sensor

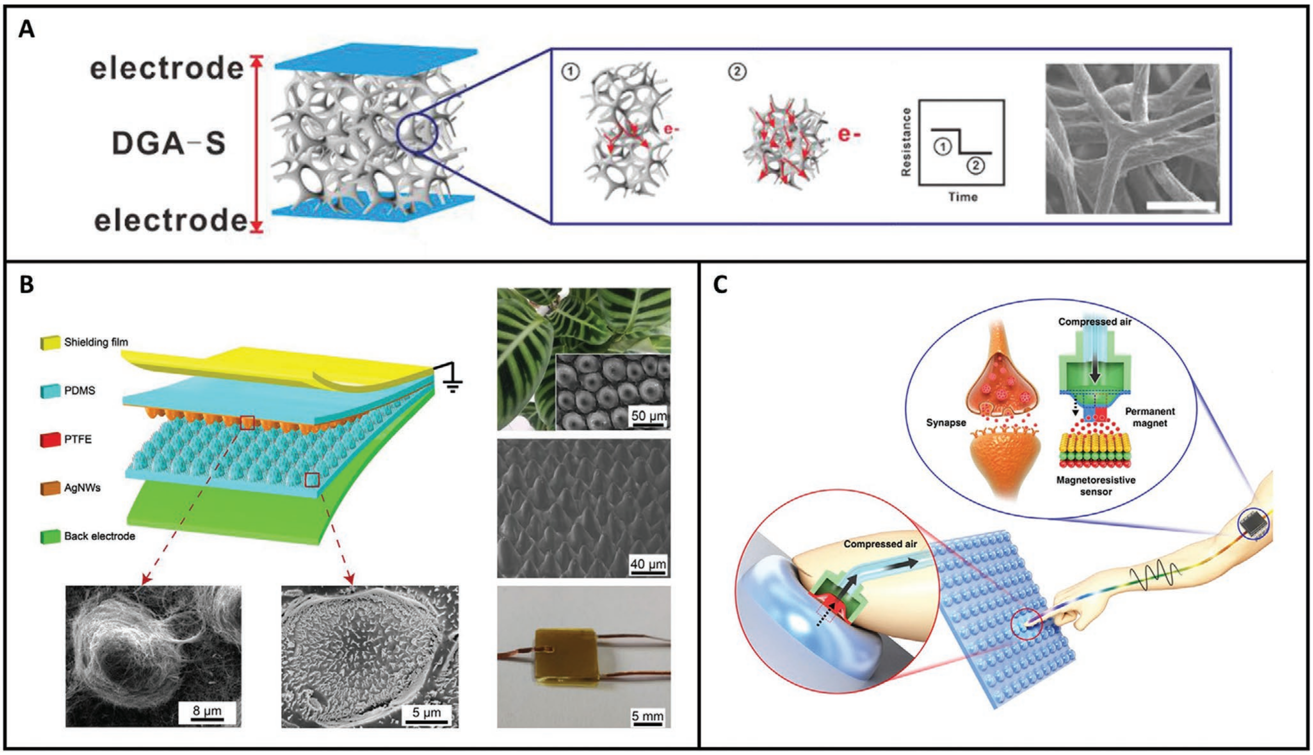

**Figure 20.** Bioinspired pressure mechanoreceptors. A) A sea sponge was coated with AgNWs and pDA-RGO. The sponge's hierarchical structure and nodal connections allow it to undergo large deformations. Upon deformation, the conductive surface contacts increase, and thus the sensor's resistance decrease. B) Taking the topographical design of a zebra plant leaf, a triboelectric pressure was made of PMDS coated with AgNWs and PTFE, which was seen to enhance pressure by 14 times. C) Taking inspiration from the human synapse system, when air pressure is applied, the permanent magnet (embedded into PDMS membrane) descends toward the distanced magnetoresistive sensor. This sensor was able to detect a tactile stimulation of 1000 Hz, with no distortion and hysteresis. A) Reproduced with permission.[373] Copyright 2018, Elsevier. B) Reproduced with permission.[375] Copyright 2019, Wiley-VCH. C) Reproduced with permission.[314] Copyright 2017, Nature Publishing Group.

approaches the external medium, free electrons are drawn from the ground through the sensor's conductive lead. In the process, a current is generated until contact between the sensor and external medium is established. As the sensor distances from the external medium, the free electrons flow back through the sensor's conductive lead into the ground. In the process, the direction of current is changed until the maximum distance between the sensor and external medium is reached, and electrical equilibrium is attained.[374]

### *4.3.3. Pressure Sensors*

While some mechanoreceptors have dual strain- and pressure-sensing capabilities, others are limited to detecting pressure, but with more precision. Wang's research group fabricated another triboelectric smart skin pressure sensor. The difference is the lack of AIE powder and copper surface coated microcracks, and second silicone rubber layer consisting of triangular microprism array structures. These microstructures not only improved pressure sensitivity when compared to their earlier design,[376] but it also improved surface traction when the sensor was incorporated into a pneumatically actuated gripper and crawler.[377] Yao et al. implemented triboelectric microstructures by duplicating the microconed array structures found on the surface of the *Calathea zebrina* leaf. Through the process of positive molding, two PDMS films with microconed surface topology were created. One PDMS film was coated with AgNWs, while the other with polytetrafluoroethylene (PTFE) speckles. The two PDMS films with their microstructures were placed facing one another and were stacked between an upper shielding film and a lower electrode film. The bioinspired microstructures increased pressure sensitivity by 14-fold (Figure 20B).[375]

Taking inspiration from the human skin's tactile ability and bristle interlockings found in nature, Pu et al. developed a pseudocapacitor pressure sensor with a hierarchical structure composed of zinc oxide nanosheets and nanorods. Through compression of two facing sheets with hierarchical nanostructures, interlocking between nanostructures is increased, increasing the conductive pathway and thus decreasing the electrical resistance. As pressure increases, so does the output current. The minimum detected pressure was 0.4 Pa.[378] Another group took inspiration from the sensing capabilities of hair cells and developed graphene-coated-cilia arrays (GCCAs) through in situ growth method. The fabrication process consists of mixing Co and PDMS resin in ethyl acetate and placing the mixed solution between two magnets. In the presence of a magnetic field, the Co particles are accumulated and shape the cilia arrays. Ethyl acetate is then evaporated, leaving PDMS as the flexible base layer of the cilia arrays. Last, the cilia arrays were made conductive by coating them with graphene. The GCCAs membrane was mated with an interdigitated graphene electrode film. With applied pressure, the electrical resistance decreases as the contact between cilia arrays against the electrode film increases. The sensor can detect pressures as low as 0.9 Pa and as high as 100 Pa.[379]

In addition, some have taken inspiration from the microstructures found in spinosum, which is the layer between the dermis and epidermis of the human skin. The epidermal impact produces heightened localized sensing, caused by spinosum microstructures increasing the stress concentration around sensory receptors in the dermis.[380] Boutry et al. designed a dermis/spinosum/epidermis structure of their own through lamination assembly of photolithography patterned membranes. The dermis membrane consisted of CNT dome arrays with a PU backing layer. The spinosum/epidermis membrane consisted of CNT microstructure pyramid arrays in a phyllotaxis spiral pattern. The two membranes were stacked with the array structures facing one another, with a polyhydroxybutyrate–polyhydroxyvalerate (PHB-PHV) film between them to insulate the arrayed capacitors. The sensor can measure shear and pressure, detecting as low as 0.5 kPa and as high as 100 kPa.[381] Pang et al. made their replica of the spinosum microstructure by using coarse paper. Two PDMS molds of the structure were made and dip-coated in GO. The GO was then reduced (RGO) through applied heat. The two RGO/PDMS fabricated molds were stacked with microstructures facing one another. With a load applied, the contact and interlocking of microstructures lead to the decrease in electrical resistance. The pressure sensor holds linearity until 2.6 kPa.[382]

Contactless pressure sensors were developed by taking inspiration from the human synapse system, which sends electrochemical signals between central nerve cells when a mechanoreceptor is signaled.[380] Their design is unique, yet simple. An air chamber is covered with a PDMS membrane with an embedded permanent magnet held at a distance from a magnetoresistive sensor that resides below it. With the air pressure changing in the chamber, the PDMS membrane is deformed, varying the gap distance between the permanent magnet and magnetoresistive sensor. The fabricated anisotropic magnetoresistive (AMR) sensor in concurrence with the planar Hall effect (PHR) sensor was used to measure the magnetic field change. A hybrid Wheatstone bridge circuit was used to measure the output voltage. An anti-symmetrical magnetic field is created with the vertical descension of the permanent magnet toward AMR/PHR sensor. The sensor's voltage is recorded as an alternating current is applied through the Wheatstone bridge (gold) circuit. The variation in the output voltage is a consequence of both the AMR and PHR sensor. The pressure sensor showed a detection range of 6– 400 kPa (Figure 20C).[314] The group implemented this sensor as tactile feedback sensing in their robotic hand gripper, which was able to hold a variety of objects without inflicting any damage.[383] The above mentioned designs along with additional metrics are summarized in **Table 5**.

#### *4.3.4. Flow Sensors*

A notable physical characteristic on both fish[384–386] and amphibians[387–389] is the lateral line system, which runs lengthwise from the head down along their body. The lateral line systems consist of a series of superficial (in fish and amphibians) and canal (fish) neuromasts. Neuromasts are mechanoreceptors that detect surrounding vibrations and flow fields, providing proprioception and the ability to differentiate between objects, prey, and flow rates and patterns.[390–393] While fish and amphibians have other mechanoreceptors (e.g., hearing) and sensory receptors (i.e., chemo and photo), the particular mechanoreceptor has been observed to enhance their efficiency in swimming and maneuvering.[393,394]

Each neuromast is formed of nerve hair cells encapsulated by a gelatinous porous membrane called cupula. Superficial neuromasts (SN) consist of tens of hair bundles, and their cupula are elongated (rounded) cone-shaped. In contrast, canal neuromasts (CN) hold hundreds to thousands of hair bundles and their cupula are dome-shaped. Superficial neuromasts are located on the body's surface and detect steady to low-frequency flows. Canal neuromasts are housed at the base of lateral line canals and situated between inlet pores, exposed to the surrounding environment. The deflection of these neuromasts cause the deformation of surrounding cell membranes, which leads to the opening and closing of ion channels. The produced electrical potential transmits neural signals to the brain, alerting the animal of surrounding perturbations, thus allowing it to respond accordingly.[389,393,395]

The structural design of neuromasts have been a point of inspiration for the advancement of highly sensitive and accurate flow sensors.[396–399] Most of the existing designs are based around the microfabrication of cantilever rigid pillars, representing the hair cell(s), centered upon a deformable base film, representing the surrounding cell membranes. The pillar deflection causes membrane deformation, outputting a voltage reading through a resistive (i.e., strain gauge) or capacitive mechanism. The resistive mechanism is generally a Wheatstone bridge circuit, which allows for deflection to be measured in multiple directions. Pillar deflection induces imbalance to the bridge circuit, generating an output voltage (**Figure 21**A).[400–402] The applied capacitive mechanism includes principle mediums such as piezoelectric (PZT) polymers (Figure 21B),[403,404] IPMC,[405,406] and traditional capacitor setup (as pillars) (Figure 21C,D).[407–409] Last, optical fibers[410,411] have also been recently explored as a flow sensing mechanism (Figure 21E).

A PZT polymer, such as lead zirconium titanate, can act as the sensing membrane whereupon the pillar is centered and fixed on a circular/ring[404] or circular/gapped (i.e., top and bottom)[403] electrode. Upon the pillar deflection, the PZT polymer membrane is deformed causing a collected change in the electrodes, reflected in the output voltage. The fabrication of an IPMC sensor is commonly on a larger scale (i.e., millimeter to centimeter), and consists of chemically plating an ionic polymer membrane (i.e., Nafion) with a conductive material (i.e., platinum). Vibration and flow deform an IPMC sensor[405,406] causing the ions to migrate and rearrange, and in

**Table 5.** Summary of bioinspired soft mechanoreceptors – pressure sensors.

| Mechanism | Bioinspiration | Materials | Pressure sensitivity ($kPa^{-1}$) | Min pressure [kPa] | Max pressure [kPa] | Response time [ms] | Other metrics | References |
|---|---|---|---|---|---|---|---|---|
| Magnetic (planar Hall effects), hybrid Wheatstone bridge | Human synapse system | PDMS, AMR, magneto resistive (MR) | (detect 30 mg) | $6 \times 10^{-3}$ | 400 | 40 | Tactile stimulation: 1000 Hz (no distortion and hysteresis) | [314] (Figure 20C) |
| | | PDMS, MR-sensor (Ta/Ni/Fe/IrMn/Ta) | 0.016 | $6 \times 10^{-3}$ | 350 | NA | Resolution: 300 µN, noise ratio: 0.17% of maximum signal change (due to pressure) | [383] |
| Capacitive | Human skin (i.e., dermis/spinosum/epidermis) | CNT, PU, PHB-PHV | 0.19 (<1 kPa), 0.10 (1 < P < 10 kPa), 0.04 (10 < P < 20 kPa) | <0.5 | 100 | NA | Minimal hysteresis, response time: millisecond range | [381] |
| Piezoresistive, hierarchical structure interlocking | Human skin (i.e., dermis/spinosum/epidermis) | RGO, PMDS | 25.1 (0–2.6 kPa), 0.45 (>2.6 kPa) | 0 | 2.6 | 120 | Recovery time: 80 ms, linearity range up to 2.6 kPa | [382] |
| | Human skin (i.e., sensitive to touch) | ZnO nanorods and sheets | 0.5–1200 | $4 \times 10^{-4}$ | 10 | 2 | | [378] |
| Piezoresistive | Human skin (i.e., sensitive to touch) | LiCl, SDS, LMA, shell HLPs | 0.131–0.051 | 0 | NA | 152 | Recovery time: 147 ms, repeatability: 3–25 kPa | [368] |
| Triboelectric, photonic | Human skin (i.e., sensitive to touch) | AgNW, silicone rubber | 34 (<0.17 kPa), 2.6 (0.17–1.7 kPa), 0.13 (>1.7 kPa) | $17 \times 10^{-2}$ | $17 \times 10^{-1}$ | 90 | Recovery time: 60 ms | [374] |
| Triboelectric | Human skin (i.e., sensitive to touch) | silver-flakes, silicone rubber | 0.29 | $63 \times 10^{-3}$ | 20 | NA | Sensitivity in low pressure regime | [377] |
| | Surface structure of plant (*Calathea zebrina*) leaf | PTFE, AgNWs, PDMS, | 9.08–127.22 | 5 | 50 | NA | PTFE enhanced pressure- sensitivity by 14× | [375] (Figure 20B) |
| Piezoresistive, hierarchical structure interlocking | Sea sponge structure | sea sponge (*Phylum Porifera*), pDA-RGO, AgNWs | 0.0016 | 0 | 40 | 54 | | [373] (Figure 20A) |
| | Spider leg slit sensillum | PANIH, GO, PU | 0.0021 | $1 \times 10^{-2}$ | 25 | 22 | Recovery time: 20 ms, Detects 25 mg feather | [372] |
| | Biological bristles and cilia | ZnO microparticles, PDMS, PET, ITO | 75–121 (0–0.200 kPa) | $15 \times 10^{-6}$ | $2 \times 10^{-1}$ | NA | | [367] (Figure 19C) |
| Piezoresistive, magnetic | Biological bristles and cilia | PDMS, graphene, Co particles, Ca | 0.4 | $9 \times 10^{-4}$ | $1 \times 10^{-1}$ | NA | Frequency range: 0.1–10 Hz | [379] |

turn output a voltage. Wissman et al. injected liquid metal (i.e., eutectic gallium–indium) into a silicone cupula, creating three parallel capacitive plates. The plates are separated by the surrounding silicone, while connected at their base. During deflection, capacitance increases for the plate experiencing tension and decreases for the plate experiencing compression.[407,408] Wolf et al. fabricated a pillar composed of four equidistant optical (SMF-28) fibers with adhesive in between them and a common spherical tip. A segment along the length of each fiber was modified to have a fiber Bragg gratings (FBG) structure. The FBG structure creates periodic spacing within the fiber, altering its refractive index. Depending on the spacing, the illuminated light will reflect at different wavelengths. Therefore, the degree of pillar deformation (i.e., fiber compression and tension) can be measured through the refraction of light from the four optical fibers.[410,411]

Some researchers have implemented the cupula into their designs through drop-casting HA[400–402] or methacrylic anhydride modified hyaluronic acid-based (HA-MA)[403,409] hydrogel on pillar(s), encapsulating them. Aside from it increasing the pillar's cross-sectional surface area and stiffness, its structural porosity further increases the drag force through the material's hydrophilicity and swelling, resulting in a greater bending moment. Larger scale sensors utilized silicone[407,408] and

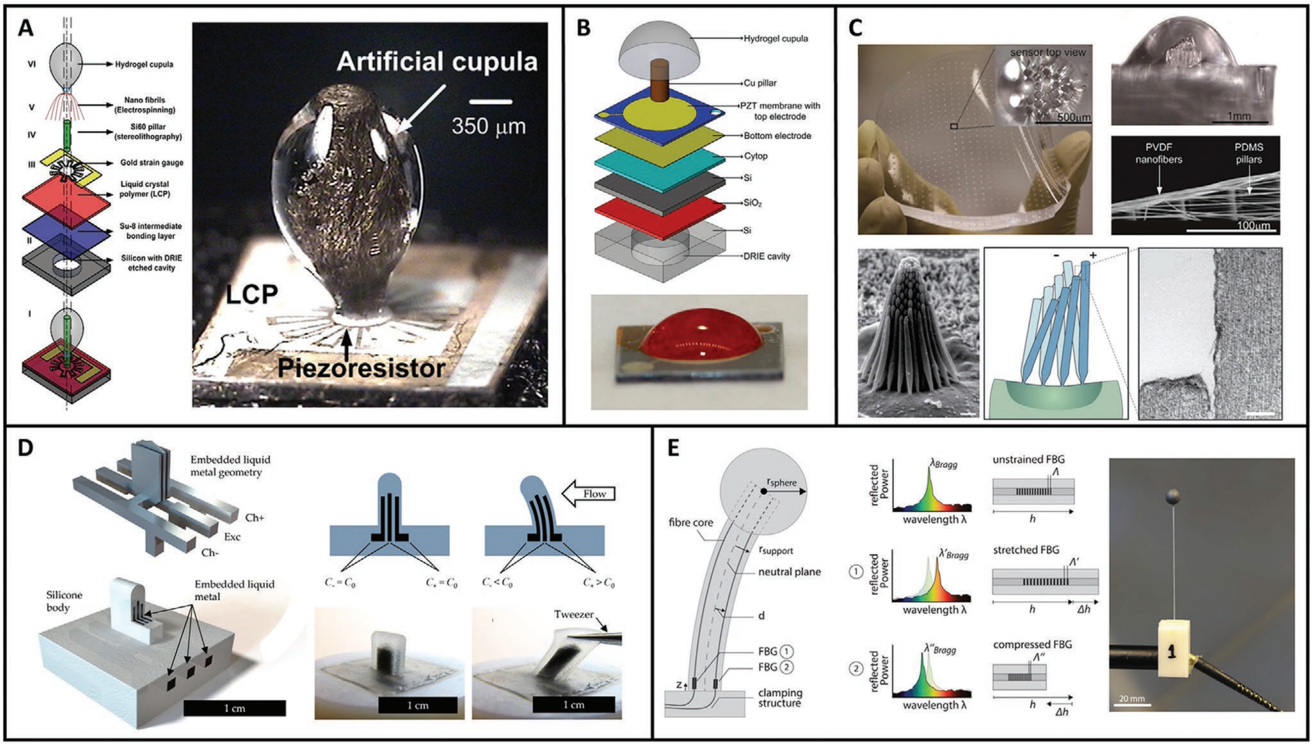

**Figure 21.** Bioinspired neuromast flow mechanoreceptors. The following are a collection of artificial micro flow sensors inspired by (superficial and canal) neuromast cupulas/bundles using the mechanism of: A) Resistive with Wheatstone bridge circuit, B) piezoelectric, C,D) capacitance with mechanical deflection, E) optical SMF-28 fibers with fiber Bragg gratings. A) Reproduced with permission.[402] Copyright 2016, Nature Publishing Group. B) Reproduced with permission.[403] Copyright 2017, AIP Publishing. C) Reproduced with permission.[409] Copyright 2016, Nature Publishing Group. D) Reproduced with permission.[407] Copyright 2019, MDPI. E) Reproduced with permission.[411] Copyright 2019, IOP Publishing.

PDMS[406] to coat the outer surface of the pillar. Others have taken an additional step by implementing nanofibers,[402,409] which link the hair cell tips to one another under the cupula. Through this, Asadnia et al. not only linked their pillars together with piezoelectric PVDF nanofibers but also used it as a sensing mechanism to measure the change in capacitance with fiber deformation.[409]

These sensors are fabricated from materials commonly used in microelectromechanical systems (MEMS), such as carbon (nanotubes),[401,403] silicon (i.e., Si60)[402,404] and epoxy-based photoresist (i.e., SU-8)[400,409] for the pillar; silicon,[400] lead zirconium titanate,[403,404] PDMS,[409] and other liquid-crystal polymers[402,404] for the base membrane, and gold[400–402] and/or carbon[403] for the capacitive or resistive mechanism. **Table 6** lists the above mentioned designs, along with additional technical details.

## 5. Concluding Remarks and Future Directions

This review discusses some of the essential components of bioinspired soft robotic systems: materials, actuators, and sensors. Recent advances in bioinspired soft robotics are surveyed, first by a primer on the materials used in the field, each characterized by unique strengths and weaknesses. Through exploring new compositions and unconventional materials, scientists and engineers have discovered improved materials to support the field as it evolves. Furthermore, by expanding the capacity for material selectivity, precision and control for actuators and sensors have been improved, and the design space for bioinspired soft robots has been broadened. Nonetheless, many soft materials struggle with short lifetimes due to the degradation of the materials. This is particularly true in the case of biohybrid designs where biological tissues are used. Moreover, soft bioinspired materials are often made from compounds that are sensitive to environmental changes. Although this can be a beneficial trait, leading to products such as soft sensors, it can also impact the applications they can be used for. Hydrogels are a particular example of this as they require an aqueous environment and thus, can not be used for dry applications.

Bioinspired soft actuators have received extensive efforts improving their mechanical and actuation properties in addition to their modeling and fabrication methods. Despite rapid advancements of bioinspired soft actuators, improvements are needed before they can be integrated into real-world applications. One of the limiting factors is their low output force. Although sufficient for small scale robots, it is challenging for soft actuators to compete with conventional actuators on larger scales. Low output work density, delayed response, and short lifespan are among other limitations that require further studies.

**Table 6.** Summary of bioinspired soft mechanoreceptors – flow sensors.

| Mechanism | Bioinspiration | Materials used | Sensitivity [mV (mm $s^{-1}$)$^{-1}$] | Resolution [mm $s^{-1}$] | Other Metrics | References |
|---|---|---|---|---|---|---|
| Resistive, Wheatstone bridge circuit | Blind cavefish (*Astyanax fasciatus*) neuromast cupula | Hydrogel, nanofibrils | | | | |
| | | Si60, Au, LCP, SU-8, Silicon | 22 000–77 000 | 39–18 | Young's modulus of the artificial cupula closely matches the biological cupula (10–100 Pa) | [402] (Figure 21A) |
| | | SU-8 , HA hydrogel, Au, Si, SiO2, Si | NA | NA | Four times higher sensitivity | [400] |
| | | CNT, HA hydrogel, liquid crystalline polymer, Vertically aligned multiwalled carbon- nanotubes (VACNT) bundle, Si wafer | 0.16 (air) | NA | | [401] |
| Piezoelectric | Canal neuromast cupula | Si, Au, PZT, Ti/Pt, $SiO_2$ | 0.8 (air), 22 (water) | 2.5 (air), 0.0082 (water) | | [404] |
| | | HA Hydrogel, PZT, Cu pillar | NA | $625 \times 10^3$ (water) | Hydrogel cupula enhanced sensor output by ≈2.1 × | [403] (Figure 21B) |
| Capacitance, mechanical deflection | Cilia bundle | HA-MA hydrogel, PDMS, PDVF nanofiber, Au | 0.3 | 0.008 | | [409] (Figure 21C) |
| | Canal neuromast cupula | Liquid metal eutectic gallium–indium, silicone (Ecoflex 00–30) | 0.0512 (deflection), 0.0632 (flow) pF/mm | NA | | [407,408] |
| IPMC | Canal neuromast cupula | Silicone oil/water, latex membrane, TangoBlack material (Object Connex 359, Stratasys) | NA | NA | Sensitivity over 20× higher with silicone than with water | [405] |
| | Superficial neuromast cupula | PDMS | NA | NA | Sensitivity with cupula enhanced by 20× at highest tested flow velocity (25 cm $s^{-1}$) | [406] |
| Optical fiber, FBGs | Superficial neuromast cupula | Optical SMF-28 fibers | (5 mm $s^{-1}$) | 0.005 | Linear Dynamic Range of 29 dB at 5 kHz sampling and 38 dB at 100 Hz sampling | [411] (Figure 21E) |
| | | | NA | NA | Euclidean localization error: 1.3 cm for a vibrating object, moving an object it is on average 3.3 cm. | [410] |

While being at its infantile state, much progress has been achieved in the field of bioinspired soft sensors. For instance, recent efforts have brought about miniature biocompatible optical aids and receivers; selective and accurate sensors for measuring humidity, volatile organic compounds, and noncondensable gases; surface contact pressure and/or strain sensors for monitoring of physiological conditions; and flow sensors detecting subtle vibration and flow fields. This is not to negate the limitations within recently developed soft bioinspired sensors. Like preexisting conventional sensors, the accuracy of soft sensors is range dependent. While they may hold a wide sensing range, sensor linearity is limited. However, this can be improved with modeling and system analysis. Due to the usage of soft materials, decreased lifespan and reduced reliability are unavoidable but can be mitigated through properly selecting material compositions and utilizing sensors within environmentally controlled facilities.

Soft robots could become pivotal in a wide variety of applications, especially in human interactive fields such as surgical robotics and rehabilitation exoskeletons, where dexterous soft tools are preferable. In addition to human interaction, soft robots would be highly desirable for the exploration of unstructured terrain as well as search and rescue operations, considering their deformable bodies and self-healing capabilities. In particular, tetherless soft robots are being developed to respond to noncontact stimuli such as light and electric fields, both of which have been shown to be very selective and precise actuation strategies.

In the future, bioinspired hybrid robots that incorporate a rigid frame with soft actuating components and soft sensing skins may be a potential direction to take.[412] This combined approach would offer both flexibility and strength. However, due to soft actuators being comparatively slow, hybrid robots utilizing bioinspired actuation tend to be slower compared to their fully rigid counterparts. There are also challenges in fabrication that currently inhibit these hybrids. Delamination, or detachment, of connection points between soft and rigid components during actuation, is an inherent problem for systems combining materials with different stiffnesses. In addition, systematic modeling and control of hybrid and soft robots are necessary for effective control.

With the advancements in the arena of soft materials, actuation, and sensing, the toolbox for building a soft robot is becoming more comprehensive. However, for it to be at par with conventional robotic systems, the design and fabrication of soft robots will need to become standardized. Furthermore, the development of rigorous models and controllers for soft bodies is essential. With such efforts, soft robotic systems will become robust and agile for a diverse assortment of applications.

## Acknowledgements

R.A. and E.O.S. contributed equally to this work. The authors would like to thank Alex Petras for help with proofreading the manuscript and members of the BIRTH Lab for fruitful discussions about several bioinspired soft actuators and sensors incorporated in this paper.

## Conflict of Interest

The authors declare no conflict of interest.

## Keywords

bioinspired actuators, bioinspired robotics, bioinspired sensors, soft materials, soft robotics

Received: May 9, 2020
Revised: August 15, 2020
Published online:

[1] A. Al-Ibadi, S. Nefti-Meziani, S. Davis, *Robotics* **2018**, *7*, 19.
[2] T. Manwell, B. Guo, J. Back, H. Liu, in *2018 IEEE Int. Conf. on Soft Robotics*, IEEE, Livorno, Italy **2018**, pp. 54–59.
[3] R. Xie, M. Su, Y. Zhang, M. Li, H. Zhu, Y. Guan, in *2018 IEEE Int. Conf. on Robotics and Automation*, IEEE, Brisbane, Australia **2018**, pp. 3448–3453.
[4] W. Coral, C. Rossi, O. M. Curet, D. Castro, *Bioinspir. Biomim.* **2018**, *13*, 056009.
[5] J. Fras, Y. Noh, M. Macias, H. Wurdemann, K. Althoefer, in *2018 IEEE Int. Conf. on Robotics and Automation*, IEEE, Brisbane, Australia **2018**, pp. 1583–1588.
[6] J. Frame, N. Lopez, O. Curet, E. D. Engeberg, *Bioinspir. Biomim.* **2018**, *13*, 064001.
[7] D. Rus, M. T. Tolley, *Nature* **2015**, *521*, 467.
[8] Z. Peng, J. Huang, *Appl. Sci.* **2019**, *9*, 3102.
[9] H.-R. Lim, H. S. Kim, R. Qazi, Y.-T. Kwon, J.-W. Jeong, W.-H. Yeo, *Adv. Mater.* **2019**, 1901924.
[10] C. Walsh, *Nat. Rev. Mater.* **2018**, *3*, 78.
[11] E. W. Hawkes, L. H. Blumenschein, J. D. Greer, A. M. Okamura, *Sci. Rob.* **2017**, *2*, 8.
[12] R. K. Katzschmann, J. DelPreto, R. MacCurdy, D. Rus, *Sci. Rob.* **2018**, *3*, 16.
[13] J. Luong, P. Glick, A. Ong, M. S. deVries, S. Sandin, E. W. Hawkes, M. T. Tolley, in *2019 2nd IEEE Int. Conf. on Soft Robotics*, IEEE, Seoul, South Korea **2019**, pp. 801–807.
[14] Y. Chen, H. Zhao, J. Mao, P. Chirarattananon, E. F. Helbling, N.-s. P. Hyun, D. R. Clarke, R. J. Wood, *Nature* **2019**, *575*, 324.
[15] M. Stoppa, A. Chiolerio, *Sensors* **2014**, *14*, 11957.
[16] S. Gong, W. Cheng, *Adv. Electron. Mater.* **2017**, *3*, 1600314.
[17] R. A. Bilodeau, R. K. Kramer, *Front. Robot. AI* **2017**, *4*, 48.
[18] M. T. Tolley, R. F. Shepherd, B. Mosadegh, K. C. Galloway, M. Wehner, M. Karpelson, R. J. Wood, G. M. Whitesides, *Soft Rob.* **2014**, *1*, 213.
[19] S. Terryn, J. Brancart, D. Lefeber, G. Van Assche, B. Vanderborght, *Sci. Robot* **2017**, *2*, 1.
[20] E. Acome, S. Mitchell, T. Morrissey, M. Emmett, C. Benjamin, M. King, M. Radakovitz, C. Keplinger, *Science* **2018**, *359*, 61.
[21] D. L. Taylor, M. in het Panhuis, *Adv. Mater.* **2016**, *28*, 9060.
[22] B. C. Tee, C. Wang, R. Allen, Z. Bao, *Nat. Nanotechnol.* **2012**, *7*, 825.
[23] Y. Morimoto, H. Onoe, S. Takeuchi, *Sci. Rob.* **2018**, *3*, 18.
[24] C. Cvetkovic, M. C. Ferrall-Fairbanks, E. Ko, L. Grant, H. Kong, M. O. Platt, R. Bashir, *Sci. Rep.* **2017**, *7*, 3775.
[25] A. L. Duigou, S. Requile, J. Beaugrand, F. Scarpa, M. Castro, *Smart Mater. Struct.* **2017**, *26*, 125009.
[26] Y. Ge, R. Cao, S. Ye, Z. Chen, Z. Zhu, Y. Tu, D. Ge, X. Yang, *Chem. Commun.* **2018**, *54*, 3126.
[27] Y. Sun, Y. Wang, C. Hua, Y. Ge, S. Hou, Y. Shang, A. Cao, *Carbon* **2018**, *132*, 394.
[28] H. Jiang, Y. Liu, J. Liu, S. Li, Y. Song, D. Han, L. Ren, *Front. Chem.* **2019**, *7*, 464.
[29] Y. Zhang, H. Jiang, F. Li, Y. Xia, Y. Lei, X. Jin, G. Zhang, H. Li, *J. Mater. Chem. A* **2017**, *5*, 14604.
[30] D.-D. Han, Y.-L. Zhang, Y. Liu, Y.-Q. Liu, H.-B. Jiang, B. Han, X.-Y. Fu, H. Ding, H.-L. Xu, H.-B. Sun, *Adv. Funct. Mater.* **2015**, *25*, 4548.
[31] J.-W. Mao, Z.-D. Chen, D.-D. Han, J.-N. Ma, Y.-L. Zhang, H.-B. Sun, *Nanoscale* **2019**, *11*, 20614.
[32] H. Wang, H. Luo, H. Zhou, X. Zhou, X. Zhang, W. Lin, G. Yi, Y. Zhang, *Chem. Eng. J.* **2018**, *345*, 452.
[33] R. Zhang, C. Ying, H. Gao, Q. Liu, X. Fu, S. Hu, *Compos. Sci. Technol.* **2019**, *171*, 218.
[34] M. A. Haq, Y. Su, D. Wang, *Mater. Sci. Eng., C* **2017**, *70*, 842.
[35] T. H. Kim, J. G. Choi, J. Y. Byun, Y. Jang, S. M. Kim, G. M. Spinks, S. J. Kim, *Sci. Rep.* **2019**, *9*, 1.
[36] C. Ohm, M. Brehmer, R. Zentel, *Adv. Mater.* **2010**, *22*, 3366.
[37] N. Wang, C. Cui, H. Guo, B. Chen, X. Zhang, *Sci. China Technol. Sci.* **2018**, *61*, 1512.
[38] Z. Chen, X. Tan, *IEEE/ASME Trans. Mechatron.* **2008**, *13*, 519.
[39] L. Hines, K. Petersen, G. Z. Lum, M. Sitti, *Adv. Mater.* **2017**, *29*, 1603483.
[40] R. Hernández, A. Sarafian, D. López, C. Mijangos, *Polymer* **2004**, *45*, 5543.
[41] J.-U. Lee, D. Yoon, H. Cheong, *Nano Lett.* **2012**, *12*, 4444.
[42] L. J. Romasanta, M. A. López-Manchado, R. Verdejo, *Prog. Polym. Sci.* **2015**, *51*, 188.
[43] M. V. Vaganov, D. Y. Borin, S. Odenbach, Y. L. Raikher, *Soft Matter* **2019**, *15*, 4947.
[44] M. D. Bartlett, N. Kazem, M. J. Powell-Palm, X. Huang, W. Sun, J. A. Malen, C. Majidi, *Proc. Natl. Acad. Sci.* **2017**, *114*, 2143.
[45] E. Biddiss, T. Chau, *Med. Eng. Phys.* **2008**, *30*, 403.
[46] J. Zhou, R. N. Miles, *Proc. Natl. Acad. Sci.* **2017**, *114*, 12120.

[47] C. M. Donatelli, S. A. Bradner, J. Mathews, E. Sanders, C. Culligan, D. Kaplan, E. D. Tytell, in *2018 IEEE Int. Conf. on Soft Robotics*, IEEE, Livorno, Italy **2018**, pp. 60–65.
[48] G. Selvolini, I. Băjan, O. Hosu, C. Cristea, R. Săndulescu, G. Marrazza, *Sensors* **2018**, *18*, 7.
[49] P. Pataranutaporn, J. S. De La Vega, A. Chowdhury, A. Ng, G. Mihaleva, in *2018 Int. Flexible Electronics Technology Conf.*, Ottawa, Canada, **2018**, pp. 1–4.
[50] Q. Zhu, Y. Jin, W. Wang, G. Sun, D. Wang, *ACS Appl. Mater. Interfaces* **2019**, *11*, 1440.
[51] T. Wu, J. Li, J. Li, S. Ye, J. Wei, J. Guo, *J. Mater. Chem. C* **2016**, *4*, 9687.
[52] L. Zong, M. Li, C. Li, *Adv. Mater.* **2017**, *29*, 1604691.
[53] T. Patino, R. Mestre, S. Sanchez, *Lab Chip* **2016**, *16*, 3626.
[54] C. Cvetkovic, R. Raman, V. Chan, B. J. Williams, M. Tolish, P. Bajaj, M. S. Sakar, H. H. Asada, M. T. A. Saif, R. Bashir, *Proc. Natl. Acad. Sci.* **2014**, *111*, 10125.
[55] R. Raman, C. Cvetkovic, S. G. Uzel, R. J. Platt, P. Sengupta, R. D. Kamm, R. Bashir, *Proc. Natl. Acad. Sci.* **2016**, *113*, 3497.
[56] S.-J. Park, M. Gazzola, K. S. Park, S. Park, V. Di Santo, E. L. Blevins, J. U. Lind, P. H. Campbell, S. Dauth, A. K. Capulli, F. S. Pasqualini, S. Ahn, A. Cho, H. Yuan, B. M. Maoz, R. Vijaykumar, J.-W. Choi, K. Deisseroth, G. V. Lauder, L. Mahadevan, K. Kit Parker, *Science* **2016**, *353*, 158.
[57] S. R. Shin, B. Migliori, B. Miccoli, Y.-C. Li, P. Mostafalu, J. Seo, S. Mandla, A. Enrico, S. Antona, R. Sabarish, T. Zheng, L. Pirrami, K. Zhang, Y. S. Zhang, K.-t. Wan, D. Demarchi, M. R. Dokmeci, A. Khademhosseini, *Adv. Mater.* **2018**, *30*, 1704189.
[58] R. Mestre, T. Patiño, X. Barceló, S. Anand, A. Pérez-Jiménez, S. Sánchez, *Adv. Mater. Technol.* **2019**, *4*, 1800631.
[59] R. W. Carlsen, M. Sitti, *Small* **2014**, *10*, 3831.
[60] S. Réquilé, A. Le Duigou, A. Bourmaud, C. Baley, *Composites, Part A* **2019**, *123*, 278.
[61] A. Le Duigou, S. Requile, J. Beaugrand, F. Scarpa, M. Castro, *Smart Mater. Struct.* **2017**, *26*, 125009.
[62] A. Le Duigou, M. Castro, *Ind. Crops Prod.* **2017**, *99*, 142.
[63] R. Pugliese, F. Gelain, *Mater. Des.* **2020**, *186*, 108370.
[64] L. Jiang, Y. Wang, S. Wen, Y. Zhou, J. Ma, S. Chen, S. Jerrams, *Mater. Des.* **2020**, *192*, 108674.
[65] D. Li, R. B. Kaner, *Science* **2008**, *320*, 1170.
[66] O. C. Compton, S. T. Nguyen, *Small* **2010**, *6*, 711.
[67] Y. Hu, K. Qi, L. Chang, J. Liu, L. Yang, M. Huang, G. Wu, P. Lu, W. Chen, Y. Wu, *J. Mater. Chem. C* **2019**, *7*, 6879.
[68] J. He, P. Xiao, J. Shi, Y. Liang, W. Lu, Y. Chen, W. Wang, P. Théato, S.-W. Kuo, T. Chen, *Chem. Mater.* **2018**, *30*, 4343.
[69] K. Ojha, O. Anjaneyulu, A. Ganguli, *Curr. Sci.* **2014**, *107*, 397.
[70] J. H. Lee, D. W. Shin, V. G. Makotchenko, A. S. Nazarov, V. E. Fedorov, Y. H. Kim, J.-Y. Choi, J. M. Kim, J.-B. Yoo, *Adv. Mater.* **2009**, *21*, 4383.
[71] Y.-Y. Gao, B. Han, W.-Y. Zhao, Z.-C. Ma, Y.-S. Yu, H.-B. Sun, *Front. Chem.* **2019**, *7*.
[72] Y. Yang, M. Zhang, D. Li, Y. Shen, *Adv. Mater. Technol.* **2019**, *4*, 1800366.
[73] L. Zhang, J. Pan, Y. Liu, Y. Xu, A. Zhang, *ACS Appl. Mater. Interfaces* **2020**.
[74] M. Ji, N. Jiang, J. Chang, J. Sun, *Adv. Funct. Mater.* **2014**, *24*, 5412.
[75] L. Wang, Y. Liu, Y. Cheng, X. Cui, H. Lian, Y. Liang, F. Chen, H. Wang, W. Guo, H. Li, M. Zhu, H. Ihara, *Adv. Sci.* **2015**, *2*, 1500084.
[76] B. Han, Y.-L. Zhang, L. Zhu, Y. Li, Z.-C. Ma, Y.-Q. Liu, X.-L. Zhang, X.-W. Cao, Q.-D. Chen, C.-W. Qiu, H.-B. Sun, *Adv. Mater.* **2019**, *31*, 1806386.
[77] Y. Hu, G. Wu, T. Lan, J. Zhao, Y. Liu, W. Chen, *Adv. Mater.* **2015**, *27*, 7867.
[78] E. Wang, M. S. Desai, S.-W. Lee, *Nano Lett.* **2013**, *13*, 2826.
[79] Y. Huang, J. Liang, Y. Chen, *J. Mater. Chem.* **2012**, *22*, 3671.
[80] M. C. Catoira, L. Fusaro, D. Di Francesco, M. Ramella, F. Boccafoschi, *J. Mater. Sci.: Mater. Med.* **2019**, *30*, 115.
[81] E. M. Ahmed, *J. Adv. Res.* **2015**, *6*, 105.
[82] L. Ionov, *Mater. Today* **2014**, *17*, 494.
[83] S. Wu, B. Duan, X. Qin, J. T. Butcher, *Acta Biomater.* **2017**, *60*, 144.
[84] R. Luo, J. Wu, N.-D. Dinh, C.-H. Chen, *Adv. Funct. Mater.* **2015**, *25*, 7272.
[85] Y. Zhou, C. Wan, Y. Yang, H. Yang, S. Wang, Z. Dai, K. Ji, H. Jiang, X. Chen, Y. Long, *Adv. Funct. Mater.* **2019**, *29*, 1806220.
[86] S. Xue, Y. Wu, J. Wang, M. Guo, D. Liu, W. Lei, *Materials* **2018**, *11*, 29937530.
[87] S. Chatterjee, P. Hui, C.-w. Kan, *Polymers* **2018**, *10*, 480.
[88] M. Sasaki, B. C. Karikkineth, K. Nagamine, H. Kaji, K. Torimitsu, M. Nishizawa, *Adv. Healthc. Mater.* **2014**, *3*, 1919.
[89] T. J. White, *J. Polym. Sci., Part B* **2018**, *56*, 695.
[90] R. Yang, Y. Zhao, *Angew. Chem., Int. Ed.* **2017**, *56*, 14202.
[91] Y. Yu, T. Ikeda, *Angew. Chem., Int. Ed.* **2006**, *45*, 5416.
[92] H. Jiang, C. Li, X. Huang, *Nanoscale* **2013**, *5*, 23648966.
[93] M. Warner, E. Terentjev, *Liquid Crystal Elastomers*, Oxford University Press, Oxford, England **2003**.
[94] R. R. Kohlmeyer, J. Chen, *Angew. Chem., Int. Ed.* **2013**, *52*, 9234.
[95] T. J. White, D. J. Broer, *Nat. Mater.* **2015**, *14*, 1087.
[96] H. Kim, Liquid Crystal Elastomers for Actuators and Electronics. Diss. **2019**.
[97] S. J. Dünki, Y. S. Ko, F. A. Nüesch, D. M. Opris, *Adv. Funct. Mater.* **2015**, *25*, 2467.
[98] F. Carpi, D. De Rossi, R. Kornbluh, R. E. Pelrine, P. Sommer-Larsen, *Dielectric Elastomers as Electromechanical Transducers: Fundamentals, Materials, Devices, Models and Applications of an Emerging Electroactive Polymer Technology*, Elsevier, New York **2009**.
[99] K. B. Subramani, E. Cakmak, R. J. Spontak, T. K. Ghosh, *Adv. Mater.* **2014**, *26*, 2949.
[100] N. Mathews, Novel material composites for dielectric elastomer actuators. Diss. **2019**.
[101] Y. Wang, U. Gupta, J. Zhu, P. Li, D. Du, L. Zhang, J. Ouyang, J. Liu, C. C. Foo, in *2019 IEEE Int. Conf. on Robotics and Biomimetics*, IEEE, Dali, China **2019**, pp. 1959–1964.
[102] M. Zhang, G. Li, X. Yang, Y. Xiao, T. Yang, T.-W. Wong, T. Li, *Smart Mater. Struct.* **2018**, *27*, 095016.
[103] J.-H. Choi, J. Ahn, J.-B. Kim, Y.-C. Kim, J.-Y. Lee, I.-K. Oh, *Small* **2016**, *12*, 1840.
[104] S. Nemat-Nasser, C. Thomas, *Ionomeric Polymer–Metal Composites*, **2001**.
[105] U. Deole, R. Lumia, M. Shahinpoor, M. Bermudez, *J. Micro-Nano Mechatron.* **2008**, *4*, 95.
[106] M. Hao, Y. Wang, Z. Zhu, Q. He, D. Zhu, M. Luo, *Front. Robot. AI* **2019**, *6*, 129.
[107] J. H. Lee, J. H. Lee, J.-D. Nam, H. Choi, K. Jung, J. W. Jeon, Y. K. Lee, K. J. Kim, Y. Tak, *Sens. Actuators, A* **2005**, *118*, 98.
[108] Q. Shen, S. Trabia, T. Stalbaum, V. Palmre, K. Kim, I.-K. Oh, *Sci. Rep.* **2016**, *6*, 24462.
[109] J. D. Carrico, T. Hermans, K. J. Kim, K. K. Leang, *Sci. Rep.* **2019**, *9*, 17482.
[110] M. Shahinpoor, K. J. Kim, D. J. Leo, *Polym. Compos.* **2003**, *24*, 24.
[111] K. Kim, M. Shahinpoor, *Proc. SPIE* **2001**.
[112] K. J. Kim, S. Tadokoro, *Electroactive Polymers for Robotics Applications: Artificial Muscle and Sensors*, Springer, New York **2007**.
[113] I. Must, F. Kaasik, I. Põldsalu, L. Mihkels, U. Johanson, A. Punning, A. Aabloo, *Adv. Eng. Mater.* **2015**, *17*, 84.
[114] K. Junius, M. Moltedo, P. Cherelle, C. Rodriguez-Guerrero, B. Vanderborght, D. Lefeber, *Bioinspir. Biomim.* **2017**, *12*, 061001.
[115] D. Scaradozzi, G. Palmieri, D. Costa, A. Pinelli, *Ocean Eng.* **2017**, *130*, 437.

[116] H. Yousef, M. Boukallel, K. Althoefer, *Sens. Actuators, A* **2011**, *167*, 171.

[117] P. K. Singh, C. M. Krishna, *Univer. J. Mech. Eng.* **2014**, *2*, 193.

[118] I. D. Walker, *ISRN Robot.* **2013**, *2013*.

[119] E. Mattar, *Robot. Auton. Syst.* **2013**, *61*, 517.

[120] J. Yuan, S. K. Cho, *J. Mech. Sci. Technol.* **2012**, *26*, 3761.

[121] S. Li, K. Wang, *Bioinspir. Biomim.* **2016**, *12*, 011001.

[122] J. Hughes, U. Culha, F. Giardina, F. Guenther, A. Rosendo, F. Iida, *Front. Robot. AI* **2016**, *3*, 69.

[123] C. Lee, M. Kim, Y. J. Kim, N. Hong, S. Ryu, H. J. Kim, S. Kim, *Int. J. Control Autom.* **2017**, *15*, 3.

[124] M. Manti, V. Cacucciolo, M. Cianchetti, *IEEE Robot. Autom. Mag.* **2016**, *23*, 93.

[125] C. Dawson, J. F. Vincent, A.-M. Rocca, *Nature* **1997**, *390*, 668.

[126] I. Must, E. Sinibaldi, B. Mazzolai, *Nat. Commun.* **2019**, *10*, 1.

[127] R. Elbaum, L. Zaltzman, I. Burgert, P. Fratzl, *Science* **2007**, *316*, 884.

[128] R. Pfeifer, M. Lungarella, F. Iida, *science* **2007**, *318*, 1088.

[129] A. Miriyev, *MDPI* **2019**, *8*, 74.

[130] H. Cui, Q. Zhao, Y. Wang, X. Du, *Chem. - Asian J.* **2019**, *14*, 2369.

[131] S. Coyle, C. Majidi, P. LeDuc, K. J. Hsia, *Extreme Mech. Lett.* **2018**, *22*, 51.

[132] H. Ko, A. Javey, *Acc. Chem. Res.* **2017**, *50*, 691.

[133] S. J. Kim, H. I. Kim, S. J. Park, I. Y. Kim, S. H. Lee, T. S. Lee, S. I. Kim, *Smart Mater. Struct.* **2005**, *14*, 511.

[134] Y. Shang, J. Wang, T. Ikeda, L. Jiang, *J. Mater. Chem. C* **2019**, *7*, 3413.

[135] F. Carpi, R. Kornbluh, P. Sommer-Larsen, G. Alici, *Bioinspir. Biomim.* **2011**, *6*, 045006.

[136] Y. Bahramzadeh, M. Shahinpoor, *Soft Rob.* **2014**, *1*, 38.

[137] M. Cianchetti, A. Licofonte, M. Follador, F. Rogai, C. Laschi, *MDPI* **2014**, *3*, 226.

[138] L. Yao, H. Ishii, in *Robotic Systems and Autonomous Platforms* (Eds: M. Strano, S. M. Walsh), Elsevier, New York **2019**, pp. 41–57.

[139] M. Rüggeberg, I. Burgert, *PloS one* **2015**, *10*, 4.

[140] E. Reyssat, L. Mahadevan, *J. R. Soc., Interface* **2009**, *6*, 951.

[141] R. Liu, T. Gong, K. Zhang, C. Lee, *Sci. Rep.* **2017**, *7*, 1.

[142] M. Wang, X. Tian, R. H. Ras, O. Ikkala, *Adv. Mater. Interfaces* **2015**, *2*, 1500080.

[143] H.-L. Gao, S.-M. Chen, L.-B. Mao, Z.-Q. Song, H.-B. Yao, H. Cölfen, X.-S. Luo, F. Zhang, Z. Pan, Y.-F. Meng, Y. Ni, S.-H. Yu, *Nat. Commun.* **2017**, *8*, 1.

[144] J. Peng, Q. Cheng, *ChemPhysChem* **2018**, *19*, 1980.

[145] L. Zhang, Y. Zhang, F. Li, S. Yan, Z. Wang, L. Fan, G. Zhang, H. Li, *ACS Appl. Mater. Interfaces* **2019**, *11*, 12890.

[146] C. x. Xiang, W. Wang, Q. Zhu, D. Xue, X. Zhao, M. Li, D. Wang, *ACS Appl. Mater. Interfaces* **2019**.

[147] S. H. Kim, C. H. Kwon, K. Park, T. J. Mun, X. Lepró, R. H. Baughman, G. M. Spinks, S. J. Kim, *Sci. Rep.* **2016**, *6*, 1.

[148] T. Jia, Y. Wang, Y. Dou, Y. Li, M. Jung de Andrade, R. Wang, S. Fang, J. Li, Z. Yu, R. Qiao, Z. Liu, Y. Cheng, Y. Su, M. Minary-Jolandan, R. H. Baughman, D. Qian, Z. Liu, *Adv. Funct. Mater.* **2019**, *29*, 1808241.

[149] W. Wang, C. Xiang, Q. Liu, M. Li, W. Zhong, K. Yan, D. Wang, *J. Mater. Chem. A* **2018**, *6*, 22599.

[150] Q. Chen, X. Yan, H. Lu, N. Zhang, M. Ma, *ACS Appl. Mater. Interfaces* **2019**, *11*, 20473.

[151] A. Le Duigou, V. Keryvin, J. Beaugrand, M. Pernes, F. Scarpa, M. Castro, *Composites, Part A* **2019**, *116*, 36.

[152] B. Shin, J. Ha, M. Lee, K. Park, G. H. Park, T. H. Choi, K.-J. Cho, H.-Y. Kim, *Sci. Rob.* **2018**, *3*, 14.

[153] T. Qu, H. Zang, Y. Dai, D. Liu, B. Liao, in *2019 WRC Symp. on Advanced Robotics and Automation*, IEEE, Beijing, China **2019**, pp. 235–241.

[154] S. Poppinga, C. Zollfrank, O. Prucker, J. Rühe, A. Menges, T. Cheng, T. Speck, *Adv. Mater.* **2018**, *30*, 1703653.

[155] J. Kopeček, J. Yang, *Polym. Int.* **2007**, *56*, 1078.

[156] Q. Zhu, Y. Jin, W. Wang, G. Sun, D. Wang, *ACS Appl. Mater. Interfaces* **2018**, *11*, 1440.

[157] H. Tan, X. Yu, Y. Tu, L. Zhang, *J. Phys. Chem. Lett.* **2019**, *10*, 5542.

[158] G. Fotie, R. Rampazzo, M. A. Ortenzi, S. Checchia, D. Fessas, L. Piergiovanni, *Polymers* **2017**, *9*, 415.

[159] M. Ma, L. Guo, D. G. Anderson, R. Langer, *Science* **2013**, *339*, 186.

[160] L. D. Zarzar, P. Kim, J. Aizenberg, *Adv. Mater.* **2011**, *23*, 1442.

[161] S. Riedel, B. Heyart, K. S. Apel, S. G. Mayr, *Sci. Rep.* **2017**, *7*, 1.

[162] V. Kan, E. Vargo, N. Machover, H. Ishii, S. Pan, W. Chen, Y. Kakehi, in *Proc. of the 2017 CHI Conf. on Human Factors in Computing Systems*, Denver, CO **2017**, pp. 989–1000.

[163] G. Kocak, C. Tuncer, V. Bütün, *Polym. Chem.* **2017**, *8*, 144.

[164] R. B. Vasani, E. J. Szili, G. Rajeev, N. H. Voelcker, *Chem. - Asian J.* **2017**, *12*, 1605.

[165] A. M. Atta, A. O. Ezzat, H. A. Al-Lohedan, A. M. Tawfeek, A. A. Alobaidi, *Nanomaterials* **2019**, *9*, 1693.

[166] N. Koseva, V. Mitova, Z. Todorova, I. Tsacheva, in *Polymeric Nanomaterials in Nanotherapeutics* (Ed: C. Vasile), Elsevier, New York **2019**, pp. 183–233.

[167] H. Peng, X. Ning, G. Wei, S. Wang, G. Dai, A. Ju, *Carbohydr. Polym.* **2018**, *195*, 349.

[168] C. Yang, F. Su, Y. Liang, W. Xu, S. Li, E. Liang, G. Wang, N. Zhou, Q. Wan, X. Ma, *Soft Matter* **2020**, *16*, 2928.

[169] Y. Cheng, K. Ren, D. Yang, J. Wei, *Sens. Actuators, B* **2018**, *255*, 3117.

[170] X. Li, X. Cai, Y. Gao, M. J. Serpe, *J. Mater. Chem. B* **2017**, *5*, 2804.

[171] M. F. Mutalabisin, B. Chatterjee, J. M. Jaffri, *Res. J. Pharm. Technol.* **2018**, *11*, 5115.

[172] J. Duan, X. Liang, K. Zhu, J. Guo, L. Zhang, *Soft Matter* **2017**, *13*, 345.

[173] H. Shahsavan, S. M. Salili, A. Jákli, B. Zhao, *Adv. Mater.* **2017**, *29*, 1604021.

[174] S. Jiang, F. Liu, A. Lerch, L. Ionov, S. Agarwal, *Adv. Mater.* **2015**, *27*, 4865.

[175] L. Dong, Y. Zhao, *Mater. Chem. Front.* **2018**, *2*, 1932.

[176] Y. Cui, Y. Yin, C. Wang, K. Sim, Y. Li, C. Yu, J. Song, *Appl. Math. Mech.* **2019**, *40*, 943.

[177] Y. Zhang, Z. Wang, Y. Yang, Q. Chen, X. Qian, Y. Wu, H. Liang, Y. Xu, Y. Wei, Y. Ji, *Sci. Adv.* **2020**, *6*, eaay8606.

[178] Y. Wu, Y. Yang, Q. Chen, X. Qian, Y. Wei, Y. Ji, *Angew. Chem., Int. Ed.* **2020**.

[179] J. Wang, L. Lin, Q. Cheng, L. Jiang, *Angew. Chem., Int. Ed.* **2012**, *51*, 4676.

[180] H. Lin, S. Ma, B. Yu, M. Cai, Z. Zheng, F. Zhou, W. Liu, *Chem. Mater.* **2019**, *31*, 4469.

[181] X. Yang, G. Li, T. Cheng, Q. Zhao, C. Ma, T. Xie, T. Li, W. Yang, *J. Appl. Mech.* **2016**, *83*, 7.

[182] H. Warren, M. in het Panhuis, G. M. Spinks, D. L. Officer, *J. Polym. Sci., Part B: Polym. Phys.* **2018**, *56*, 46.

[183] J. Zheng, P. Xiao, X. Le, W. Lu, P. Théato, C. Ma, B. Du, J. Zhang, Y. Huang, T. Chen, *J. Mater. Chem. C* **2018**, *6*, 1320.

[184] R. Göstl, A. Senf, S. Hecht, *Chem. Soc. Rev.* **2014**, *43*, 1982.

[185] S. J. Aßhoff, F. Lancia, S. Iamsaard, B. Matt, T. Kudernac, S. P. Fletcher, N. Katsonis, *Angew. Chem., Int. Ed.* **2017**, *56*, 3261.

[186] Leeladhar, P. Raturi, J. Singh, *Sci. Rep.* **2018**, *8*, 1.

[187] H. Shahsavan, A. Aghakhani, H. Zeng, Y. Guo, Z. S. Davidson, A. Priimagi, M. Sitti, *Proc. Natl. Acad. Sci.* **2020**, *117*, 5125.

[188] X. Xiong, A. del Campo, J. Cui, in *Smart Polymers and their Applications* (Ed: M. R. Aguilar), Elsevier, New York **2019**, pp. 87–153.

[189] K. Upadhyay, S. Thomas, R. K. Tamrakar, N. Kalarikkal, in *Advanced Functional Polymers for Biomedical Applications* (Eds: M. Mozafari, N. P. S. Chauhan), Elsevier, **2019**, pp. 211–233.

[190] E. Kizilkan, J. Strueben, A. Staubitz, S. N. Gorb, *Sci. Robot* **2017**, *2*, 2.

[191] S. Iamsaard, S. J. Aßhoff, B. Matt, T. Kudernac, J. J. Cornelissen, S. P. Fletcher, N. Katsonis, *Nat. Chem.* **2014**, *6*, 229.

[192] W. Wang, C. Xiang, Q. Zhu, W. Zhong, M. Li, K. Yan, D. Wang, *ACS Appl. Mater. Interfaces* **2018**, *10*, 27215.
[193] X. Wang, B. Yang, D. Tan, Q. Li, B. Song, Z.-S. Wu, A. del Campo, M. Kappl, Z. Wang, S. N. Gorb, S. Liu, L. Xue, *Mater. Today* **2020**, *35*, 42.
[194] Y. Yang, D. Li, Y. Shen, *IEEE Robot. Autom. Lett.* **2019**, *4*, 1647.
[195] C. Ahn, X. Liang, S. Cai, *Adv. Mater. Technol.* **2019**, *4*, 1900185.
[196] H. Zeng, O. M. Wani, P. Wasylczyk, A. Priimagi, *Macromol. Rapid Commun.* **2018**, *39*, 1700224.
[197] M. Rogóż, H. Zeng, C. Xuan, D. S. Wiersma, P. Wasylczyk, *Adv. Opt. Mater.* **2016**, *4*, 1689.
[198] M. Rogóż, K. Dradrach, C. Xuan, P. Wasylczyk, *Macromol. Rapid Commun.* **2019**, *40*, 1900279.
[199] H. Yang, W. R. Leow, T. Wang, J. Wang, J. Yu, K. He, D. Qi, C. Wan, X. Chen, *Adv. Mater.* **2017**, *29*, 1701627.
[200] A. Nishiguchi, H. Zhang, S. Schweizerhof, M. F. Schulte, A. Mourran, M. Moeller, *ACS Appl. Mater. Interfaces* **2020**, *12*, 12176.
[201] A. S. Kuenstler, R. C. Hayward, *Curr. Opin. Colloid Interface Sci.* **2019**.
[202] G. A. Sotiriou, C. O. Blattmann, S. E. Pratsinis, *Adv. Funct. Mater.* **2013**, *23*, 34.
[203] A. S. Ahmed, R. Ramanujan, in *Bioinspiration, Biomimetics, and Bioreplication 2014*, International Society for Optics and Photonics, Long Beach, CA **2014**.
[204] S. Reinicke, S. Döhler, S. Tea, M. Krekhova, R. Messing, A. M. Schmidt, H. Schmalz, *Soft Matter* **2010**, *6*, 2760.
[205] Y. L. Raikher, O. Stolbov, G. Stepanov, *J. Phys. D: Appl. Phys.* **2008**, *41*, 152002.
[206] J. Tang, Z. Tong, Y. Xia, M. Liu, Z. Lv, Y. Gao, T. Lu, S. Xie, Y. Pei, D. Fang, T. J. Wang, *J. Mater. Chem. B* **2018**, *6*, 2713.
[207] S. Khaderi, J. Hussong, J. Westerweel, J. den Toonder, P. Onck, *RSC Adv.* **2013**, *3*, 12735.
[208] S. Zhang, Y. Wang, R. Lavrijsen, P. R. Onck, J. M. den Toonder, *Sens. Actuators, B* **2018**, *263*, 614.
[209] P. Liu, Y. Zhang, S. Liu, Y. Zhang, Z. Du, L. Qu, *Appl. Clay Sci.* **2019**, *172*, 19.
[210] W. Jiang, L. Wang, G. Ye, B. Chen, L. Yin, Y. Shi, H. Liu, *J. Mater. Sci.: Mater. Electron.* **2019**, *30*, 3767.
[211] M. Ilami, R. J. Ahmed, A. Petras, B. Beigzadeh, H. Marvi, *Sci. Rep.* **2020**, *10*, 11.
[212] G. Z. Lum, Z. Ye, X. Dong, H. Marvi, O. Erin, W. Hu, M. Sitti, *Proc. Natl. Acad. Sci.* **2016**, *113*, E6007.
[213] Z. Ren, W. Hu, X. Dong, M. Sitti, *Nat. Commun.* **2019**, *10*, 1.
[214] L. Wang, M. Zhang, W. Shi, Y. Hou, C. Liu, S. Feng, Z. Guo, Y. Zheng, *Sci. Rep.* **2015**, *5*, 11209.
[215] E. B. Joyee, Y. Pan, *Soft Rob.* **2019**, *6*, 333.
[216] J. Ali, U. K. Cheang, J. D. Martindale, M. Jabbarzadeh, H. C. Fu, M. J. Kim, *Sci. Rep.* **2017**, *7*, 1.
[217] S. Ben, J. Yao, Y. Ning, Z. Zhao, J. Zha, D. Tian, K. Liu, L. Jiang, *Sci. China: Chem.* **2020**, *63*, 347.
[218] S. Jiang, Y. Hu, H. Wu, Y. Zhang, Y. Zhang, Y. Wang, Y. Zhang, W. Zhu, J. Li, D. Wu, J. Chu, *Adv. Mater.* **2019**, *31*, 1807507.
[219] H. Lu, M. Zhang, Y. Yang, Q. Huang, T. Fukuda, Z. Wang, Y. Shen, *Nat. Commun.* **2018**, *9*, 1.
[220] H. Leon-Rodriguez, V. H. Le, S. Y. Ko, J.-O. Park, S. Park, in *2015 15th Int. Conf. on Control, Automation and Systems*, IEEE, Busan, Korea **2015**, pp. 1833–1838.
[221] M. Ilami, R. J. Ahmed, D. Edwards, E. Thompson, S. Zeinolabedinzadeh, H. Marvi, *ACS omega* **2019**, *4*, 21242.
[222] X. Zhang, F. Wang, Y. Yu, G. Chen, L. Shang, L. Sun, Y. Zhao, *Sci. Bull.* **2019**, *64*, 1110.
[223] L. Shang, Y. Yu, W. Gao, Y. Wang, L. Qu, Z. Zhao, R. Chai, Y. Zhao, *Adv. Funct. Mater.* **2018**, *28*, 1705802.
[224] L. N. Pham, J. J. Abbott, in *2018 IEEE/RSJ Int. Conf. on Intelligent Robots and Systems*, IEEE, Madrid, Spain **2018**, pp. 1783–1788.
[225] Z. Zhang, X. Li, X. Yu, H. Chai, Y. Li, H. Wu, S. Jiang, *Compos. Struct.* **2019**, *229*, 111422.
[226] Z. Zhang, D. Chen, H. Wu, Y. Bao, G. Chai, *Compos. Struct.* **2016**, *135*, 17.
[227] W. Hu, G. Z. Lum, M. Mastrangeli, M. Sitti, *Nature* **2018**, *554*, 81.
[228] V. K. Venkiteswaran, L. F. P. Samaniego, J. Sikorski, S. Misra, *IEEE Robot. Autom. Lett.* **2019**, *4*, 1753.
[229] T. Xu, J. Zhang, M. Salehizadeh, O. Onaizah, E. Diller, *Sci. Rob.* **2019**, *4*, eaav4494.
[230] Y. Dai, D. Chen, S. Liang, L. Song, Q. Qi, L. Feng, in *2019 IEEE Int. Conf. on Robotics and Biomimetics*, IEEE, Dali, China **2019**, pp. 2201–2206.
[231] Y. Kim, H. Yuk, R. Zhao, S. A. Chester, X. Zhao, *Nature* **2018**, *558*, 274.
[232] R. Tognato, A. R. Armiento, V. Bonfrate, R. Levato, J. Malda, M. Alini, D. Eglin, G. Giancane, T. Serra, *Adv. Funct. Mater.* **2019**, *29*, 1804647.
[233] U. K. Cheang, D. Roy, J. H. Lee, M. J. Kim, *Appl. Phys. Lett.* **2010**, *97*, 213704.
[234] I. S. Khalil, H. C. Dijkslag, L. Abelmann, S. Misra, *Appl. Phys. Lett.* **2014**, *104*, 223701.
[235] S. Palagi, E. W. Jager, B. Mazzolai, L. Beccai, *Bioinspir. Biomim.* **2013**, *8*, 046004.
[236] K. Bente, A. Codutti, F. Bachmann, D. Faivre, *Small* **2018**, *14*, 1704374.
[237] F. Ullrich, C. Bergeles, J. Pokki, O. Ergeneman, S. Erni, G. Chatzipirpiridis, S. Pané, C. Framme, B. J. Nelson, *Invest. Ophthalmol. Visual Sci.* **2013**, *54*, 2853.
[238] H. Ceylan, I. C. Yasa, O. Yasa, A. F. Tabak, J. Giltinan, M. Sitti, *BioRxiv* **2018**, 379024.
[239] M.-Y. Choi, Y. Shin, H. S. Lee, S. Y. Kim, J.-H. Na, *Sci. Rep.* **2020**, *10*, 1.
[240] C. Christianson, C. Bayag, G. Li, S. Jadhav, A. Giri, C. Agba, T. Li, M. T. Tolley, *Front. Robot. AI* **2019**, *6*, 126.
[241] C. Wang, K. Sim, J. Chen, H. Kim, Z. Rao, Y. Li, W. Chen, J. Song, R. Verduzco, C. Yu, *Adv. Mater.* **2018**, *30*, 1706695.
[242] S. Ma, Y. Zhang, Y. Liang, L. Ren, W. Tian, L. Ren, *Adv. Funct. Mater.* **2020**, *30*, 1908508.
[243] X. Zhou, S. Bi, *Bioinspir. Biomim.* **2012**, *7*, 041001.
[244] K. Kaneko, K. Harada, F. Kanehiro, G. Miyamori, K. Akachi, in *2008 IEEE/RSJ Int. Conf. on Intelligent Robots and Systems*, IEEE, Nice, France **2008**, pp. 2471–2478.
[245] B. Beigzadeh, M. Ilami, S. Najafian, in *2015 3rd RSI Int. Conf. on Robotics and Mechatronics*, IEEE, Rome, Italy **2015**223–228.
[246] Y. Bar-Cohen, *SPIE* **2002**, *4695*, 1.
[247] Y. Qiu, E. Zhang, R. Plamthottam, Q. Pei, *Acc. Chem. Res.* **2019**, *52*, 316.
[248] G. Kovacs, L. Düring, S. Michel, G. Terrasi, *Sens. Actuators, A* **2009**, *155*, 299.
[249] G. Haghiashtiani, E. Habtour, S.-H. Park, F. Gardea, M. C. McAlpine, *Extreme Mech. Lett.* **2018**, *21*, 1.
[250] M. Corbaci, W. Walter, K. Lamkin-Kennard, *MDPI* **2018**, *7*, 73.
[251] H. S. Jung, S. Y. Yang, K. H. Cho, M. G. Song, C. T. Nguyen, H. Phung, U. Kim, H. Moon, J. C. Koo, J.-D. Nam, H. R. Choi, *Int. J. Control Autom. Syst.* **2017**, *15*, 25.
[252] Z. Ye, Z. Chen, *IEEE/ASME Trans. Mechatron.* **2019**, *24*, 218.
[253] G.-Y. Gu, U. Gupta, J. Zhu, L.-M. Zhu, X. Zhu, *IEEE Trans. Robot.* **2017**, *33*, 1263.
[254] C. Cao, X. Gao, S. Burgess, A. T. Conn, *Extreme Mech. Lett.* **2020**, *35*, 100619.
[255] C. Cao, X. Gao, A. T. Conn, *Smart Mater. Struct.* **2019**, *28*, 095015.

[256] G.-Y. Gu, J. Zhu, L.-M. Zhu, X. Zhu, *Bioinspir. Biomim.* **2017**, *12*, 011003.
[257] L. Li, H. Godaba, H. Ren, J. Zhu, *IEEE/ASME Trans. Mechatron.* **2019**, *24*, 100.
[258] L. Xu, G. Gu, in *2017 24th Int. Conf. on Mechatronics and Machine Vision in Practice.*, Piscataway, NY, **2017**, pp. 1–3.
[259] E.-F. M. Henke, S. Schlatter, I. A. Anderson, *Soft Rob.* **2017**, *4*, 353.
[260] T. Li, Z. Zou, G. Mao, X. Yang, Y. Liang, C. Li, S. Qu, Z. Suo, W. Yang, *Soft Rob.* **2019**, *6*, 133.
[261] C. T. Nguyen, H. Phung, P. T. Hoang, T. Dat Nguyen, H. Jung, H. Moon, J. C. Koo, H. R. Choi, in *2017 IEEE/RSJ Int. Conf. on Intelligent Robots and Systems*, Vancouver, Canda, **2017**, pp. 6233–6238.
[262] C. T. Nguyen, H. Phung, P. T. Hoang, T. D. Nguyen, H. Jung, H. R. Choi, *J. Mech. Robo.* **2018**, *10*, 6.
[263] J. Cao, L. Qin, J. Liu, Q. Ren, C. C. Foo, H. Wang, H. P. Lee, J. Zhu, *Extreme Mech. Lett.* **2018**, *21*, 9.
[264] M. Duduta, D. R. Clarke, R. J. Wood, in *2017 IEEE Int. Conf. on Robotics and Automation.*, IEEE, Marina Bay Sands, Singapore **2017**, pp. 4346–4351.
[265] W.-B. Li, W.-M. Zhang, H.-X. Zou, Z.-K. Peng, G. Meng, *Smart Mater. Struct.* **2018**, *27*, 115024.
[266] L. Qin, J. Cao, Y. Tang, J. Zhu, *J. Appl. Mech.* **2018**, *85*, 051001.
[267] J. Shintake, V. Cacucciolo, H. Shea, D. Floreano, *Soft Rob.* **2018**, *5*, 466.
[268] Y. Tang, L. Qin, X. Li, C. Chew, J. Zhu, in *2017 IEEE/RSJ Int. Conf. on Intelligent Robots and Systems*, Vancouver, Canada **2017**, pp. 2403–2408.
[269] C. Christianson, N. N. Goldberg, D. D. Deheyn, S. Cai, M. T. Tolley, *Sci. Rob.* **2018**, *3*, eaat1893.
[270] H. Godaba, J. Li, Y. Wang, J. Zhu, *IEEE Robot. Autom. Lett.* **2016**, *1*, 624.
[271] T. Li, G. Li, Y. Liang, T. Cheng, J. Dai, X. Yang, B. Liu, Z. Zeng, Z. Huang, Y. Luo, T. Xie, W. Yang, *Sci. Adv.* **2017**, *3*, 4.
[272] F. Berlinger, M. Duduta, H. Gloria, D. Clarke, R. Nagpal, R. Wood, in *2018 IEEE Int. Conf. on Robotics and Automation*, IEEE, Brisbane, Australia **2018**, pp. 3429–3435.
[273] B. Liu, F. Chen, S. Wang, Z. Fu, T. Cheng, T. Li, *J. Appl. Mech.* **2017**, *84*, 091005.
[274] S. Wang, B. Huang, D. McCoul, M. Li, L. Mu, J. Zhao, *Smart Mater. Struct.* **2019**, *28*, 045006.
[275] N. Sholl, A. Moss, W. M. Kier, K. Mohseni, *Soft Rob.* **2019**, *6*, 356.
[276] G.-K. Lau, Y.-W. Chin, T.-G. La, in *Electroactive Polymer Actuators and Devices 2017*, International Society for Optics and Photonics, Portland, OR **2017**, p. 1016320.
[277] A. T. Conn, J. Rossiter, in *Electroactive Polymer Actuators and Devices 2011*, Int. Society for Optics and Photonics, San Diego, CA **2011**, p. 79761Z.
[278] A. Conn, S. Burgess, C. Ling, R. Vaidyanathan, *Int. J. Des. Nat. Ecodyn.* **2008**, *3*, 12.
[279] S. Petsch, R. Rix, P. Reith, B. Khatri, S. Schuhladen, D. Ruh, R. Zentel, H. Zappe, in *2014 IEEE 27th Int. Conf. on Micro Electro Mechanical Systems*, IEEE, San Francisco, CA **2014**, pp. 905–908.
[280] H. Shahsavan, S. M. Salili, A. Jákli, B. Zhao, *Adv. Mater.* **2017**, *29*, 1604021.
[281] S. Schuhladen, F. Preller, R. Rix, S. Petsch, R. Zentel, H. Zappe, *Adv. Mater.* **2014**, *26*, 7247.
[282] C. Wang, K. Sim, J. Chen, H. Kim, Z. Rao, Y. Li, W. Chen, J. Song, R. Verduzco, C. Yu, *Adv. Mater.* **2018**, *30*, 1706695.
[283] Q. He, Z. Wang, Y. Wang, A. Minori, M. T. Tolley, S. Cai, *Sci. Adv.* **2019**, *5*, 10.
[284] B. Pawlowski, J. Sun, J. Zhao, in *2018 IEEE Conf. on Decision and Control*, IEEE, Miami Beach, FL **2018**, pp. 409–414.
[285] M. J. Ford, C. P. Ambulo, T. A. Kent, E. J. Markvicka, C. Pan, J. Malen, T. H. Ware, C. Majidi, *Proc. Natl. Acad. Sci.* **2019**, *116*, 21438.
[286] F. Michael, M. Palaniswamy, C. P. Ambulo, T. H. Ware, C. Majidi, *Soft Matter* **2020**, *16*, 5878.
[287] T. A. Kent, M. J. Ford, E. J. Markvicka, C. Majidi, *Multifunct. Mater.* **2020**.
[288] C. Lu, Y. Yang, J. Wang, R. Fu, X. Zhao, L. Zhao, Y. Ming, Y. Hu, H. Lin, X. Tao, Y. Li, W. Chen, *Nat. Commun.* **2018**, *9*, 1.
[289] E. Tabatabaie, M. Shahinpoor, *Int. Rob. Auto. J.* **2019**, *5*, 138.
[290] Z. Chen, P. Hou, Z. Ye, in *2018 IEEE/RSJ Int. Conf. on Intelligent Robots and Systems*, IEEE, Vancouver, Canada **2018**, pp. 8146–8151.
[291] X. Yi, Z. Chen, A. Chakravarthy, in *Dynamic Systems and Control Conf.*, vol. 59162, American Society of Mechanical Engineers, Park City, UT **2019**.
[292] L. Chang, L. Yu, C. Li, Q. Niu, Y. Hu, P. Lu, Z. Zhu, Y. Wu, *Smart Mater. Struct.* **2018**, *27*, 105046.
[293] M. Pilz da Cunha, Y. Foelen, R. J. H. van Raak, J. N. Murphy, T. A. P. Engels, M. G. Debije, A. P. H. J. Schenning, *Adv. Opt. Mater.* **2019**, *7*, 1801643.
[294] S. Taccola, F. Greco, E. Sinibaldi, A. Mondini, B. Mazzolai, V. Mattoli, *Adv. Mater.* **2015**, *27*, 1668.
[295] J. Mu, C. Hou, B. Zhu, H. Wang, Y. Li, Q. Zhang, *Sci. Rep.* **2015**, *5*, 1.
[296] Y. Hu, A. Xu, J. Liu, L. Yang, L. Chang, M. Huang, W. Gu, G. Wu, P. Lu, W. Chen, Y. Wu, *Adv. Mater. Technol.* **2019**, *4*, 1800674.
[297] Y. Hu, J. Liu, L. Chang, L. Yang, A. Xu, K. Qi, P. Lu, G. Wu, W. Chen, Y. Wu, *Adv. Funct. Mater.* **2017**, *27*, 1704388.
[298] A. Le Duigou, G. Chabaud, F. Scarpa, M. Castro, *Adv. Funct. Mater.* **2019**, *29*, 1903280.
[299] L. Yang, K. Qi, L. Chang, A. Xu, Y. Hu, H. Zhai, P. Lu, *J. Mater. Chem. B* **2018**, *6*, 5031.
[300] Y. Dong, J. Wang, X. Guo, S. Yang, M. O. Ozen, P. Chen, X. Liu, W. Du, F. Xiao, U. Demirci, B. F. Liu, *Nat. Commun.* **2019**, *10*, 1.
[301] H. Deng, C. Zhang, J.-W. Su, Y. Xie, C. Zhang, J. Lin, *J. Mater. Chem. B* **2018**, *6*, 5415.
[302] T. Kamal, S.-Y. Park, *Chem. Commun.* **2014**, *50*, 2030.
[303] Y. Liu, B. Xu, S. Sun, J. Wei, L. Wu, Y. Yu, *Adv. Mater.* **2017**, *29*, 1604792.
[304] Y. Wang, Q. Guo, G. Su, J. Cao, J. Liu, X. Zhang, *Adv. Funct. Mater.* **2019**, *29*, 1906198.
[305] Y. Sun, M.-K. Kim, M. Wang, J. Yu, S. Y. Hong, J.-D. Nam, L. Ci, J. Suhr, *Carbon* **2020**, *161*, 702.
[306] L. Du, Z.-Y. Xu, C.-L. Huang, F.-Y. Zhao, C.-J. Fan, J. Dai, K.-K. Yang, Y.-Z. Wang, *Appl. Mater. Today* **2020**, *18*, 100463.
[307] L. Xu, H.-Q. Chen, J. Zou, W.-T. Dong, G.-Y. Gu, L.-M. Zhu, X.-Y. Zhu, *Bioinspir. Biomim.* **2017**, *12*, 025003.
[308] Y. Zhao, D. Xu, J. Sheng, Q. Meng, D. Wu, L. Wang, J. Xiao, W. Lv, Q. Chen, D. Sun, *Appl. Bionics Biomech.* **2018**, *2018*.
[309] D.-J. Guo, R. Liu, Y. Cheng, H. Zhang, L.-M. Zhou, S.-M. Fang, W. H. Elliott, W. Tan, *ACS Appl. Mater. Interfaces* **2015**, *7*, 5480.
[310] A. Kodaira, K. Asaka, T. Horiuchi, G. Endo, H. Nabae, K. Suzumori, *IEEE Robot. Autom. Lett.* **2019**, *4*, 1335.
[311] K. Zhang, Y. H. Jung, S. Mikael, J.-H. Seo, M. Kim, H. Mi, H. Zhou, Z. Xia, W. Zhou, S. Gong, Z. Ma, *Nat. Commun.* **2017**, *8*, 1.
[312] L. Maffli, S. Rosset, M. Ghilardi, F. Carpi, H. Shea, *Adv. Funct. Mater.* **2015**, *25*, 1656.
[313] C. Qu, S. Wang, L. Liu, Y. Bai, L. Li, F. Sun, M. Hao, T. Li, Q. Lu, L. Li, S. Qin, T. Zhang, *Small* **2019**, *15*, 1900216.
[314] S. Oh, Y. Jung, S. Kim, S. Kim, X. Hu, H. Lim, C. Kim, *Sci. Rep.* **2017**, *7*, 1.
[315] W. Miao, Y. Yao, Z. Zhang, C. Ma, S. Li, J. Tang, H. Liu, Z. Liu, D. Wang, M. A. Camburn, J.-C. Fang, R. Hao, X. Fang, S. Zheng, N. Hu, X. Wang, *Nat. Commun.* **2019**, *10*, 1.
[316] H. Rask-Andersen, W. Liu, E. Erixon, A. Kinnefors, K. Pfaller, A. Schrott-Fischer, R. Glueckert, *Anat. Rec.* **2012**, *295*, 1791.
[317] Y. Cheng, J. Cao, Y. Zhang, Q. Hao, *Bioinspir. Biomim.* **2019**, *14*, 031002.

[318] G. J. Lee, C. Choi, D.-H. Kim, Y. M. Song, *Adv. Funct. Mater.* **2018**, *28*, 1705202.
[319] S. Wu, T. Jiang, G. Zhang, B. Schoenemann, F. Neri, M. Zhu, C. Bu, J. Han, K.-D. Kuhnert, *Artif. Intell. Rev.* **2017**, *48*, 573.
[320] Z.-C. Ma, X.-Y. Hu, Y.-L. Zhang, X.-Q. Liu, Z.-S. Hou, L.-G. Niu, L. Zhu, B. Han, Q.-D. Chen, H.-B. Sun, *Adv. Funct. Mater.* **2019**, *29*, 1903340.
[321] C. W. Oyster, *The Human Eye : Structure and Function*, Sinauer, Sunderland, MA **1999**.
[322] D. Atchison, G. Smith, *Optics of the Human Eye*, Butterworth Heinemann, Waltham, MA **2000**.
[323] J.-J. Kim, H. Liu, A. O. Ashtiani, H. Jiang, *Rep. Prog. Phys.* **2020**, *83*, 047101.
[324] S. H. Oh, K. Rhee, S. K. Chung, *Sens. Actuators, A* **2016**, *240*, 153.
[325] A. O. Ashtiani, H. Jiang, *J. Micromech. Microeng.* **2015**, *26*, 015004.
[326] B. Jin, J.-H. Lee, Z. Zhou, G. Zhang, G.-B. Lee, H. Ren, C. Nah, *Opt. Eng.* **2016**, *55*, 017107.
[327] D. Liang, X.-Y. Wang, *Bioinspir. Biomim.* **2016**, *11*, 066008.
[328] C. Choi, M. K. Choi, S. Liu, M. S. Kim, O. K. Park, C. Im, J. Kim, X. Qin, G. J. Lee, K. W. Cho, M. Kim, E. Joh, J. Lee, D. Son, S.-H. Kwon, N. L. Jeon, Y. M. Song, N. Lu, D.-H. Kim, *Nat. Commun.* **2017**, *8*, 1.
[329] E. Perrier, S. Vergne, A. Klein, M. Poupin, P. Rondeau, L. Le Bellego, L. E. Armstrong, F. Lang, J. Stookey, I. Tack, *Br. J. Nutr.* **2013**, *109*, 1678.
[330] T. D. C. Minh, D. R. Blake, P. R. Galassetti, *Diabetes Res. Clin. Pract.* **2012**, *97*, 195.
[331] W. Wu, H. Haick, *Adv. Mater.* **2018**, *30*, 1705024.
[332] H. Jin, Y. S. Abu-Raya, H. Haick, *Adv. Healthcare Mater.* **2017**, *6*, 1700024.
[333] J. A. Raub, M. Mathieu-Nolf, N. B. Hampson, S. R. Thom, *Toxicology* **2000**, *145*, 1.
[334] F. Rule, R. S. Times, V. Ranges, *Occupational Safety and Health Administration*, United States Department of Labor **1993**, https://www.osha.gov/dts/sltc/methods/inorganic/id209/id209.html.
[335] S. Solomon, G.-K. Plattner, R. Knutti, P. Friedlingstein, *Proc. Natl. Acad. Sci.* **2009**, *106*, 1704.
[336] J. He, P. Xiao, J. Shi, Y. Liang, W. Lu, Y. Chen, W. Wang, P. Théato, S.-W. Kuo, T. Chen, *Chem. Mater.* **2018**, *30*, 4343.
[337] H. Wang, H. Luo, H. Zhou, X. Zhou, X. Zhang, W. Lin, G. Yi, Y. Zhang, *Chem. Eng. J.* **2018**, *345*, 452.
[338] M. Qin, M. Sun, R. Bai, Y. Mao, X. Qian, D. Sikka, Y. Zhao, H. J. Qi, Z. Suo, X. He, *Adv. Mater.* **2018**, *30*, 1800468.
[339] E. Colusso, G. Perotto, Y. Wang, M. Sturaro, F. Omenetto, A. Martucci, *J. Mater. Chem. C* **2017**, *5*, 3924.
[340] S. Savagatrup, V. Schroeder, X. He, S. Lin, M. He, O. Yassine, K. N. Salama, X.-X. Zhang, T. M. Swager, *Angew. Chem.* **2017**, *129*, 14254.
[341] H. Lodish, A. Berk, C. A. Kaiser, M. Krieger, M. P. Scott, A. Bretscher, H. Ploegh, P. Matsudaira, *Molecular Cell Biology*, Macmillan, New York **2008**.
[342] W. P. Jencks, *Adv. Enzymol. Relat. Areas Mol. Biol.* **1975**, *43*, 219.
[343] M. Soler, G. R. Newkome, *Supramol. Chem.: Mol. Nanomater.* **2012**.
[344] X. Zhang, C. Wang, *Chem. Soc. Rev.* **2011**, *40*, 94.
[345] F. Liu, B. Dong, X. Liu, Y. Zheng, J. Zi, *Opt. Express* **2009**, *17*, 16183.
[346] H.-b. Seo, S.-Y. Lee, *Sci. Rep.* **2017**, *7*, 1.
[347] M. Rassart, P. Simonis, A. Bay, O. Deparis, J. P. Vigneron, *Phys. Rev. E* **2009**, *80*, 031910.
[348] S. Mouchet, M. Lobet, B. Kolaric, A. Kaczmarek, R. Van Deun, P. Vukusic, O. Deparis, E. Van Hooijdonk, *Mater. Today: Proc.* **2017**, *4*, 4979.
[349] Z. Lei, Q. Wang, S. Sun, W. Zhu, P. Wu, *Adv. Mater.* **2017**, *29*, 1700321.
[350] B. Li, H. Tan, S. Anastasova, M. Power, F. Seichepine, G.-Z. Yang, *Biosens. Bioelectron.* **2019**, *123*, 77.
[351] A. S. French, P. H. Torkkeli, E.-A. Seyfarth, *J. Comp. Physiol., A* **2002**, *188*, 739.
[352] F. G. Barth, M. Wadepuhl, *J. Morphol.* **1975**, *145*, 209.
[353] P. S. Hill, *Naturwissenschaften* **2009**, *96*, 1355.
[354] Z. Han, L. Liu, J. Zhang, Q. Han, K. Wang, H. Song, Z. Wang, Z. Jiao, S. Niu, L. Ren, *Nanoscale* **2018**, *10*, 15178.
[355] A. Hudspeth, *Nat. Rev. Neurosci.* **2014**, *15*, 600.
[356] M. Bathe, C. Heussinger, M. M. Claessens, A. R. Bausch, E. Frey, *Biophys. J.* **2008**, *94*, 2955.
[357] P. Huang, Y.-Q. Li, X.-G. Yu, W.-B. Zhu, S.-Y. Nie, H. Zhang, J.-R. Liu, N. Hu, S.-Y. Fu, *ACS Appl. Mater. Interfaces* **2018**, *10*, 11197.
[358] T. Yang, X. Jiang, Y. Zhong, X. Zhao, S. Lin, J. Li, X. Li, J. Xu, Z. Li, H. Zhu, *ACS Sens.* **2017**, *2*, 967.
[359] Y. Hu, K. Qi, L. Chang, J. Liu, L. Yang, M. Huang, G. Wu, P. Lu, W. Chen, Y. Wu, *J. Mater. Chem. C* **2019**, *7*, 6879.
[360] I. Hanukoglu, V. R. Boggula, H. Vaknine, S. Sharma, T. Kleyman, A. Hanukoglu, *Histochem. Cell Biol.* **2017**, *147*, 733.
[361] S. Lin, X. Zhao, X. Jiang, A. Wu, H. Ding, Y. Zhong, J. Li, J. Pan, B. Liu, H. Zhu, *Small* **2019**, *15*, 1900848.
[362] X. Pan, Q. Wang, P. He, K. Liu, Y. Ni, L. Chen, X. Ouyang, L. Huang, H. Wang, S. Xu, *Chem. Eng. J.* **2020**, *379*, 122271.
[363] M. Liao, P. Wan, J. Wen, M. Gong, X. Wu, Y. Wang, R. Shi, L. Zhang, *Adv. Funct. Mater.* **2017**, *27*, 1703852.
[364] G. Cai, J. Wang, K. Qian, J. Chen, S. Li, P. S. Lee, *Adv. Sci.* **2017**, *4*, 1600190.
[365] J. H. Waite, N. H. Andersen, S. Jewhurst, C. Sun, *J. Adhes.* **2005**, *81*, 297.
[366] Z. Gao, Y. Li, X. Shang, W. Hu, G. Gao, L. Duan, *Mater. Sci. Eng., C* **2020**, *106*, 110168.
[367] B. Yin, X. Liu, H. Gao, T. Fu, J. Yao, *Nat. Commun.* **2018**, *9*, 1.
[368] S. Xia, Q. Zhang, S. Song, L. Duan, G. Gao, *Chem. Mater.* **2019**, *31*, 9522.
[369] J. C. Tuthill, R. I. Wilson, *Curr. Biol.* **2016**, *26*, R1022.
[370] F. G. Barth, *Curr. Opin. Neurobiol.* **2004**, *14*, 415.
[371] J. Ashmore, *Physiol. Rev.* **2008**, *88*, 173.
[372] Y. Guo, Z. Guo, M. Zhong, P. Wan, W. Zhang, L. Zhang, *Small* **2018**, *14*, 1803018.
[373] X. Dong, Y. Wei, S. Chen, Y. Lin, L. Liu, J. Li, *Compos. Sci. Technol.* **2018**, *155*, 108.
[374] T. Bu, T. Xiao, Z. Yang, G. Liu, X. Fu, J. Nie, T. Guo, Y. Pang, J. Zhao, F. Xi, Z. L. Wang, *Adv. Mater.* **2018**, *30*, 1800066.
[375] G. Yao, L. Xu, X. Cheng, Y. Li, X. Huang, W. Guo, S. Liu, Z. L. Wang, H. Wu, *Adv. Funct. Mater.* **2019**, *30*, 1907312.
[376] X. Pu, M. Liu, X. Chen, J. Sun, C. Du, Y. Zhang, J. Zhai, W. Hu, Z. L. Wang, *Sci. Adv.* **2017**, *3*, e1700015.
[377] Y.-C. Lai, J. Deng, R. Liu, Y.-C. Hsiao, S. L. Zhang, W. Peng, H.-M. Wu, X. Wang, Z. L. Wang, *Adv. Mater.* **2018**, *30*, 1801114.
[378] L. Pu, R. Saraf, V. Maheshwari, *Sci. Rep.* **2017**, *7*, 1.
[379] Y.-F. Liu, Y.-F. Fu, Y.-Q. Li, P. Huang, C.-H. Xu, N. Hu, S.-Y. Fu, *J. Mater. Chem. B* **2018**, *6*, 896.
[380] S. Fox, *Human Physiology*, McGraw-Hill Education, New York **2015**.
[381] C. M. Boutry, M. Negre, M. Jorda, O. Vardoulis, A. Chortos, O. Khatib, Z. Bao, *Sci. Rob.* **2018**, *3*, eaau6914.
[382] Y. Pang, K. Zhang, Z. Yang, S. Jiang, Z. Ju, Y. Li, X. Wang, D. Wang, M. Jian, Y. Zhang, R. Liang, H. Tian, Y. Yang, T.-L. Ren, *ACS Nano* **2018**, *12*, 2346.
[383] S.-H. Kim, S. Oh, K. B. Kim, Y. Jung, H. Lim, K.-J. Cho, *IEEE Robot. Autom. Lett.* **2018**, *3*, 3545.
[384] K. S. Kindt, G. Finch, T. Nicolson, *Dev. Cell* **2012**, *23*, 329.
[385] H. Bleckmann, R. Zelick, *Integr. Zool.* **2009**, *4*, 13.
[386] J. Engelmann, W. Hanke, J. Mogdans, H. Bleckmann, *Nature* **2000**, *408*, 51.
[387] A. B. Kroese, J. M. Van der Zalm, J. Van den Bercken, *Pfluegers Arch.* **1978**, *375*, 167.

[388] I. Russell, in *Frog Neurobiology* (Eds: R. Llinas, W. Precht), Springer, New York **1976**, pp. 513–550.
[389] E. Schwartz, in *Electroreceptors and Other Specialized Receptors in Lower Vertrebrates* (Ed: A. Fessard), Springer, New York **1974**, pp. 257–278.
[390] A. Ghysen, C. Dambly-Chaudière, *Genes Dev.* **2007**, *21*, 2118.
[391] S. P. Windsor, S. E. Norris, S. M. Cameron, G. D. Mallinson, J. C. Montgomery, *J. Exp. Biol.* **2010**, *213*, 3819.
[392] S. P. Windsor, S. E. Norris, S. M. Cameron, G. D. Mallinson, J. C. Montgomery, *J. Exp. Biol.* **2010**, *213*, 3832.
[393] S. M. van Netten, M. J. McHenry, in *The Lateral Line System* (Eds: S. Coombs, H. Bleckmann, R. R. Fay, A. N. Popper), Springer, New York **2013**, pp. 99–119.
[394] J. C. Montgomery, C. F. Baker, A. G. Carton, *Nature* **1997**, *389*, 960.
[395] D. J. Randall, D. Randall, W. Burggren, K. French, R. Eckert, *Eckert Animal Physiology*, Macmillan, New York **2002**.
[396] Y. Jiang, Z. Ma, D. Zhang, *Bioinspir. Biomim.* **2019**, *14*, 041001.
[397] M. Bora, A. G. P. Kottapalli, J. Miao, M. S. Triantafyllou, *Bioinspir. Biomim.* **2018**, *13*, 025002.
[398] C. Abels, V. M. Mastronardi, F. Guido, T. Dattoma, A. Qualtieri, W. M. Megill, M. De Vittorio, F. Rizzi, *Sensors* **2017**, *17*, 1080.
[399] G. Liu, A. Wang, X. Wang, P. Liu, *Appl. Bionics Biomechan.* **2016**, *2016*.
[400] A. G. P. Kottapalli, M. Bora, E. Kanhere, M. Asadnia, J. Miao, M. S. Triantafyllou, *Sensors* **2017**, *17*, 1728.
[401] M. Bora, A. Kottapalli, J. Miao, M. Triantafyllou, in *2017 19th Int. Conf. on Solid-State Sensors, Actuators and Microsystems*, IEEE, Piscataway, NJ **2017**, pp. 1211–1214.
[402] A. G. P. Kottapalli, M. Bora, M. Asadnia, J. Miao, S. S. Venkatraman, M. Triantafyllou, *Sci. Rep.* **2016**, *6*, 1.
[403] M. Bora, A. Kottapalli, J. Miao, M. Triantafyllou, *APL Mater.* **2017**, *5*, 104902.
[404] M. Asadnia, A. G. P. Kottapalli, J. Miao, M. E. Warkiani, M. S. Triantafyllou, *J. R. Soc., Interface* **2015**, *12*, 20150322.
[405] M. A. Sharif, X. Tan, in *Electroactive Polymer Actuators and Devices XX*, International Society for Optics and Photonics, Bellingham, WA **2018**.
[406] H. Lei, M. A. Sharif, D. A. Paley, M. J. McHenry, X. Tan, in *Electroactive Polymer Actuators and Devices 2016*, International Society for Optics and Photonics, Las Vegas, NV **2016**.
[407] J. P. Wissman, K. Sampath, S. E. Freeman, C. A. Rohde, *Sensors* **2019**, *19*, 2639.
[408] J. P. Wissman, K. Sampath, C. A. Rohde, in *Bioinspiration, Biomimetics, and Bioreplication IX*, International Society for Optics and Photonics, Denver, CO **2019**, 109650T.
[409] M. Asadnia, A. G. P. Kottapalli, K. D. Karavitaki, M. E. Warkiani, J. Miao, D. P. Corey, M. Triantafyllou, *Sci. Rep.* **2016**, *6*, 32955.
[410] B. J. Wolf, S. M. van Netten, in *2019 IEEE Sensors Applications Symp.*, IEEE, Sophia Antipolis, France **2019**, pp. 1–6.
[411] B. J. Wolf, J. A. Morton, W. N. MacPherson, S. M. Van Netten, *Bioinspir. Biomim.* **2018**, *13*, 026013.
[412] M. Su, R. Xie, Y. Zhang, X. Kang, D. Huang, Y. Guan, H. Zhu, *Appl. Sci.* **2019**, *9*, 2999.

**Mahdi Ilami** received his B.S. in mechanical engineering from Ferdowsi University of Mashhad, Iran in 2012. He received his M.S. in mechanical engineering from Iran University of Science and Technology, Tehran, Iran in 2015. He is currently a Ph.D. candidate at Arizona State University, Tempe, AZ, USA. His research interests include magnetically controlled robots and their applications in healthcare.

**Hosain Bagheri** received his B.Sc. (2009) and M.Sc. (2012) in mechanical engineering from the University of Arizona, Tucson, AZ, USA. After 4 years of working in industry, he returned to academia. He is currently a Ph.D. candidate at Arizona State University, Tempe, AZ, USA. His research interests include terrestrial and aquatic bioinspired robotic systems.

**Reza Ahmed** received his B.S. in mechanical engineering from Brigham Young University Idaho, Rexburg, USA in 2014. He is currently a Ph.D. student at Arizona State University, Tempe, AZ, USA. His research interests include magnetic robotics; particularly magnetic control of ferrofluid droplets.

**E. Olga Skowronek** received her B.S. in mechanical engineering from North Carolina State University, Raleigh, NC, USA. She is currently a Ph.D. student at Arizona State University, Tempe, AZ, USA. Her research interests include bioinspired soft robotics and the 3D printing of soft robots.

**Hamid Marvi** is an assistant professor of mechanical and aerospace engineering at Arizona State University, Tempe, AZ, USA. He received his Ph.D. in mechanical engineering from Georgia Institute of Technology, Atlanta, GA, USA in 2013 and worked as a postdoctoral associate at Georgia Tech (2013–2014) and at Carnegie Mellon University, Pittsburgh, PA, USA (2014–2015). His research interests include bioinspired, soft, and magnetic robotics, and physics of interactions with granular environments.